PROCESSING AND CHARACTERIZATION OF TEXTURED BARIUM FERRITE CERAMICS

A THESIS SUBMITTED TO
THE GRADUATE SCHOOL OF NATURAL AND APPLIED SCIENCES
OF
MIDDLE EAST TECHNICAL UNIVERSITY

BY

EDA AYDOĞAN

IN PARTIAL FULFILLMENT OF THE REQUIREMENTS
FOR
THE DEGREE OF MASTER OF SCIENCE
IN
METALLURGICAL AND MATERIALS ENGINEERING

JUNE 2012

Approval of the thesis:

PROCESSING AND CHARACTERIZATION OF TEXTURED BARIUM FERRITE CERAMICS

submitted by **EDA AYDOĞAN** in partial fulfillment of the requirements for the degree of **Master of Science in Metallurgical and Materials Engineering Department, Middle East Technical University** by,

Prof. Dr. Canan ÖZGEN _____
Dean, Graduate School of **Natural and Applied Sciences**

Prof. Dr. C. Hakan GÜR _____
Head of Department, **Metallurgical and Materials Engineering**

Assoc. Prof. Dr. Arcan Fehmi DERİCİOĞLU _____
Supervisor, **Metallurgical and Materials Engineering Dept., METU**

Examining Committee Members:

Prof. Dr. Muharrem TİMUÇİN _____
Department of Metallurgical and Materials Eng., METU

Assoc. Prof. Dr. Arcan Fehmi DERİCİOĞLU _____
Department of Metallurgical and Materials Eng., METU

Assoc. Prof. Dr. Caner DURUCAN _____
Department of Metallurgical and Materials Eng., METU

Assoc. Prof. Dr. Zafer Evis _____
Department of Engineering Sciences, METU

Assist. Prof. Dr. Y. Eren KALAY _____
Department of Metallurgical and Materials Eng., METU

Date: 29.06.2012

I hereby declare that all information in this document has been obtained and presented in accordance with academic rules and ethical conduct. I also declare that, as required by these rules and conduct, I have fully cited and referenced all material and results that are not original to this work.

Name, Last name : Eda AYDOĞAN

Signature :

ABSTRACT

PROCESSING AND CHARACTERIZATION OF TEXTURED BARIUM FERRITE CERAMICS

Aydoğan, Eda

M.Sc., Department of Metallurgical and Materials Engineering

Supervisor : Assoc. Prof. Dr. Arcan Fehmi Dericioğlu

Co-Supervisor: Prof. Dr. Muharrem Timuçin

June 2012, 114 pages

Technological advances results in the fact that quite a large number of electronic equipment interacts with its environment leading to the malfunction of the devices. This brings about the necessity of using proper electromagnetic (EM) wave absorbers/shields to avoid such interactions. In order to absorb EM waves in a large frequency band from several MHz to GHz, barium hexaferrite (BaHF) ceramics which are produced as textured ceramics as well as in multilayered form can be used. Textured ceramics are processed by tape casting using templated grain growth (TGG) phenomenon. In order to obtain textured ceramics, BaHF powders and platelets are required as raw materials in such a way that during sintering small size powders are directioned by large platelet surfaces. In this study, ferrite powders were synthesized by mixed oxide technique while the platelets were produced by both molten salt synthesis (MSS) and reactive templated grain growth (RTGG) methods. In the case of platelet synthesis by MSS, effects of calcination temperature

and time as well as type and composition of the flux on the formation and morphology of platelets were investigated based on the XRD and SEM results. Studies have shown that KCl flux led to the formation of sharper platelet morphology, while NaCl resulted in more round shapes. However, extent of BaHF formation in the case of NaCl was higher when compared to KCl flux due to its higher wettability characteristic, and hence faster interaction with the raw materials. Since the aspect ratio of the synthesized platelets was only ca. 2-4, these platelets were not efficient for further TGG studies. Alternatively, $BiFeO_3$ (BiF) particles having ~30-40 μm average size were synthesized as seed crystals for the synthesis of BaHF platelets by RTGG method. After the washing of these platelets with dilute HNO_3, pure BaHF powders and platelets were directed by tape casting which was followed by sintering using TGG phenomenon. Degree of achieved texturing in the processed ceramics was studied using Rietveld analysis, pole figure measurement and electron backscattered diffraction (EBSD).

Keywords: Barium ferrites, molten salt synthesis (MSS), templated grain growth (TGG), textured ceramics, Rietveld analysis, pole figure, electron backscattered diffraction (EBSD).

ÖZ

YÖNLENDİRİLMİŞ BARYUM FERRİT SERAMİKLERİN ÜRETİLMESİ VE KARAKTERİZASYONU

Aydoğan, Eda
Yüksek Lisans, Metalurji ve Malzeme Mühendisliği Bölümü
Tez Yöneticisi : Doç. Dr. Arcan Fehmi Dericioğlu
Ortak Tez Yöneticisi: Prof. Dr. Muharrem Timuçin

Haziran 2012, 114 sayfa

Teknolojik gelişmeler birçok elektronik cihazın çevresiyle etkileşime girerek işlevlerini kaybetmelerine neden olmaktadır. Bu tür etkileşimleri engellemek için, uygun elektromanyetik dalga absorplayıcı malzemelerin kullanımını gerektirmektedir. Elektromanyetik dalgaları MHz'den GHz'e kadar geniş bir frekans aralığında absorplayabilmek için dokulu (yönlenmiş) ve çok katmanlı barium hekzaferrit (BaHF) seramikler kullanılabilir. Dokulu seramikler şerit döküm yöntemi ile şablonlu tane büyümesi metodu kullanılarak üretilir. Dokulu seramik üretmek için ham madde olarak baryum ferrit plakalara ve tozlara ihtiyaç duyulur. Çünkü sinterleme sırasında plakalara göre daha küçük boyutlu tozlar, plakalar tarafından yönlendirilerek plakalarla aynı yönde büyümesini sağlanır. Bu çalışmada ferrit tozları karışık oksit tekniği ile sentezlenirken, plakalar eriyik tuz sentezleme (MSS) ve reaktif şablonlu tane büyümesi (RTGG) metotları ile üretilmiştir. MSS yöntemi ile sentezlenen plakalar için kalsinasyon sıcaklığı ve zamanının yanında, tuz çeşidi ve kompozisyonunun plaka morfolojisine ve faz dönüşümüne etkisi, XRD

ve SEM karakterizasyon sonuçlarına bağlı olarak tartışılmıştır. Yapılan çalışmalar KCl tuzu içerisinde sentezlenen plakaların daha sivri kenarlara sahip olurken, NaCl tuzu içerisinde sentezlenenlerin daha yuvarlak bir morfolojiye sahip olduklarını göstermiştir. Fakat NaCl tuzunun yüksek ıslatabilme karakteristiği ve dolayısıyla tozlarla hızlı etkileşimi nedeniyle BaHF oluşumu NaCl tuzu içerisinde KCl tuzuna nazaran daha fazladır. Plakaların en-boy oranları ortalama 2-4 olduğu için, üretilen plakalar şablonlu tane büyümesi için etkili olarak kullanılamamıştır. Bunun yerine, reaktif şablonlu tane büyümesi (RTGG) yöntemi ile BaHF plakaların üretimi için ortalama 30-40 μm büyüklükteki $BiFeO_3$ (BiF) parçacıkları şablon olarak kullanılmak üzere sentezlenmiştir. Sentezlenen toz ve plakalar seyreltik HNO_3 acidi ile yıkandıktan sonra şerit döküm yöntemi ve sinterleme ile şablonlu tane büyümesi metodunu kullanarak yönlendirilmiştir. Üretilen seramiklerdeki ulaşılan yönlenme derecesi Rietveld analiz yöntemi, ‘‘pole’’ figür ölçümü ve elektron geri saçılım kırınımı (EBSD) karakterizasyon yöntemi kullanılarak belirlenmiştir.

Anahtar Kelimeler: Baryum ferritler, eriyik tuz yöntemi, şablonlu tane büyümesi, yönlendirilmiş seramikler, Rietveld analizi, ‘‘pole’’ figür, electron geri saçılım kırınımı (EBSD).

To My Family,

ACKNOWLEDGEMENTS

I would like to express my sincere appreciation to Assoc. Prof. Dr. Arcan Dericioğlu and Prof. Dr. Muharrem Timuçin for their supervision, guidance, support and encouragement throughout the study.

I am grateful to Prof. Dr. Şakir Bor, Assist. Prof. Dr. Y. Eren Kalay and Assist Prof. Dr. Caner Şimşir for their special support and consultancy during my study. I feel obliged to Aylin Güneş for her help in XRD characterizations and Göksu Gürer and Selen N. Gürbüz Güner for their guidance.

I also thank to the staff of Metal Forming Center of Excellence, Atılım University for their helps for texture analysis as well as Central Laboratory, METU for their helps for elemental analysis.

I am grateful to all the staff of the Department of Metallurgical and Materials Engineering and my labmates Aylin Güneş, Cansu Yazganarıkan, Güney Daloğlu, Özgür Hamat, Selen N. Gürbüz Güner and Seray Kaya.

Finally, I owe a debt to my family and my fiancé Gökhan Güngör for their endless love, support and encouragement throughout my life.

TABLE OF CONTENTS

LIST OF TABLES

TABLES

LIST OF FIGURES

FIGURES

CHAPTER 1

INTRODUCTION

Ferrites are compounds of various metals and oxygen in a mixed crystal of a close-packed structure. They have a general formula of $MOFe_2O_3 \bullet xH_2O$ where M is a divalent metallic ion. Ferrites have high electrical resistivity, high hardness, low dielectric loss at high frequencies together with high permeability and low coercivity [1]. Meanwhile, certain magnetic and dielectric properties make ferrites eligible for various applications such as the usage of permanent magnets, chip inductors [2, 3], microwave absorbers [4] etc.

Barium hexaferrite (BaHF – $BaFe_{12}O_{19}$) is a hexagonal ferrimagnetic ceramic that can exhibit high uniaxial magnetocrystalline anisotropy and Curie temperature as well as excellent chemical stability and corrosion resistance [5-8]. Among ferrites, specifically, its magnetic and dielectric loss characteristics provide superior electromagnetic wave absorption properties [5]. It is mainly used in the field of magnetic recording media, microwave devices and electromagnetic shielding [9, 10].

The most important problem of BaHF ceramics in microwave absorption is that they can absorb the energy only within a narrow frequency band. However, this problem can be overcome by using barium hexaferrite (BaHF) ceramics with textured microstructure and processed in multilayered structures [11]. Research studies have proven that processing of textured ceramics is not as complicated as single crystal processing even though both reveal similar properties. However, there is very limited knowledge about the microwave applications of the textured

ferrites. Especially there is limited study available on the production of multilayered structures of textured BaHF ceramics which are produced by tape casting method, to the best of our knowledge. Reports available in this scope are mainly related with the production of textured ceramics under a strong magnetic field during pressing [12]. However, from the application point of view it is very attractive to obtain such a ceramic body that has different absorption characteristics in different directions. For this reason, in this study multilayered textured ferrites have been produced by tape casting method.

Anisotropy in platelet-like BaHF crystals is more obvious, since both the easy magnetization direction and c-axis are perpendicular to the basal plane of the platelet [5]. To make use of this, textured BaHF ceramics can be formed using templated grain growth (TGG) phenomenon [13], where BaHF platelets act as seed crystals orienting on their planar faces. For the effective operation of TGG, platelets having both large aspect ratios and radii are required.

Mainly various chemical methods such as sol-gel, hydrothermal, co-precipitation etc. have been used for the production of BaHF ceramics with platelet morphology in addition to molten salt method [6]. Molten salt synthesis (MSS) is a technique by which large (up to millimeter-size) seed crystals can by synthesized at low temperatures starting from mixed oxide raw materials [14]. Because of the small diffusion distances and high mobility of raw materials in molten salts along with high surface reactivity of the salts, reactions can be completed in a relatively short time interval [15]. In addition to low temperatures of formation, molten salts provide stabilization of different polymorphs when compared to other synthesis methods [16].

Although molten salt synthesis has been used extensively for BaHF platelet synthesis, to the best of our knowledge, there is limited information and comprehensive study about the kinetics of this process and the effect of flux type on the morphology. In the present study, diffusion kinetics of precursors in NaCl and KCl fluxes has been investigated by inductively coupled plasma spectroscopy, scanning electron microscopy and X-ray diffraction (XRD) analyses. Moreover,

effect of synthesis time and temperature as well as flux type and composition on the formation and morphology of BaHF have been studied.

This study is composed of two main parts; first one is the synthesis of barium hexaferrite powders and platelets, second one is the production of multilayered ceramics by tape casting using template grain growth phenomenon. In the first part of this study, barium hexaferrite powders are synthesized by mixed oxide technique while the platelets are synthesized by both molten salt synthesis (MSS) and reactive templated grain growth (RTGG) methods. During the synthesis of BaHF platelets by molten salt synthesis, effect of synthesis time and temperature as well as flux type and composition on the formation and morphology of BaHF has been investigated in detail. In the second part of the study, textured BaHF ceramics are processed by tape casting using the platelets synthesized by both MSS and RTGG methods. However, textured BaHF ceramics could not be obtained by using the platelets synthesized by MSS since they have maximum radial size of 2-4 μm. Using the platelets synthesized by RTGG from bismuth ferrite seed crystals, textured bulk BaHF ceramics are obtained by tape casting using templated grain growth phenomenon. In the present study, BaHF powders, platelets synthesized by both MSS and RTGG methods and textured bulk ceramics produced by tape casting were characterized by X-ray diffraction (XRD) and scanning electron microscopy (SEM) techniques. Additionally, in order to investigate effect of flux type and composition as well as calcination time and temperature on the morphology, size and growth mechanism of BaHF platelets during the platelet synthesis by MSS, inductively coupled plasma-mass spectroscopy (ICP-MS) studies were conducted. For the determination of degree of texture achieved in BaHF ceramics, Rietveld analyses, pole figure measurements and EBSD studies were carried out.

Throughout this thesis, in the first chapter, general information about BaHF ceramics, production of textured ceramics and focus of the present study have been presented. In the second chapter, theory and literature review about the properties of BaHF and synthesis methods of BaHF powders and platelets as well as templated grain growth (TGG) phenomenon for the production of textured

ceramics have been expressed. Second chapter is followed by third, fourth, fifth and sixth chapters which cover experimental procedure, results, discussion and conclusion, respectively.

CHAPTER 2

LITERATURE REVIEW

2.1. Electromagnetic Interference (EMI) Shielding And EM Wave Absorbing Materials

Since electromagnetic waves are used extensively in radar, telecommunication, wireless broadcasting, imaging, medical diagnosis, surveillance etc., their interaction with each other and other electronic devices may cause interference in data transfer and failure of the devices. One of the most effective ways to decrease the electromagnetic interference is to use of electromagnetic wave absorbing materials. In anechoic applications, dielectric and ferrite type absorbers are used extensively. Dielectric absorbers were used primarily in anechoic applications during the 1940s when indoor test facilities were first developed. In the 1950s, urethane foam in pyramidal-shape was started to be used, and this dielectric absorber foam was the main product of anechoic applications up to 1970s [17]. At first, ferrites were used for low frequency applications; however, with the use of multilayered ferrites and the proper dopants, ferrites could be used in wide microwave frequencies [18].

2.1.1 Pyramidal Absorber

2.1.1.1. Solid Foam

Solid foam is a kind of urethane foam that is loaded with carbon. It can show the highest broadband performance among all the dielectric absorbers at both straight, square pyramid (Figure 2.1 (a)) and the twisted pyramid (Figure 2.1 (b)). Solid foam has extensive usage in anechoic applications, since it can reduce forward scattering while increasing back scattering. Especially, the twisted pyramids are used for the dielectric absorption of wide incidence angles.

The shoulders of the two pyramid geometry stated above can carry the load of the cantilever geometry. Although the twisted pyramid is black, it is painted with a latex paint in order to increase the light reflectance. In order to hinder the decrease in reflectivity, the tips of the absorbers left as unpainted which is also good for the prevention of tip breakage as a result of wear and tear. Foam absorber needs to be well maintained as it is not strong enough.

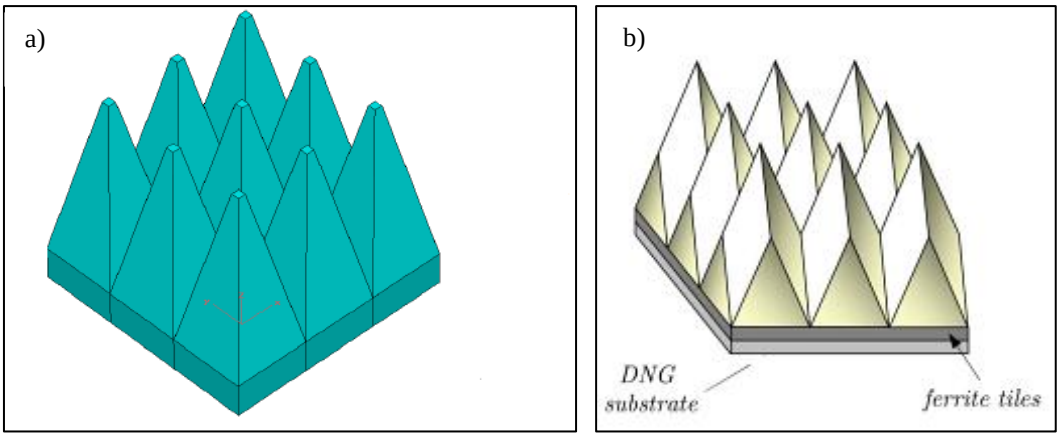

Figure 2.1 Geometry of the (a) standard pyramid [19], (b) twisted pyramid absorber [20].

Electromagnetic performance of pyramidal absorbers is evaluated as normal incidence reflectivity and expressed in –dB. Generally, this information is provided in graphics of reflectivity (in –dB) vs. material thickness (on the order of wavelength). Figure 2.2 shows typical performance of pyramidal materials.

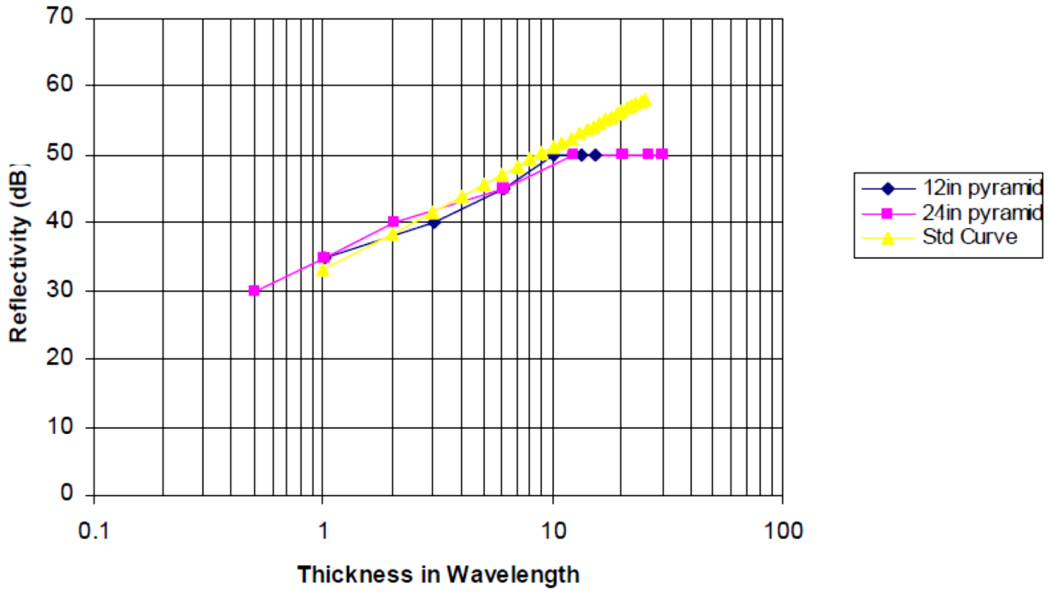

Figure 2.2 Normal incidence reflectivity performance of pyramidal absorbers [21].

2.1.1.2. Hollow Pyramidal Absorber

Hollow pyramidal absorbers are lightweight which are made wrapping by thin sheets of lossy foam absorbers and sticking to a backside a foam panel. As well as having fire retardancy, they may have some small holes allowing the cooling air blown behind to spread through the piece can be introduced. In order to improve their performance at the lower frequencies (down to 30 MHz), length of the pyramids should be longer [22].

2.1.2 Wedge Absorber

Wedge absorber is a kind of foam absorber having the geometry similar to that of the pyramidal absorbers in one direction with uniform shape in the other direction. It is used in chamber designs of energy ceasing walls for measurements of radar cross-section (RCS). The wedge design makes the absorber sensitive to polarization and prevents backscatter of the incident beam coming with high incidence angles. Figure 2.3 shows the geometry of wedge-shaped absorber whose reflectivity is a bit less than the pyramidal materials having the same height with wedge absorber [23].

Figure 2.3 Geometry of wedge-shaped absorber material [24].

2.1.3 Convoluted Microwave Absorber

Convoluted microwave absorber is a kind of broadband dielectric microwave absorber that is made of convoluted foam (Figure 2.4). It is mainly suitable for the usage in the upper microwave frequency ranges, especially in the millimeter bands.

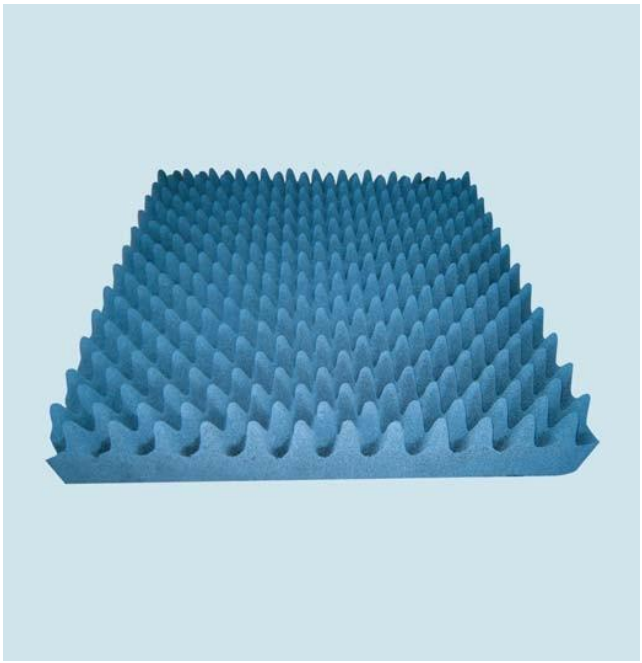

Figure 2.4 Geometry of the convoluted absorber [25].

2.1.4 Multilayered Dielectric Absorber

Multilayered dielectric absorber is composed of uniform sheets of foam (Figure 2.5). Depending on the overall thickness of the absorber, sheet thickness may vary. As illustrated in Figure 2.6, with the increase in the thickness of the product, the operation frequency of the material becomes lower [26] causing this material to be used only in laboratory applications.

Figure 2.5 Geometry of the multilayered absorber [27].

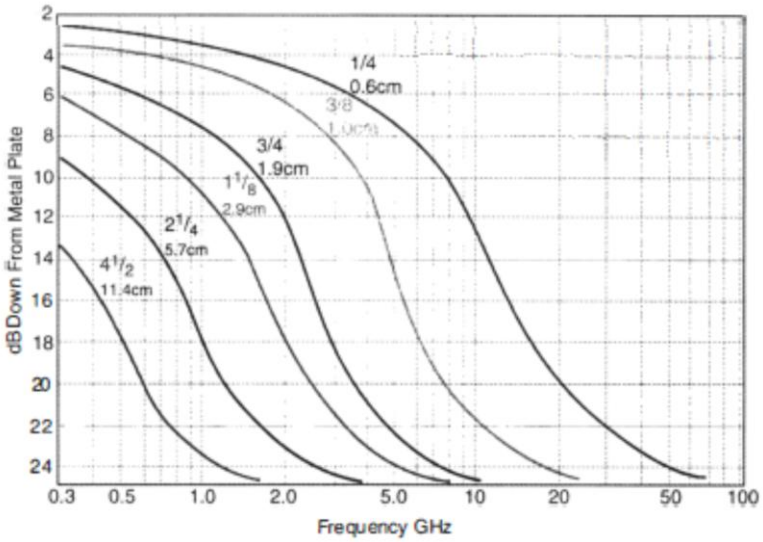

Figure 2.6 Performance curves of multilayered absorber [26].

2.1.4.1. Jaumann Absorbers

Jaumann absorbers are composed of multilayered resistive sheets in such an order that the highest resistivity sheet is in the front while the lowest resistivity one is at the back. By this way bandwidth of the Salisbury screen made by positioning resistive sheets on the surface of an object to build a resonant absorber can be enhanced [28]. Increasing number of layers broadens the EM wave absorption frequency range (Figure 2.7). Knott et al. [29] reported that the Jaumann absorber having four-layer structure has about four times the fractional bandwidth of a single layer absorber.

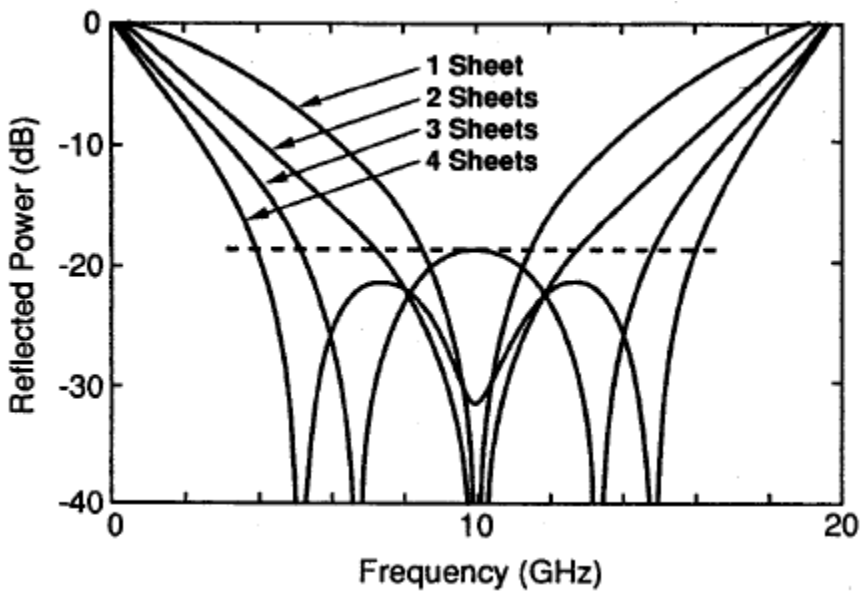

Figure 2.7 The predicted performance of Jaumann multilayered absorbers [29].

2.1.5 Hybrid Dielectric Absorber

Multilayered absorber is 33% more efficient in terms of providing dielectric loss compared to a pyramidal absorber having the same thickness. Hence, hybrid dielectric absorber which is combination of the two types is more suitable for the applications below 1 GHz frequency. These dielectric hybrids consist of a pyramidal front material that is matching with subsequent graded dielectric layers. Impedance match for the energy transfer to the higher grade dielectric layer is provided by the pyramidal front. Consequently, high energy loss can be attained at

low frequencies. On the other hand, multilayered structure which is stacked easily can be constructed through the large square base of the product (Figure 2.8). When compared to the pyramidal absorber having the same height, performance increases about 3-6 dB in the case of normal incidence, while it is 6-10 dB at wide angle incidence [17].

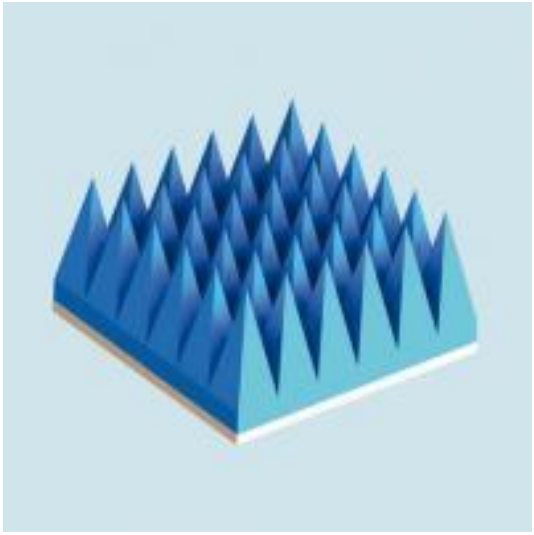

Figure 2.8 Geometry of hybrid dielectric absorber [30].

The Dallenbach layer consists of a homogeneous dielectric layer back of which is sticked to a metal plate and the reflections from both the outer and back surfaces cancel each other. Impedance change at the interface of the two media leads to the reflection at the surface. If the impedance difference of a material relative to the space is zero, reflection at the surface will be hindered. However, it is almost impossible to produce a dielectric material having lossy characteristics at broadband ranges. Reflection coefficient of Dallenbach layers changes with thickness for different permeability and permittivity values [28], as shown in Figure 2.9.

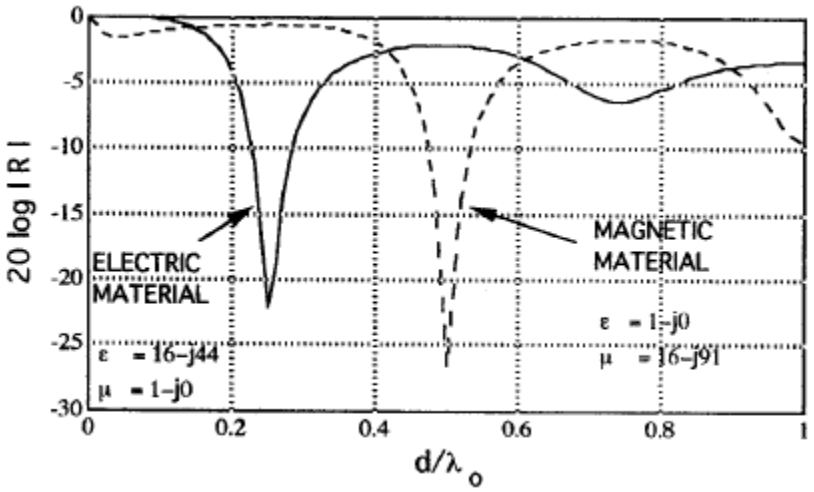

Figure 2.9 Performance of Dallenbach Layers [28].

2.1.6 Walkway Absorber

Broadband walkway absorber is composed of pyramidal absorber on which an interlocking pattern occupied by a self-extinguishing polystyrene core is located. A denser polystyrene laminate is placed on top of this structure as shown in Figure 2.10 [31].

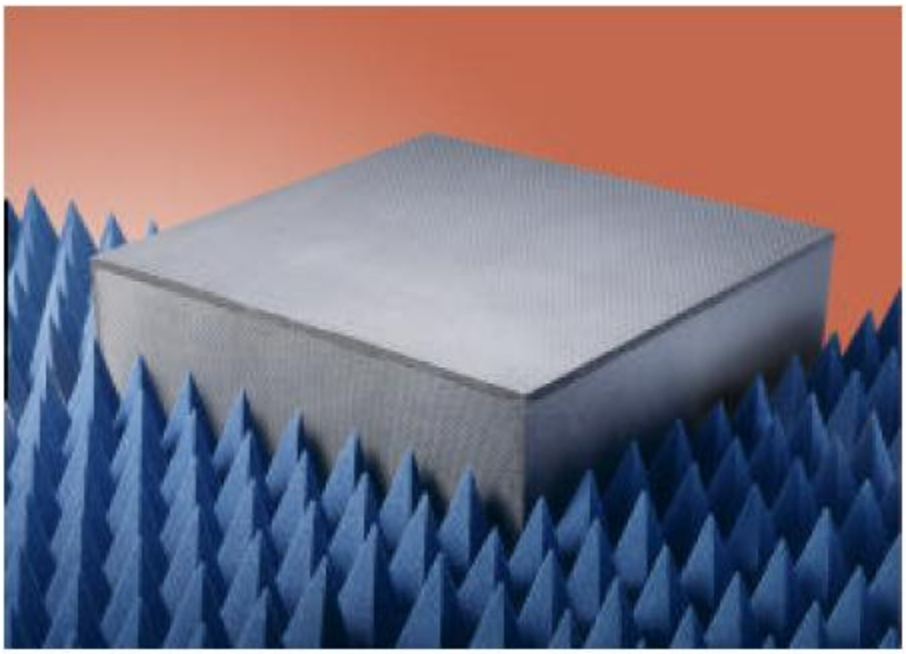

Figure 2.10 Geometry of a walkway absorber [31].

2.2. Ferrites For EMI Shielding and Barium Hexaferrites

Ferrites have close-packed structure that is composed of oxygen anions and metallic cations filling the interstices. They have a general formula $MeOFe_2O_3.xH_2O$ where M is a divalent metallic ion such as Mn^{2+}, Fe^{2+}, Co^{2+}, Ni^{2+}, Zn^{2+}, Mg^{2+} and Cd^{2+}. In general, the magnetic saturation intensity of ferrites is lower than that of various metallic magnetic alloys, whereas ferrites have very high resistivity and can be used as insulators. Therefore, low power loss in ferrites at high frequencies makes them suitable at these frequency ranges [1].

Ferrites are ferrimagnets; meaning that they have a net magnetic moment as the net magnetization of magnetic sublattices is not zero [1].

Ferrites can be classified as spinel, garnet and magnetoplumbite with respect to their crystal structure. Different ratios of the Fe_2O_3 to the other oxide component may lead to distinct structures (Table 2.1)

Table 2.1 Summary of ferrite structure types according to various Fe_2O_3 –MeO (or Me_2O_3) oxide ratios [32].

Spinel	$1Fe_2O_3$-1MeO	where MeO=transition metal oxide
Garnet	5 Fe_2O_3-3 Me_2O_3	where Me_2O_3=rare earth metal oxide
Magnetoplumbite	$6Fe_2O_3$-1MeO	where MeO=divalent metal oxide from group IIA (BaO, CaO, SrO)

The *spinel* ferrites possess the structure of the natural spinel, $MgAl_2O_4$. Although most of the commercially important spinels are synthetic, magnetite (Fe_3O_4) which is the most important and oldest magnetic material is natural. Bragg (1915) and Nishikawa (1915) firstly determined the structure of spinel. The ideal structure is formed by a cubic close-packed array of O atoms, in which cations fill one-eighth of the tetrahedral and one-half of the octahedral interstitial sites. The unit cell contains eight formula units AB_2O_4, with eight A sites, 16 B sites and 32 oxygens. A and B refer to the tetrahedrally coordinated sites and the octahedrally

coordinated sites, respectively [33]. In order to indicate the arrangement of the A and B sites, it is beneficial to take A site as the origin and divide the unit cell into eight cubes of edge *a/2*. Spinel ferrites have the space group of $Fd\bar{3}m$, and they are composed of one A and three B cations resulting in four-fold coordination of O atoms [34].

In magnetooptical, microwave and memory applications, garnet ferrites are used extensively. Therefore, they are studied in the form of bulk ceramics, single crystals, thin and epitaxial films, etc. The general formula of ferrite garnets is $R_3Fe_5O_{12}$, where R is a rare-earth trivalent cation. Garnet ferrites have cubic symmetry and space group of $Ia\bar{3}d$ where 160 atoms form eight formula units in a unit cell. O sublattice can be represented by a polyhedral combination rather than a close-packed arrangement unlike the spinel ferrites [33].

Magnetoplumbite ferrites have hexagonal symmetry like the inverse spinel, and they are generally called as hexagonal ferrites. The chemical formula may be represented as $MeFe_{12}O_{19}$ where Me is a divalent ion such as barium, lead or strontium [35]. In the present study, $BaFe_{12}O_{19}$ having magnetoplumbite structure will be discussed in detail.

2.2.1 Hexagonal Ferrites and Barium Hexaferrite

Hexagonal ferrites are family of related compounds having both hexagonal and rhombohedral symmetry instead of a single structure type. Other than magnetoplumbite of approximate formula $PbFe_{7.5}Mn_{3.5}A1O_5Ti_{0.5}O_{19}$, natural isomorph of $BaFe_{12}O_{19}$, all other hexagonal ferrites are synthetic [33].

Barium hexaferrite ($BaFe_{12}O_{19}$) is an ‘‘M-type ferrite’’ as they are based upon the hexagonal magnetoplumbite, or M-structure. Its crystal structure is very complex with both cubic and hexagonal close-packed layers that are composed of Ba^{2+} and O^{2-} ions. A hexagonal ferrite unit cell having lattice parameters of a = 5.892 Å and c = 23.183 Å contains two formula units, a total of 64 ions [36, 39]. In the barium hexaferrite structure S, R and T blocks in which O atoms are arranged in a close packed structure form the basis of the structure as shown in Figure 2.11. The S unit

is constructed by two formula units $MeFe_2O_4$ having the spinel structure that is composed of two tetrahedral and four octahedral cation sites. The R block has $(BaFe_6O_{11})^{2-}$ stoichiometry and composed of three octahedral sites of two different types and one bipyramidal, five-fold cation site and 12-fold sites in which Ba^{2+} occupies an O^{2-}. The T unit has four layers where Fe ions occupy two octahedral sites and six octahedral sites of two different types having the formula of $Ba_2Fe_8O_{14}$. The block lengths of S, RS and TS blocks are 4.81 Å, 11.61 Å and 14.52 Å, respectively [37]. The unit cell of the M structure includes two formula units as $BaFe_{12}O_{19}$ and includes the unit block RSR*S*, where the asterisks indicate a 180° rotation with respect to the c-axis (Figure 2.11).

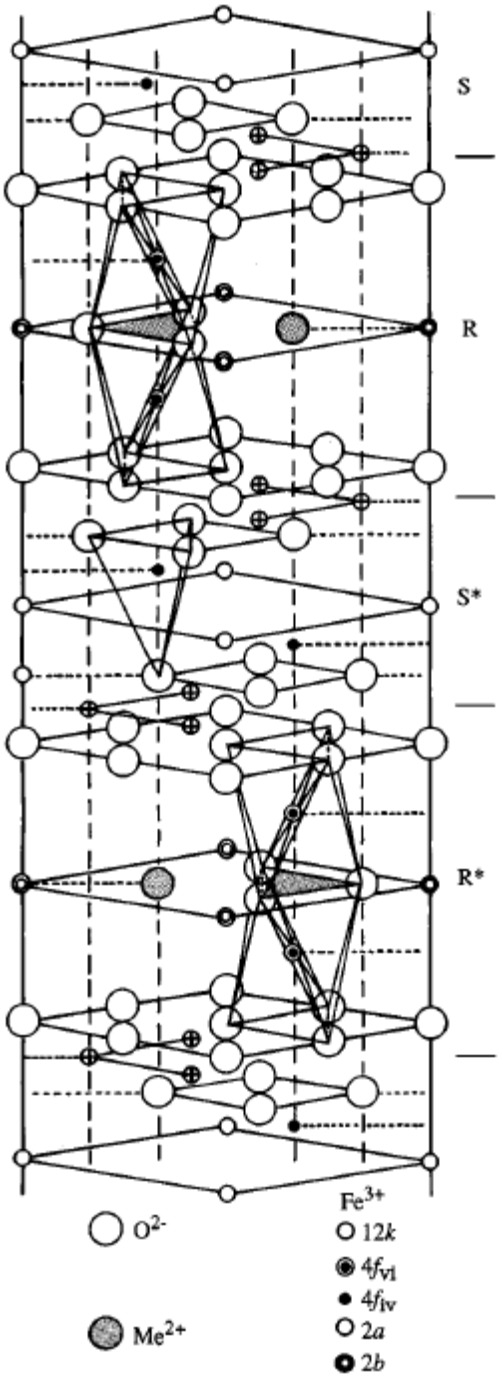

Figure 2.11 Unit cell of $BaFe_{12}O_{19}$ showing the polyhedra coordination for Fe in f_{iv} and f_{vi} sites on which the common faces of two neighbouring f_{iv} and f_{vi} polyhedra are hatched [38].

In this structure $(BaFe_6O_{11})^{2-}$ group forms the RS blocks while $(Fe_6O_8)^{2+}$ forms the S block that does not contain any Me cations. The close packed oxygen

arrangement has cubic symmetry in the S units while hexagonal symmetry in the R blocks. The (111) spinel axis coincides with the hexagonal axis. M structure has the space group of $P6_3/mmc$ in which Fe ions occupy five types of crystal site: three non-equivalent octahedral sites, tetrahedral sites and bipyramidal, fivefold sites as summarized in Table 2.2 [33].

Table 2.2 Five cation sublattices in the magnetoplumbite structure [33].

Sublattice	Number of sites	Symmetry	Block
k	12	Octahedral	R, S
f_{vi}	4	Octahedral	R
a	2	Octahedral	S
f_{iv}	4	Tetrahedral	S
b	2	Five-fold	R

These five crystal sites are 12 octahedral *k*, four octahedral f_{vi}, two octahedral *a*, four tetrahedral f_{iv} and two five-fold *b* sites (Table 2.2). R and S blocks share the 12 Fe sites in the *k* sublattice. Four f_{vi} form a (Fe_2O_9) group of two octahedra sharing a face in the R block that is close to the Ba^{2+}. Both two octahedral *a* sites and four f_{iv} tetrahedral sites are located in the S block. Two *b* sites having five-fold symmetry are quite uncommon in ferric oxides. Therefore, they are built by two tetrahedra that are sharing a face and are occupied by only one cation. According to a detailed X-ray diffraction study [39] these Fe ions are in a double-well potential of width 0.17 Å at each side of the center rather than being in the centre of the bipyramid [33].

Hexagonal ferrites exhibit magnetic properties, since nine of the 12 Fe^{3+} ions in a formula unit are on octahedral sites, two on tetrahedral sites and one on a five-coordinated site. Spins of seven ions on octahedral sites and one ion on a five-coordinated site are directed in one sense, and the remainders are oppositely directed. Therefore, there are four more atoms in one direction meaning 20 unpaired spins per formula unit (since each Fe^{3+} ion contains five electrons with parallel spins) causing a saturation magnetization of 20 μ_B per cell volume.

When compared to the other oxides, $BaFe_{12}O_{19}$ has a high magnetic anisotropy (Table 2.3) with its ‘‘preferred direction of magnetization’’ (‘‘easy’’ direction) along the c-axis. In order to increase the magnetic properties, especially coercivity of barium hexaferrite, several substitutions like Sr and Al are made for Ba and Fe, respectively [36, 40].

Table 2.3 Room temperature anisotropy constants of some important ferrites [36].

Ferrites	K_1/kJm^{-3}
Fe_3O_4	-11
$Mn_{0.98}Fe_{1.86}O_4$	-2.8
$Co_{0.8}Fe_{2.2}O_4$	+290
$NiFe_2O_4$	-6.2
$CuFe_2O_4$	-6
$Mn_{0.45}Zn_{0.55}Fe_2O_4$	-0.38
$Ni_{0.5}Zn_{0.5}Fe_2O_4$	-3
$BaFe_{12}O_{19}$	+330

2.3. Barium Hexaferrite Platelet Synthesis

There are mainly two methods for the synthesis of barium hexaferrite platelets that are chemical methods and molten salt method. The most important and applicable chemical methods are sol-gel, hydrothermal and co-precipitation synthesis. The advantage of chemical methods is the high purity products at low temperatures together with the quasi–atomic dispersion of components in a liquid precursor facilitating the synthesis of crystallized powder with submicron particles [41]. For the production of textured ceramics; however, micron size particles are required. Meanwhile, molten salt synthesis by which reactions occur at low temperatures in molten salt medium is the best method for the production of such materials. Alternatively, BaHF platelets can be produced in two-step process by reactive template grain growth (RTGG). In the first step, seed crystals are synthesized to be used as templates in the subsequent RTGG process.

2.3.1. Chemical Methods

2.3.1.1. Sol-Gel Synthesis

Sol-gel method is a conventional and attractive technique for the synthesis of nanosized particles. It is advantageous in terms of good stoichiometric control and the production of ultrafine particles with narrow size distribution at relatively low temperatures for short calcination duration. Recently, polyacrylic acid (PAA) has been used as a chelating agent in the sol-gel applications instead of citric acid. Polyacrylic acid contains more carboxylic acid groups to form chelates with homogenously mixed cations which is enhanced by the cross-linked gel when compared with the citric acid. Moreover, it can decrease the prone to the segregation during calcination [42].

Brahma et al. [43] tried to synthesize barium hexaferrite by sol-gel method; however, some residual phases remained within the structure even after sintering at 1100 ˚C. The size of the platelets was about 4.7 μm and the saturation magnetization of these platelets was 20 % less than the platelets produced by conventional methods. They attributed this result to the residual phases remained in the structure.

2.3.1.2. Hydrothermal Synthesis

‘‘Hydrothermal’’ term implies utilization of relatively high temperature and pressure. In hydrothermal synthesis, which involves H_2O as a catalyst or a component, temperatures are above 100 ˚C (less than 200 ºC), and pressures are a few atmospheres (less than 1.5 MPa) [44, 45]. During synthesis saturated vapor pressure of the solution at the reaction temperature and composition makes the process autogeneous in a short reaction interval.

Hydrothermal synthesis method can produce fine platelets as in the case of sol-gel method. Although sol-gel, microemulsion, co-precipitation methods etc. can produce BaHF platelets at low temperatures (below 500 K), some phases like α-Fe_2O_3, γ-Fe_2O_3, $BaCO_3$ and $BaFe_2O_3$ remains within the structure. For the removal of these residual phases, high temperature annealing is required which will lead to growth of the platelets [46].

By hydrothermal method, Yamauchi et al. reported to the synthesis of BaHF fine platelets (~500 nm) within a short time and low temperature (575 K) compared with the conventional method [46]. However, this method is not suitable for the production of large platelets that will be used for the production of textured ceramics.

2.3.1.3. Co-Precipitation Synthesis

Like sol-gel method, co-precipitation is one of the most effective techniques for synthesizing ultrafine ceramic particles having narrow particle size distribution [47].

Hibst [5] produced BaHF platelets by co-precipitation method in the following manner; an aqueous solution of barium chloride and iron (III) chloride are mixed with an excess aqueous solution of sodium hydroxide or sodium carbonate. After the filtration and drying operations, BaHF particles having particle size of 0.1-0.2 μm with narrow size distribution are obtained. Furthermore, temperature dependence of platelet coercive force is less compared that obtained by other chemical methods.

In the study of Iyiel [48], co-precipitation method was used for the production of highly dense and sub-micron size barium hexaferrite platelets. During the synthesis process, iron and barium hydroxides were precipitated successively from a mixed aqueous salt solution leading to highly dense, micron size barium ferrite particles. However, these platelets failed to exhibit characteristic absorption maxima with respect to frequency in magnetic measurements.

2.3.2. Molten Salt Synthesis

Molten salt synthesis (MSS) is a technique by which millimeter-size seed crystals can be synthesized at low temperatures, yet higher than those of the above-stated methods [14]. Because of the small diffusion distances of oxide mixtures in molten salts, high surface reactivity of salts and high mobility of species reactions can be completed in a relatively short time [15]. In addition to low temperatures of formation, molten salts can stabilize various polymorphs when compared to other

methods of synthesis [16]. Therefore, MSS has been widely used to form complex perovskite materials, like PZT [15, 49], ferrites [50], $PbNb_2O_6$ [51], PFN [51], PMN-PT [52, 53] and PLT [54]. In molten salt synthesis method specifically reaction mechanism of $BaCO_3$ and Fe_2O_3 to form $BaFe_{12}O_{19}$ is different from that of the solid-state reaction due to the existence of liquid salt medium. Figure 2.12 shows reaction mechanism in molten salt.

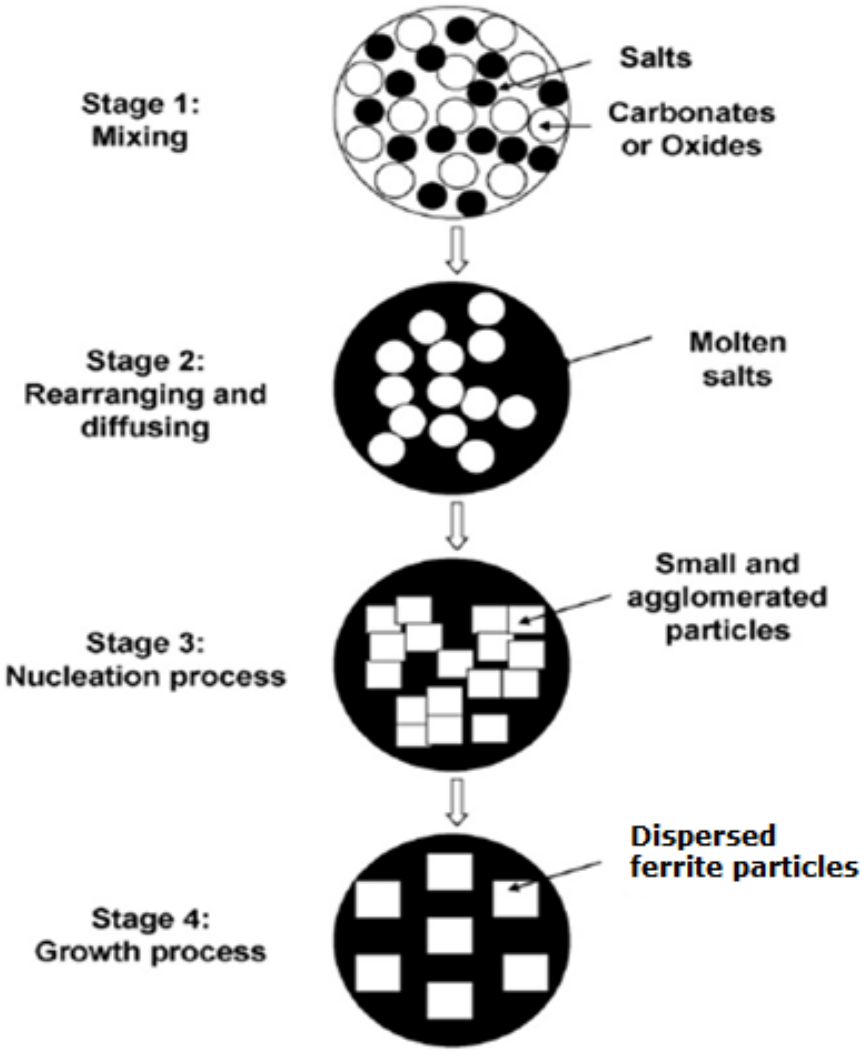

Figure 2.12 Schematic illustration of the main processing stages in the molten salt method [55].

In molten salt synthesis method, raw materials (oxides or carbonates) in stoichiometric amounts are mixed homogenously with one or two kinds of salt.

Then, this mixture is heated above the melting temperature of the salt or salt mixture so that it can melt and form liquid medium. Esin et al. state that Fe_2O_3 and other oxides dissolved easily in the molten chlorides of IA and IIA metals [57]. At the calcination temperature in the salt flux, rearrangement of the oxides occurs and then ions start to diffuse in the liquid medium. With the further calcination, nucleation and growth occurs resulting in the formation of barium hexaferrite platelets [41].

It is fact that due to the limited thermal activation at low temperatures diffusion kinetics and reaction rates are slow [14]. In order to decrease the reaction durations and improve the kinetics, calcination should occur at higher processing temperatures [58]. This situation is for the solid state reaction based synthesis methods like mixed oxide method. In the case of MSS; however, reaction rates and kinetics is faster as the mass transport occurs in the molten salt enabling the calcination at modest temperatures with feasible rates [58]. There are three main steps of MSS that are (i) mechanical mixing of the salt and oxides, (ii) melting of the salt and homogenization of the constituents in the melt and (iii) heat treatment for the nucleation and growth of the desired phase [56]. The two fundamental requirements for MSS are: (i) the proper choice of oxides that will give the resultant compound at the end and (ii) the use of suitable lower melting temperature fluxes which will assist the reactions to occur at a low temperature. The choice of the fluxes is critical, since the salts should not react with both the raw materials and resultant compounds (negligible solid solubility in the oxides), should have low melting temperatures to form liquid medium and should be removed easily after the reaction [58]. MSS parameters such as type of the salt(s), salt to oxide ratio, initial particle size of the raw materials, calcination time and temperature are important, as they have a direct effect on the morphology and size as well as aspect ratio of the final products [56].

Naik et al. and Beretka et al. studied the solid state reaction between $SrCO_3$ and α-Fe_2O_3 for permanent magnets [59, 60]. In the case of molten salt synthesis of $BaFe_{12}O_{19}$ with raw materials $BaCO_3$ and α-Fe_2O_3, it was reported that individual fine crystals were obtained in a $BaCO_3$-Fe_2O_3-NaC1-KC1 flux system [61], and salt-flux accelerated the formation process of barium ferrite particles [5, 62]. Sakai

et al. [63] studied the effect of NaCl molten salt on the compound formation extensively and showed that during molten salt synthesis of the barium hexaferrites the increase of coercivity and saturation magnetization occurs simultaneously in the presence of NaCl, and almost all of the starting materials are converted into barium ferrite. On the other hand, in the absence of NaC1, the increase in saturation magnetization begins at a higher temperature than the increase in coercivity. This may be the indication of contact of the oxides and successive spread within the flux. In the absence of NaCl, $BaFe_{12}O_{19}$ forms after the formation of $BaFe_2O_4$, whereas, On the other hand, $BaFe_2O_4$ cannot be identified in the presence of NaCl. Moreover, it was shown that both saturation magnetization and coercivity increase considerably with the addition of NaCl in amounts as low as 2%. Additionally, due to the enhanced reaction rates α-Fe_2O_3 and $BaCO_3$ react to form complete barium ferrite at temperatures above 800 ℃, since the activation energy for barium ferrite formation is reduced by adding NaCl salt. In other words, NaCl acts as a catalyst for barium ferrite formation.

Hsiang and Chang [64] suggested that solubility of BaO in sulfide molten salt was higher than that of Fe_2O_3 leading to earlier precipitation of Fe_2O_3 as a spinel phase. Molten salt saturation with BaO is hindered when the salt amount increases resulting in the appearance of only the spinel phase.

2.3.3. Reactive Templated Grain Growth (RTGG) Process

In reactive templated grain growth (RTGG) processing, anisotropic particles having simpler composition and processing path than the target material are used as a raw material. During RTGG, starting materials (templates) are transformed into the final material that will have the crystallographic texture of the templates (Figure 2.13). This process is an old way of producing cordierite honeycomb having high thermal shock resistance and magnetic spinel ferrite heads having high friction resistance. RTGG is one of the most effective ways of the production of textured lead-free piezoelectric ceramics [65]. However, if the required conditions for RTGG are satisfied, this process can be applied to all the ceramic systems.

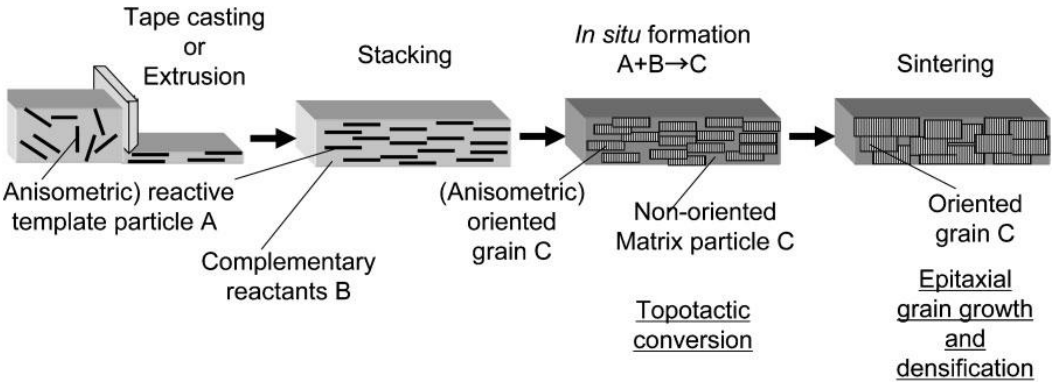

Figure 2.13 Schematic illustration of the RTGG process [65].

Templates that are synthesized before-hand are mixed with the stoichiometric amount of powders and aligned with a shear force (ie. tape casting, extrusion) to start with the reactive templated grain growth method. During the calcination of the green ceramics, reaction occurs to produce the final material preserving the direction of template alignment [66, 67].

This method is the easy way of producing textured ceramics with appropriate composition for directional growth. For RTGG to occur the crystal structure of the reactive template material should be similar to that of the final textured material. Furthermore, following conditions should be satisfied for RTGG to occur [66]:

1. Template particles should be in anisotropic shapes.
2. Thermodynamically feasible reaction should be occurring from template and other reactants to the resultant ceramic.
3. Epitaxy and topography of templates and the resultant ceramics should be matching.
4. Since the intermetallics may cause some mismatch problems between the template and the resultant ceramic, their formation should be avoided.

2.4. Production of Textured BaHF Ceramics by Templated Grain Growth (TGG) Phenomenon

There is vast literature on texturing of the microstructure of ceramics [68–71]. Microstructure texturing has been achieved by using anisotropic shaped particles

under compaction, forging or strong magnetic field generally at high temperatures [68]. Templated grain growth (TGG) that is first reported by Seabaugh et al. [72] is an alternative way of textured ceramic production. As well as being able to process large group of materials and flexibility in shaping, TGG provides higher degrees of texture when compared to the other methods [73].

Templated grain growth (TGG) is a technique developed for both morphologic and crystallographic texture in ceramic bodies in order to reveal anisotropic and novel properties. The process, shown schematically in Figure 2.14, is simple and attainable for a wide range of systems [74].

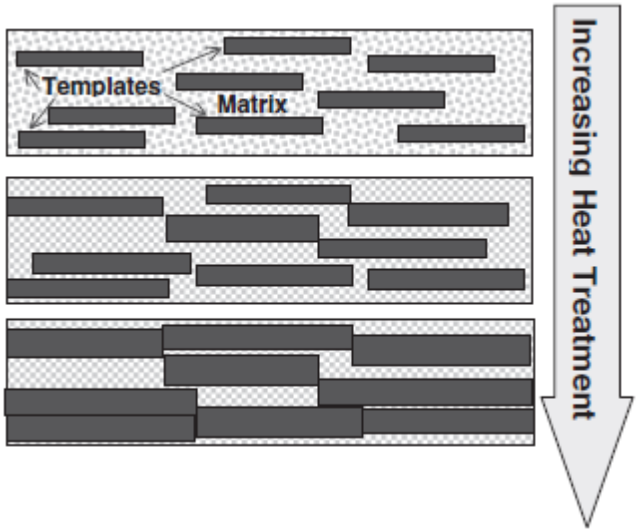

Figure 2.14 Schematic illustration of the TGG process [74].

Template particles (seed crystals) having large anisotropic shape are added to a small size powder matrix. The template content should not exceed 10 vol.% for the minimization of negative effects caused by the large templates like limited sintering. TGG occurs in two steps [75]: In the initial stage, forming process (e.g. tape casting, slip casting, extrusion, uniaxial pressing) causes the small fraction templates to align in the fine matrix. In the second step, thermal processing is applied to the green ceramic including oriented particles. The oriented large anisotropic particles begin to grow at the expense of the matrix leading to densification during thermal processing. The growth is driven by the difference in

surface free energy between the matrix and the larger template grains similar to a typical grain growth process. Thermal treatment increases the amount of texture, since grains are oriented more with the grain growth. Grain growth proceeds until the hindrance of grains by each other or decrease of the driving force due to coarsening. Earlier studies of TGG indicated that presence of chemically stable template particles, the alignment of the template particles during forming, a fine matrix grain size and a dense matrix are critical requirements for obtaining high quality texture by TGG [72, 76].

In TGG, grain growth is driven by the anisotropic grain boundary energies rather than curvature observed in most of the ceramics. In order to maximize the area of low energy faces that are perpendicular to the c-axis, lateral growth of the platelets is preferred. Since the boundaries between powders and platelets are high angle and high energy boundaries relative to the platelet surfaces, small and randomly distributed powders are consumed by the large orientated templates. Up to now, TGG which is the preferential growth of large anisometric grains at the expense of a fine matrix has been addressed for Al_2O_3 and SiC. Growing template particles decide the degree of texture in the final microstructure, as they have a size advantage with respect to the matrix powders. Despite the existence of the anisotropic matrix powders, texture will be in the growth direction of the larger grains. For TGG to occur templates and matrix should have some size difference, because matrix grains which are too large to be consumed will be misaligned and impede the alignment of the microstructure [77].

Besides the growth of the template particles, grain rotation is another phenomenon that can improve texture in the ceramic systems. Grain rotation or face to face orientation that is driven by the low energy faces of the crystals as a result of asymmetric shapes is suggested to occur at the early stages of the sintering. As evidence to particle rearrangement, densification of anisotropic particles can be shown. In the TGG phenomenon, fine matrix particles will be in contact with the low-energy faces of the large template particles. Favorably positioned powders rotate to share the low-energy surface and influence the rotation of other small grains that are further from the template interface [77].

Templated grain growth was first reported by Seabaugh et al. in a liquid-phase sintered, sol-gel based system as a function of template and liquid phase content as well as sintering time and temperature [72]. Moreover, Suvacı et al. showed that TGG occurs in three stages [78]: densification, rapid growth of template particles in the radial direction until template impingement and slower growth due to template thickening [79]. During first step of templated grain growth, densification, there will be either very little or no template growth. Texture development is controlled by the growth of the template particles instead of template rearrangement or the texture in the matrix [79, 80]. Degree of texture and template growth is mainly controlled by the initial geometry determined by template concentration. Suvacı and Messing observed that template growth occurs only at densities higher than 90% of the theoretical density. For the operation of TGG, there should be at least 1.5 times size difference between the radial direction of the platelets and matrix powders in order to preserve suitable kinetic and thermodynamic conditions [79]. Besides, the template and matrix powders should have similar crystal structure with lattice mismatch less than 15%, they should be in thermodynamic and kinetic stability, and finally, it is critical that the template to have an anisotropic morphology [81].

In the present study, a small number of large anisotropic barium hexaferrite platelets (i.e. templates) are aligned in a fine barium hexaferrite powder matrix by tape casting.

2.5. Characterization of Texture

For many years, texture (preferred orientation) in the polycrystalline materials has been studied on different systems [82]. In literature, the preferred orientation can be classified as “deformation texture” and “recrystallization (or annealing) texture”. Microstructural texture may be resulted from the processing steps like heat treatment, casting, welding etc. [83]. In 1924, preferred orientation in a metal was reported by pole figures obtained by using Laue XRD method by Wever. In addition, Cullity plotted the stereographic projections of {100} poles of 10-grained

cubic metal. There obtained 30 poles on the stereographic projection as each of the grains has three {100} pole. If the grains are distributed randomly, poles will distribute homogenously on equal areas on the sphere. In the case of preferred orientation, poles are seen as clusters in certain areas. Figure 2.15 show the stereographic projection of the cubic metal having randomly distributed and preferentially oriented grains.

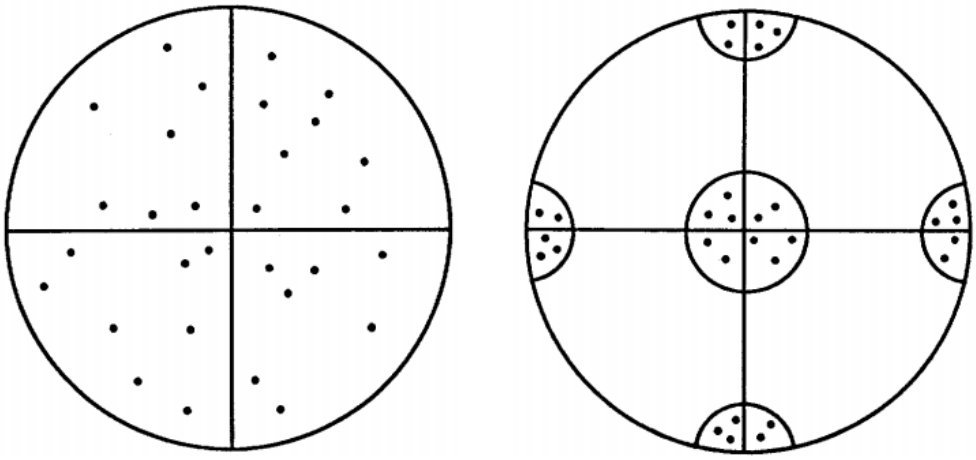

Figure 2.15 Stereographic projection of (100) pole figure showing (a) the random distribution, (b) the preferred orientation (Cullity)

In order to model the preferred orientation, orientation distribution function (ODF) (f(g)) that is defined as in Equation 2.1 was investigated by Bunge (1985).

$$^{\delta}V/V=f(g)\ ^{\delta}g \qquad (2.1)$$

where $^{\delta}V/V$ is the crystallite volume fraction, g is the orientation angle and $^{\delta}g$ is the orientation element.

If all the crystallite orientations occur with equal probability, isotropic polycrystalline materials will be resulted showing the random distribution. However, some extent of deformation will lead to the demolition of isotropic structure as a result of mechanical fibering in certain orientations. For some applications polycrystalline material behaves as single crystal in the case of ‘‘cube texture.’’

Generally, pole figures and inverse pole figures which are obtained by X-ray diffraction are used for the detection of degree of texture in polycrystalline materials. However, they have a drawback related with 2-D data for 3-D crystallographic spaces. Orientation Distribution Function (ODF) is another tool for texture characterization. It is more accurate in the investigation of individual texture components when compared to the pole figures. On the other hand, for the local texture characterizations, electron back scattered diffraction (EBSD) by scanning electron microscopy (SEM) and electron diffraction patterns by transmission electron microscopy (TEM) can be utilized [84-87].

2.5.1. Representation of Texture in Materials

In hexagonal materials, texture can be represented as {hkl}<uvw> where {hkl} is the plane that is parallel to the sheet plane and <uvw> is texture direction. If the texture is simple, it can be represented by pole figures built up by simple X-ray diffraction techniques. In the case of complex preferred orientations, X-ray diffraction is not adequate due to the semi-quantitative results. It is necessary to calculate orientation distribution function for the complete analysis of preferred orientation; however, it cannot be obtained directly from simple X-ray diffraction methods and need further derivations from pole figures.

2.5.1.1. Pole Figures

The pole figure is the stereographic projection in 2-D on which the pole distribution and orientation for a selected set of planes {hkl} can be shown. The most conventional way of pole figure measurement is the 'Schultz reflection method' which is shown schematically in Figure 2.16. The goniometer is designed for the alteration of two Euler angles, β and φ, and the Bragg angle θ that is fixed for the detection of spatial distribution of one type of diffraction plane (hkl) [88, 89]. Scanning of direct space can be achieved by rotation around the β and φ axes without the loss of the Bragg angle θ for the same (hkl) diffracting planes. Moreover, for an azimuthal angle $\varphi = 0$, scanned volume can be defined.

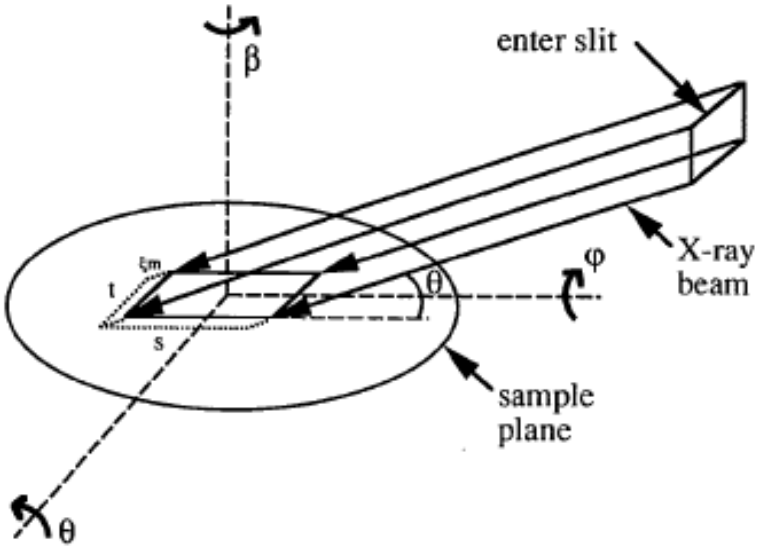

Figure 2.16 Schulz reflection method showing the scanning principles for the texture analysis [88].

2.5.1.2.Orientation Distribution Function

Since pole figures cannot give exact information about texture, orientation distribution functions (ODF) that can describe the occurancy frequencies of certain orientations in three dimensional space are utilized. Three Euler angles showing the angle between crystallographic axes (a1 or c-axes) and the specimen axes define this three dimensional space. Euler angles can be defined by both Roe system [90] and Bunge system [91] (Figure 2.17).

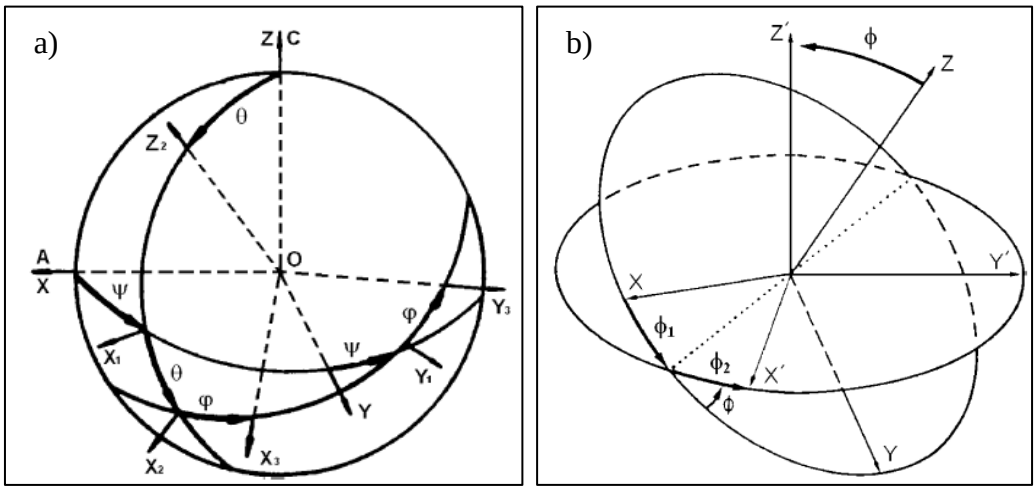

Figure 2.17 Illustration of the Euler angles (a) ψ, θ, φ in accordance with the Roe system [88] (b) ϕ1, ϕ, ϕ2 in accordance with the Bunge System [91].

In Roe system rotating ODF (f(g)) can be defined by Euler angles of ψ, θ, φ;

$$g=\{ \psi, \theta, \varphi \} \tag{2.2}$$

In the Bunge system, Euler space can be defined by Φ1, Φ, Φ2. Moreover, orientation distribution function can be described as;

$$dV/V = f(g)dg \tag{2.3}$$

where dV represents the volume elements of the sample having the orientation g within the element of orientation dg which is defined as in Equation 2.4.

$$dg=1/8\Pi^2 \bullet \sin\theta \bullet d\psi \bullet d\theta \bullet d\varphi \tag{2.4}$$

Generalized spherical harmonics representation of orientation distribution function is as follows [92]:

$$f(\psi,\theta,\varphi)=\sum_{l=0}^{\infty}\sum_{m=-l}^{+l}\sum_{n=-l}^{+l}W_{lmn}Z_{lmn}(\xi)\cdot\exp(-im\psi)\exp(-in\varphi) \tag{2.5}$$

where W_{lmn} is the coefficient of spherical harmonics, $\xi=\cos\theta$ and $Z_{lmn}(\xi)$ is associated with Jacob function.

2.5.1.3.Rietveld Analysis

Due to some deficiencies of above stated methods that are related with showing the distribution in crystal orientations and the correlation between the model equations and the processing variables, Rietveld Analysis has been used extensively [93]. For a Rietveld refinement, appropriate diffraction data collection is required. Before the data collection, factors such as diffractometer geometry, the instrument alignment, calibration quality, suitable radiation type (e.g. conventional X-ray, synchrotron X-ray or neutron), wavelength, appropriate sample preparation and thickness, slit sizes, and necessary counting time should be all adjusted correctly [94].

Pole figure measurements have been used for the texture analysis. Monochromatic X-ray or neutron diffraction is used for the construction of pole figures. During pole figure measurements, a detector is located on the center of a diffraction peak and the sample is rotated into various orientations. This is an efficient way of texture measurement only if a few pole figures of different planes are needed for the texture analysis, the intensities of peaks are reasonable and diffraction peaks are well separated. In the case of pole figure measurement of complex diffraction peaks and multi-phase materials, overlapping peaks may lead to the unreasonable results.

As a result of restriction in the texture analysis due to the complex diffraction patterns, crystallographers have developed a novel approach to crystal structure analysis. Rietveld (1969) investigated a texture analysis method on continuous powder patterns and his method is implemented in several software packages [e.g. DBWS (Wiles & Young, 1981), GSAS (Larson & Von Dreele, 1986), Fullprof (Rodriguez-Carvajal et al., 1991) and MAUD (H. R. Wenk, S. Matthies and L. Lutterotti, 1994)].

In Rietveld refinement, although there are many ways to handle texture effects, two methods defined by Bunge and Le Bail are the most popular ones. The first method is defined by Bunge (1969), and based on the ODF with generalized spherical harmonics and deciding the finite number of coefficients like crystallographic

parameters that are refined with a non-linear least-squares procedure (Popa, 1992; Ferrari & Lutterotti, 1994; Von Dreele, 1997). Second method is defined by using Le Bail algorithm [95] and based on the direct use of ODF to obtain pole figures. It is a discrete method since crystal structure and texture refinement are carried out separately. Le Bail algorithm is used to calculate ODF and the intensity fluctuations as a result of texture can be computed by pole figures. This method requires the knowledge of only the space group and cell parameters rather than crystal structure [96].

2.5.1.3.1. March-Dollase Function

In order to define the orientation distribution of the anisotropically shaped particles, March developed an equation [97] which is adjusted to Rietveld refinements by Dollase [91]. In order to study the microstructures having different degrees of texture in materials, March-Dollase equation [98] can be used [93].

Since there are two parts within the material, one is oriented templates and the other is random part, March-Dollase equation (Equation 2.6) includes the volume fraction of textured part *f* and texture factor *r* giving the effective sample compression or extension along the cylinder axis due to preferred orientation. ω is the angle between preferred orientation direction and the normal of the textured planes [93].

$$P(f,r,\omega) = f\{r^2\cos^2\omega + r^{-1}\sin^2\omega\}^{-3/2} + (1-f) \qquad (2.6)$$

If there is no preferred orientation then r=1.0. For the case of flat plate sample, *r* will be less than one since platy crystals are expected to pack normal to the diffraction vector. Since *f* is the fraction of crystallites that are associated with a particular orientation axis, summation of all the f values of textured planes should be 1.

The same intensity correction in GSAS (General Structure Analysis System) program can be made by another formula given in Equation 2.7:

$$I_{corr} = I_{obs}\left(G^2\cos^2 a_k + \frac{1}{G}\sin^2 a_k\right)^{-3/2} \quad (2.7)$$

I_{obs} and I_{corr} values are measured intensity and the corrected intensity for preferred orientation, respectively. a_k is the acute angle between the scattering vector of reflection k and the orientation direction; *G* is the March coefficient. Similar to *r*, *G* ranges from 0 to 1, where zero refers to 100% preferred orientation and one refers to completely random distribution.

In the case of the hexagonal structured platelets, the strongest reflections will be coming from (00l) while the weakest ones from (110) [99]. *Leventouri* [99] calculated the relation between intensity ratios of (006) and (110) planes and resulting March coefficients. Equation 2.8 shows this relation:

$$I_{006} / I_{110} = 0.10953 G^{-4.701} \quad (2.8)$$

This equation means that with the increase in intensity difference between (006) and (110) planes, G decreases and degree of texture increases.

2.5.1.3.2. Spherical Harmonics Function

In the intensity formula a correction factor K exist in which A(h, y) is a factor describing the change in Bragg intensity for a reflection due to texture. This texture correction factor is dependent on both reflection, h and sample orientation, y as shown in Equation 2.9 [100].

$$A(h, y) = 1 + \sum_{l=2}^{L} 4\Pi / (2l+1) \sum_{m=-l}^{l} \sum_{n=-l}^{l} C_l^{mn} k_l^m(h) k_l^n(y) \quad (2.9)$$

In the case of cylindrical sample symmetry (fiber texture) only $k_l^n(y)$ terms are nonzero so the rest are excluded from the summations and the set of C_l^{m0} coefficients is sufficient to describe the effect on the diffraction patterns due to texture. L is determined by the magnitude and complexity of the texture as well as

the quality of the diffraction data. The crystal harmonic factor, $k_l^m(h)$, is defined for each reflection, h, via the polar and azimuthal coordinates (φ,β) of a unit vector coincident with h relative to the reciprocal lattice. For most crystal symmetries, φ is the angle between h and the n^{th}-order major rotation axis of the space group (usually c_0) and β is the angle between the projections of h and any secondary axis (usually a_o) onto the normal plane [101]. In a similar way, the sample harmonic factor, $k_l^n(y)$, is defined according to the polar and azimuthal coordinates (ψ,γ) of a unit vector coincident with the diffraction vector relative to a coordinate system attached to the external form of the sample [102].

2.5.2. Texture Components in Materials

2.5.2.1.Fiber texture

When an extrusion process is applied uniaxially, all the basal plane normals [001] are perpendicular to the extrusion axis. This is also called as ‘‘cylindrical texture.’’

2.5.2.2.Rolling texture

Metals and alloys with c/a ratios approximately equal to the ideal c/a ratio of 1.633, such as Mg, tend to form basal fiber textures during rolling. Metals and alloys having hexagonal structures with c/a ratios above the ideal (1.633), such as Zn (1.856) and Cd (1.885), tend to exhibit textures with basal poles tilted ±15–25° away from the normal direction toward the rolling direction, the $[11\bar{2}0]$ poles aligned with the rolling direction, and the $[10\bar{1}0]$ directions pointed parallel to the transverse direction. Such textures are due to the combination of basal slip and large-scale twinning [83].

Metals and alloys, possessing c/a ratio less than 1.633 such as Zr (1.589) and Ti (1.587), tend to form textures with basal poles tilted ±20–40° away from the normal direction toward the transverse direction, the $[1\ 0\ \bar{1}\ 0]$ poles aligned with the rolling direction, and the $[11\ \bar{2}\ 0]$ directions pointed parallel to the transverse direction [83].

2.5.2.3.Recrystallization texture

Recrystallization is similar to the phase transformation in deformed materials in such a way that both can lead to drastic changes in texture. The principal differences are (i) the “nuclei” in the case of recrystallization already exists in the deformed microstructure; and (ii) phase transformation causes a definite orientation relationship between the deformed and recrystallized materials; however, recrystallization does not. There is no report on the quantitative orientation relationship between parent grains and recrystallized ones. When the second phase particles exist in high volume fraction, there may not be any texture related with the recrystallization [83].

CHAPTER 3

EXPERIMENTAL PROCEDURE

3.1. General Procedure

In this study, both barium hexaferrite (BaHF) powders and platelets are required for the production of textured ceramics. BaHF powders were synthesized by ‘‘mixed oxide technique’’ while platelets were synthesized by both ‘‘molten salt synthesis (MSS)’’ and ‘‘reactive templated grain growth (RTGG)’’ methods. In order to obtain BaHF from Fe_2O_3 and $BaCO_3$ completely, 1 mole of Fe_2O_3 and 5.3 moles of $BaCO_3$ composition were used [103,104]. For the powders, precursors were calcined in two steps; first at 1040 ˚C for 5 hours and secondly at 1050 ˚C for 7 hours resulting in submicron size particles. For the platelets synthesized by MSS, precursors were synthesized in a flux medium (KCl, NaCl or combination of both) at 850, 900 and 950 ˚C for 1, 2, 2.5 and 3.5 hours. Since these platelets had maximum size of 3 μm, they were not properly capable of functioning as seed crystals for further templated grain growth (TGG) studies. Therefore, alternatively, within the context of RTGG method, bismuth ferrite templates were synthesized first, and they were used to produce platelet-shaped barium hexaferrite templates. For the production of textured bulk BaHF ceramics, tape casting method in which synthesized powders and platelets were directed leading to a texture in this direction by TGG was utilized.

BaHF powders, platelets synthesized by MSS and RTGG methods and textured bulk ceramics produced by tape casting were characterized by X-ray diffraction

(XRD) and scanning electron microscopy (SEM) techniques. Additionally, in order to investigate effect of flux type and composition as well as calcination time and temperature on the morphology, size and growth mechanism of BaHF platelets during the platelet synthesis by MSS, inductively coupled plasma-mass spectroscopy (ICP-MS) studies were conducted. For the determination of degree of texture achieved in BaHF ceramics, Rietveld analyses, pole figure measurements and EBSD studies were carried out.

3.2 Experimental Technique

3.2.1 Preparation of Ferrite Powders

Powder ceramics are produced by various methods like sol-gel, hydrothermal, co-precipitation, mixed oxide etc. [6]. Among them mixed oxide method is the simplest one, since it basically includes only mixing and calcining the precursors. Furthermore, synthesized powders have the potential of showing maxima in their loss factor spectrum [105-108].

Figure 3.1 shows the applied processing steps of barium ferrite production by mixed oxide method. High purity powders of Fe_2O_3 and $BaCO_3$ (Merck GmbH) were used as the raw materials.

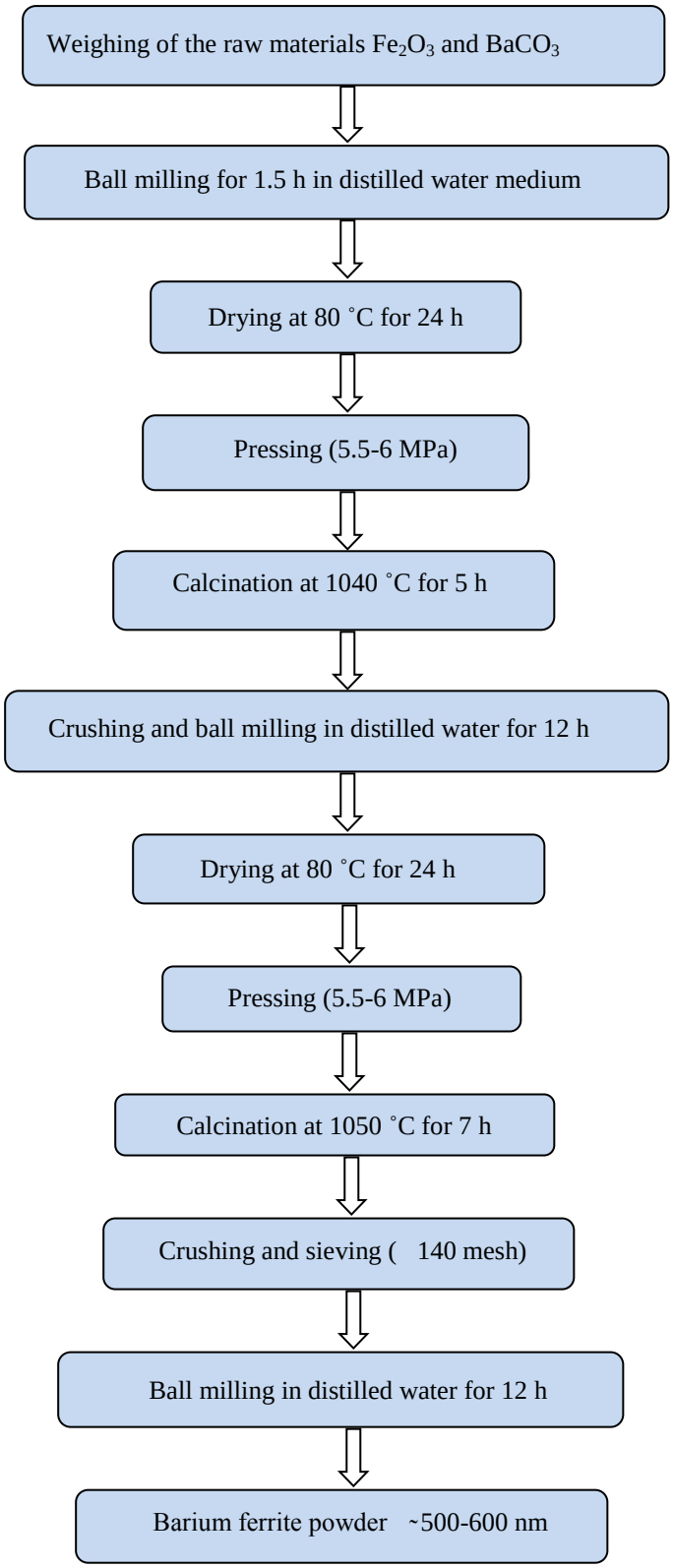

Figure 3.1 Flowchart of barium ferrite production.

Fe_2O_3 and $BaCO_3$ were ball milled for 1.5 h in previously specified stoichiometry. After drying the mixture, powders were pressed in small amounts (~ 2 g) and calcined at 1040 ˚C for 5 h in a muffle furnace. The pellets were crushed and ball-milled for 12 h for the removal of residual hematite within the structure at the second calcination step. Compaction was applied again and pellets were obtained in order to shorten the diffusion distance. Then, secondary calcination was done at 1050 ˚C for 7 h in the muffle furnace. The reaction taking place during the synthesis can be written as:

$$BaCO_3 + 6Fe_2O_3 = BaFe_{12}O_{19} + CO_2(g) \tag{3.1}$$

After sieving with 140 mesh aperture and ball milling in a polypropylene container for 12 h at 375 rpm, BaHF powders with particle size ranging from 400 to 600 nm (Figure 3.2) were obtained. In all the milling steps, distilled water was used as liquid medium while zirconia balls were used as milling media.

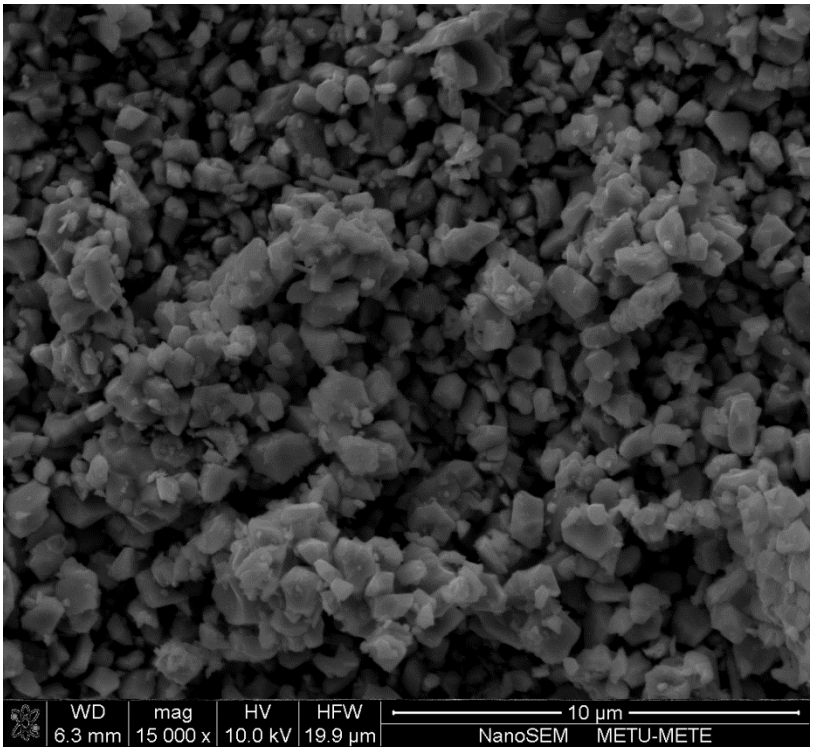

Figure 3.2 Typical appearance of BaHF powders synthesized by mixed oxide method.

For the determination of structure of the powders and quantitative phase analysis, X-ray diffraction method was used. Figure 3.3 shows the XRD of powders in which barium ferrite was determined to be the only phase.

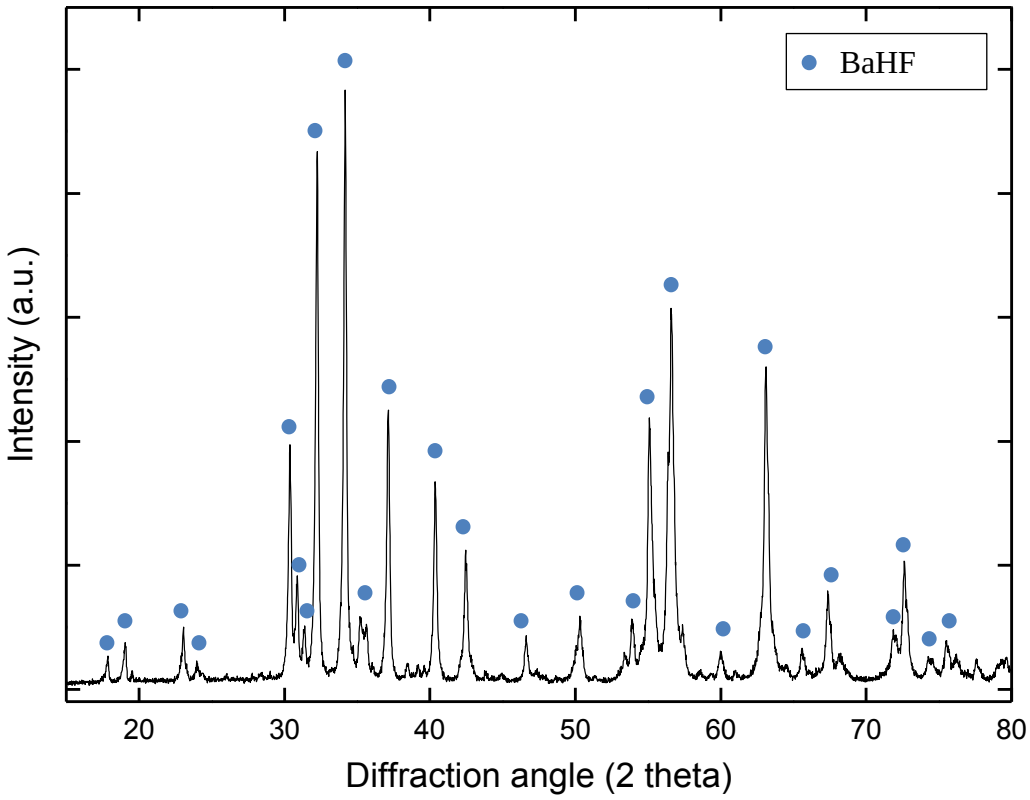

Figure 3.3 X-ray diffractogram of barium ferrite powders synthesized by mixed oxide method. (JCPDS-ICDD card no. BaHF 43-0002).

3.2.2 Preparation of Ferrite Platelets

3.2.2.1 Molten Salt Synthesis

Reagent grade powders of Fe_2O_3 (~ 200 nm), $BaCO_3$, KCl and NaCl (Merck GmbH) were used as the raw materials for synthesizing BaHFs. In order to determine the mechanism of BaHF synthesis, equal amounts of salt (KCl or NaCl) and homogenously mixed oxides ($BaCO_3$ and Fe_2O_3) were put into alumina crucibles and heated to 900 ˚C. In order to prevent formation of other compounds like $BaFe_2O_4$, $BaCO_3$ and Fe_2O_3 were mixed in $BaCO_3$•$5.3Fe_2O_3$ amounts [103, 104]. All the elements were mixed in a mortar for 15 minutes and calcined for 10,

15 and 20 minutes in both molten NaCl and KCl. After each calcination process, mixtures were cooled in air and washed with ultra pure water. The resultant solutions were used for the inductively coupled plasma spectroscopy analyses while the powders were dried at 80 ˚C for 24 h. The samples synthesized in KCl flux for 10, 15 and 20 minutes were labeled as 10K-900, 15K-900 and 20K-900, respectively. Similarly, those synthesized in NaCl flux for 10, 15 and 20 minutes were labeled as 10N-900, 15N-900 and 20N-900, respectively.

In order to study the effect of flux composition on the resulting morphologies and amount of conversion to barium ferrite, 50 wt% flux and 50 wt% oxides (Fe_2O_3 and $BaCO_3$ in 5.3:1 ratio) was used in pure NaCl, 90 wt% NaCl - 10 wt% KCl, 80 wt% NaCl – 20 wt% KCl, 70 wt% NaCl – 30 wt% KCl, 44 wt% NaCl – 56 wt% KCl (1:1 mol), 70 wt% KCl – 30 wt% NaCl, 80 wt% KCl – 20 wt% NaCl, 90 wt% KCl – 10 wt% NaCl and pure KCl (Figure 3.4). Mixture of oxides and salts were put into alumina crucibles and calcined at 850, 900 and 950 ˚C for 1, 2, 2.5 and 3.5 h. After each calcination process, mixtures were washed with distilled water and dried at 80 ˚C for 24 h. Using the SEM images of the synthesized material radii of the platelets were measured.

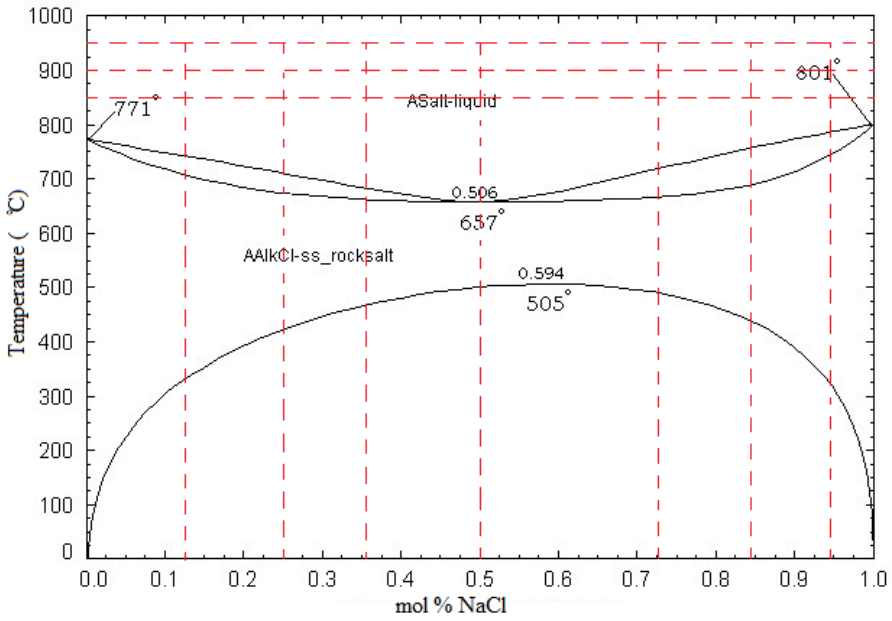

Figure 3.4 Binary phase diagram of NaCl and KCl on which studied compositions and temperatures are labeled [109].

3.2.2.2. Reactive Templated Grain Growth (RTGG) Method

An alternative method based on reactive templated grain growth (RTGG) has been developed to synthesize BaHF platelets. In this method, rod-like $BiFeO_3$ was synthesized first, and it was used as template to synthesize large BaHF platelets. Reagent grade Bi_2O_3 and Fe_2O_3 (Merck GmbH) were used in 3.5 and 1 mol, respectively. They were mixed in a mortar for 1 hour with distilled water and dried in drying oven at 70 ˚C for 18 hours. The mixture was put into an alumina crucible and heated to 850 ˚C with a rate of 0.5 ˚C/min, which was calcined at this temperature for 4 hours. The thermal reaction occurring during the calcination step is as follows (Equation 3.2):

$$Bi_2O_3 + Fe_2O_3 = 2BiFeO_3 \tag{3.2}$$

Calcined material was cooled with 0.5 ˚C/h rate to 700 ˚C in 12.5 days. Following this, the furnace was shut down, and it was cooled in the furnace. Resultant rod-like bismuth ferrite (BiF) ceramics are shown in Figure 3.5.

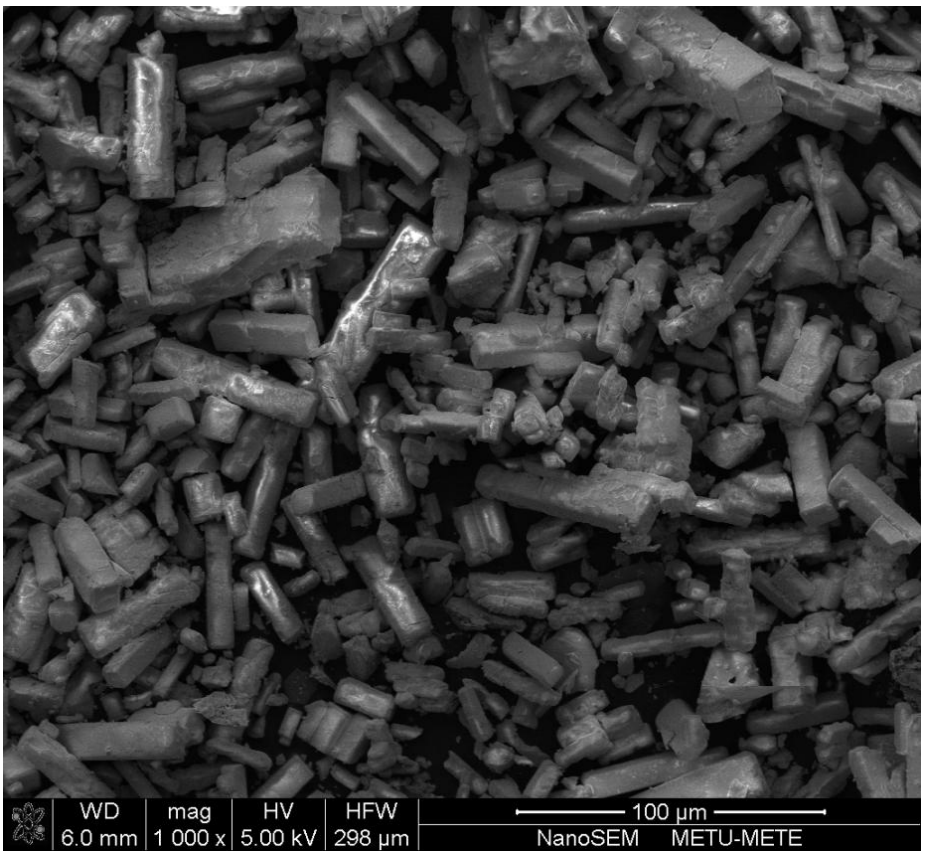

Figure 3.5 SEM image of synthesized bismuth ferrite ceramics.

Second step was to use the synthesized $BiFeO_3$ (BiF) as template to produce BaHF platelets. For this purpose, 10 wt% stoichiometric amounts of BiF-$BaCO_3$ and 90 wt% pre-synthesized BaHF powders were mixed. Equal amounts of powder mixture and polymeric solution based on methyl-ethyl-ketone (MEK) / ethanol were blended with a centrifugal mixer (Thinky, ARE 250, Tokyo, Japan) at 2000 rpm for 10 minutes. Homogenously mixed solution having the viscosity of approximately 10000-20000 cps was tape casted with a tape caster (MSE-TC-200-C, Kocaeli, Turkey). Tape casting speed was 20 cm/sec while the height of the doctor blade (thickness of the tapes) was 300 µm. After deairing for 24 h for the removal of volatile part (MEK and ethanol), tapes were cut in 3 cm x 3 cm squares, which were then layered and stacked in a laminated form. They were compacted under 10 MPa and heated to 600 ˚C with a rate of 1 ˚C/min, where they were soaked for 2 hours for the removal of polymer solution. In order to synthesize

BaHF platelets, compacted laminates were heated to 1050 ˚C with a rate of 4 ˚C/min, kept at this temperature for 10 hours and subsequently cooled in the furnace. The thermal reaction occurring during the heating is given below (Equation 3.3):

$$12BiFeO_3 + BaCO_3 = BaFe_{12}O_{19} + 6Bi_2O_3 + CO_2 \quad (3.3)$$

Calcined laminated structure was crushed smoothly in order not to harm the platelet morphology. Following this, crushed ceramics were washed with 10 % HNO_3 solution at 90 ˚C to remove residual bismuth oxide [110]. Figure 3.6 shows the resultant microstructure after the washing operation.

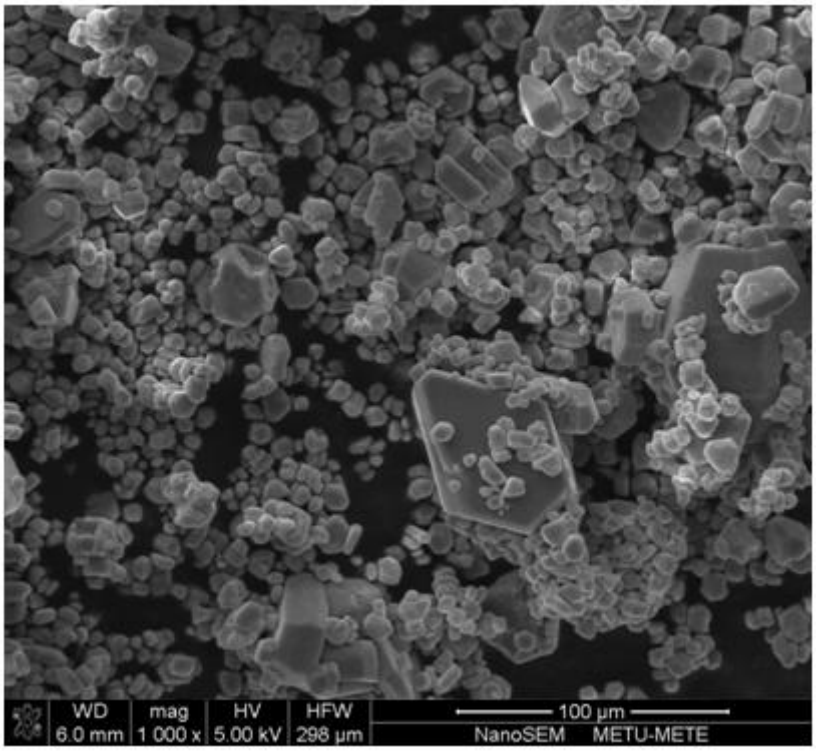

Figure 3.6 SEM image of barium hexaferrite platelets and powders synthesized using the specified route.

3.2.3 Preparation of Textured Ferrite Ceramics

All the textured BaHF ceramics were prepared by tape casting method using TGG phenomenon. The difference between these ceramics is resulted from the platelets synthesized by molten salt synthesis and reactive templated grain growth methods.

3.2.3.1. Preparation of Textured Ferrites by Platelets Synthesized via MSS

In the first case, they were tried to be produced by tape casting using TGG phenomenon. Initial ceramic mixture of tape casting was composed of 8 wt% platelets synthesized by molten salt method and 92 wt% powders synthesized by mixed oxide method. 50 ml of tape casting suspension was composed of 40 ml methyl ethyl ketone based polymer solution and 10 ml oxide mixture. The suspension was mixed using the centrifugal mixer for homogenization at 2000 rpm for 10 minutes. Homogenously mixed solution having the viscosity of approximately 10000-20000 cps was tape casted with the tape caster. Tape casting speed was again 20 cm/sec while the height of the doctor blade (thickness of the tapes) was 300 μm. After deairing for 24 h, tapes were cut in 3 cm x 3 cm squares, which were then layered and stacked in laminated form. Following this, laminates were compacted under 10 MPa and heated to 600 ˚C with a rate of 1 ˚C/min and kept 2 hours at that temperature for the removal of the polymeric solution. For sintering and templated grain growth, laminated and compacted tapes were heated to 1100 ˚C with a rate of 4 ˚C/min, held there for 8 hours and cooled in the furnace.

3.2.3.2. Preparation of Textured Ferrites by Platelets Synthesized via RTGG from BiF Seed Crystals

BaHF ceramic synthesized using BiF template was directly used as the oxide source since it contained high fraction of small powders with small fraction of large platelets. 50 ml tape casting suspension was composed of 40 ml MEK-based polymer solution and 10 ml oxide mixture. The suspension was mixed with the centrifugal mixer at 2000 rpm for 10 minutes. Resultant solution having the approximate viscosity of 10000-20000 cps was tape casted with the tape thickness of 300 μm and casting speed of 20 cm/sec. After deairing for 24 h, tapes were cut

in 3 cm x 3 cm squares, which were then layered and stacked in laminar form. This laminated structure was then compacted under the pressure of 10 MPa and heated to 600 ˚C with the rate of 1 ˚C/min and held 2 hours at that temperature for the removal of polymeric solution. For sintering and templated grain growth, laminated and compacted tapes were heated to 1000 ˚C with 4 ˚C/min rate and calcined for 2 h followed by heating to 1250 ˚C with 4 ˚C/min rate, held there for 5 hours and cooled in the furnace.

3.3 Characterization Studies

3.3.1 Microstructural Characterization

Morphology and size of barium hexaferrite powders and platelets were examined by scanning electron microscope (Nova NanoSEM). All of the studied materials, namely, powders, platelets and textured bulk ceramics were observed directly without metallographic preparation and coating. Since the materials were not coated, observations could be done at relatively low accelerating voltages between 5-10 keV.

3.3.2 Phase Analysis

For the phase analysis, XRD was conducted on the ceramics using Rigaku D/MAX2200/PC. The source was Cu K_{α} containing both wavelengths $K_{\alpha1}$=1.54056 Å and $K_{\alpha2}$=1.5444 Å. Scans were done from 15˚to 80˚with a rate of 2˚/min using a variable slit. Divergent high limiting slit was 5 mm, divergent slit and scattering slit was 1 degree and receiving slit was 0.15 mm.

3.3.3 Texture Analysis

Texture analyses by Rietveld refinement were conducted using GSAS (General Structure Analysis System) using the non-linear least square approach during

refinements instead of other available Rietveld programs such as MAUD and RIETAN, since it has free usage and proved its efficiency in Materials Science field. Besides textured ceramics, Rietveld analysis of BaHF powder (~500 nm) was also conducted in order to analyze the degree of texture level compared to randomly distributed BaHF. XRD analyses of the specimens were performed as described above. Scans were done from 20˚ to 80˚ with a rate of 2˚/min using a variable slit. Before starting the GSAS refinement, CMPR (Configuration Management Process) program was used to plot diffraction patterns of both powder and textured ceramics in addition to converting the data to the GSAS format. The resulting data were implemented to GSAS and several cycles of refinement were performed for powder and bulk textured BaHF ceramics (separately applying March-Dollase and Spherical Harmonics functions) to determine final morphological characteristics of the materials. Before the refinement, following crystallographic information about BaHF having magnetoplumbite structure (Table 3.1) was introduced to the program.

Table 3.1 Crystallographic information about BaHF [111]

Space Group				$P6_3/mmc$					
Unit Cell				Hexagonal Cubic					
Lattice Parameters (A˚)				a=5.893 c=23.194					
Atom		Equipoint		x		y		z	
Ba	Ba	2c	2c	1/3	1/3	2/3	2/3	1/4	1/4
Fe(1)	Fe(1)	2a	2a	0	0	0	0	0	0
0.5Fe(2)	Fe(2)	4e	2b	0	0	0	0	0.257	1/4
Fe(3)	Fe(3)	4f	4f	2/3	2/3	1/3	1/3	0.027	0.027
Fe(4)	Fe(4)	4f	4f	2/3	2/3	1/3	1/3	0.190	0.190
Fe(5)	Fe(5)	12k	12k	0.169	0.169	2x	2x	0.108	0.108
O(1)	O(1)	4e	4e	0	0	0	0	0.150	0.150
O(2)	O(2)	4f	4f	1/3	1/3	2/3	2/3	0.055	0.053
O(3)	O(3)	6h	6h	0.816	0.817	2x	2x	1/4	1/4
O(4)	O(4)	12k	12k	0.845	0.848	2x	2x	0.052	0.052
O(5)	O(5)	12k	12k	0.497	0.498	2x	2x	0.150	0.150

Second method for the texture analysis was the pole figure measurement. In that method, XRD device of General Electric - Seifert XRD 3003 PTS was used. Since the platelets were supposed to align along (00l) plane, pole figure measurements were obtained with 5˚ rotation steps on (006) plane between the 2θ values of 22.93750 and 23.06150 with the α and β rotation angles of 0-80˚ and 0-360˚, respectively.

Last method used for the evaluation of texture was EBSD. For that purpose, SEM (Nova NanoSEM) equipped with electron backscatter diffraction pattern attachment was used. The textured sample was prepared by polishing with diamond paste starting from 9 μm and going down to 6, 3, 1, 0.25 μm followed by lapping for 2 hours with colloidal silica having particle size 0.05 μm. EBSD was conducted with a 20 keV beam having a spot size of 4.5 to obtain denser Kikuchi paths.

CHAPTER 4

EXPERIMENTAL DATA AND RESULTS

4.1. XRD and SEM Analyses of Platelets Synthesized by Molten Salt Synthesis

ICP-MS results showed that the solubility of Fe_2O_3 is almost zero in both NaCl and KCl fluxes, while $BaCO_3$ has extensive solubility in both of them (see Table 4.1 (a) and (b)). XRD results confirmed these results, since they demonstrate the presence of considerable amount of hematite yet no $BaCO_3$ or BaO in the filtrated solid residues as shown in Figure 4.1.

Table 4.1 Inductively coupled plasma – mass spectroscopy results of samples sintered at 900 ˚C for 10, 15, 20 minutes in (a) KCl flux.

ELEMENT	10K-900	15K-900	20K-900
Ba (mg/l)	128±1.0	118±1	115±1
K (g/l)	53±1	52±1	55±1

Table 4.1 Inductively coupled plasma – mass spectroscopy results of samples sintered at 900 ˚C for 10, 15, 20 minutes in (b) NaCl flux. (cont'd)

ELEMENT	10N-900	15N-900	20N-900
Ba (mg/l)	117.9±0.8	123.5±0.7	110.3±0.7
Na (g/l)	39.9±0.6	36±1	32.3±0.6

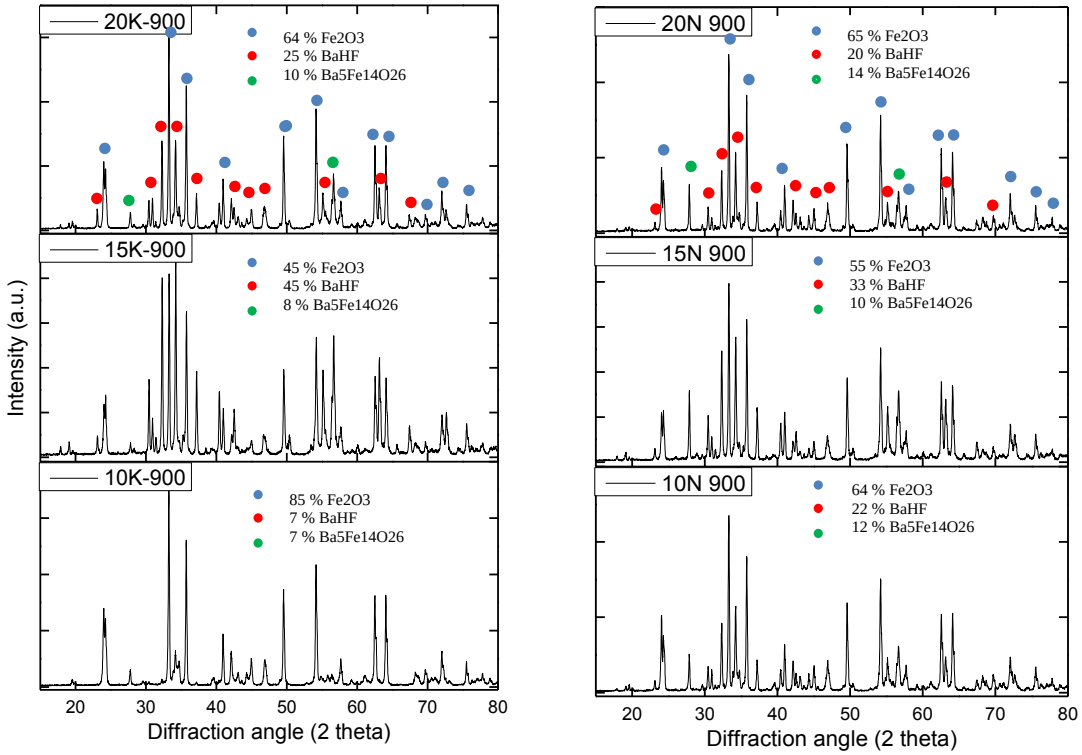

Figure 4.1 XRD results of samples sintered at 900 ˚C for 10, 15, 20 minutes in KCl and NaCl fluxes. (JCPDS-ICDD card no. 43-0002, 33-0664, 28-0144 for BaHF, Fe_2O_3 and $Ba_5Fe_{14}O_{26}$, respectively).

According to the phase diagram shown in Figure 4.2 and the XRD results in Figure above, the first forming phase seems to be $Ba_5Fe_{14}O_{26}$. However, other phases on the phase diagram cannot be seen up to the formation of BaHF.

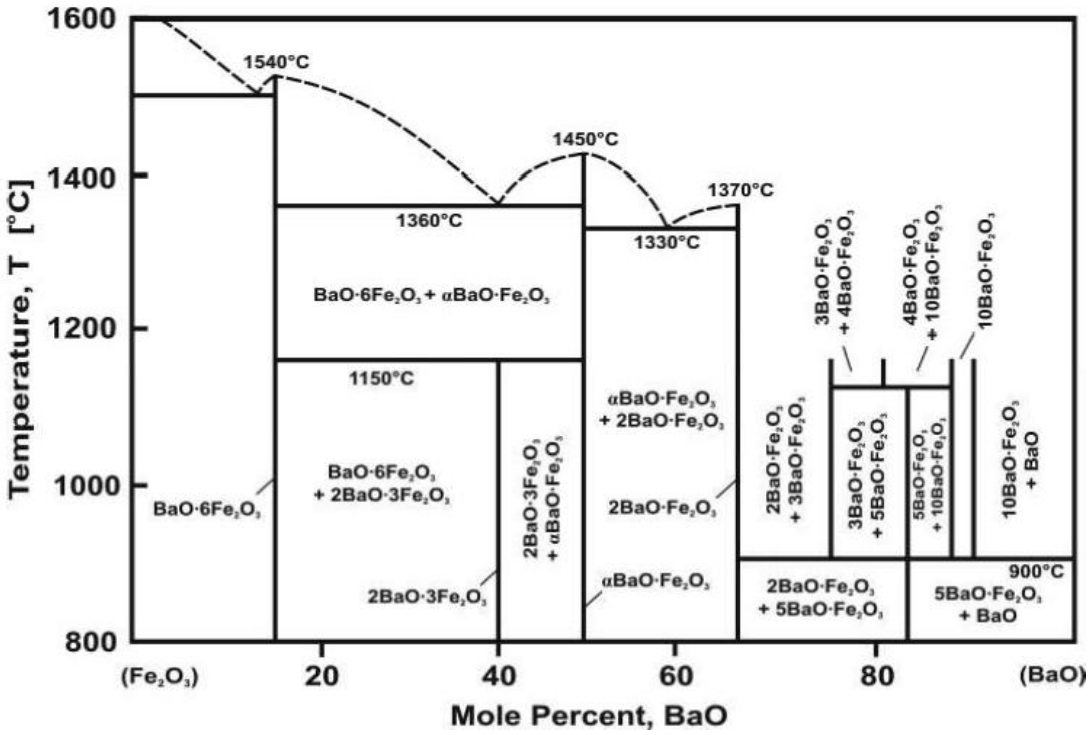

Figure 4.2 Fe_2O_3 – BaO equilibrium phase diagram [112]

When barium content is low, $Ba_5Fe_{14}O_{26}$ phase disappears in long calcination durations; however, if the barium content increases, this phase will be stabilized and increases in amount in both NaCl and KCl fluxes as shown in Figure 4.3.

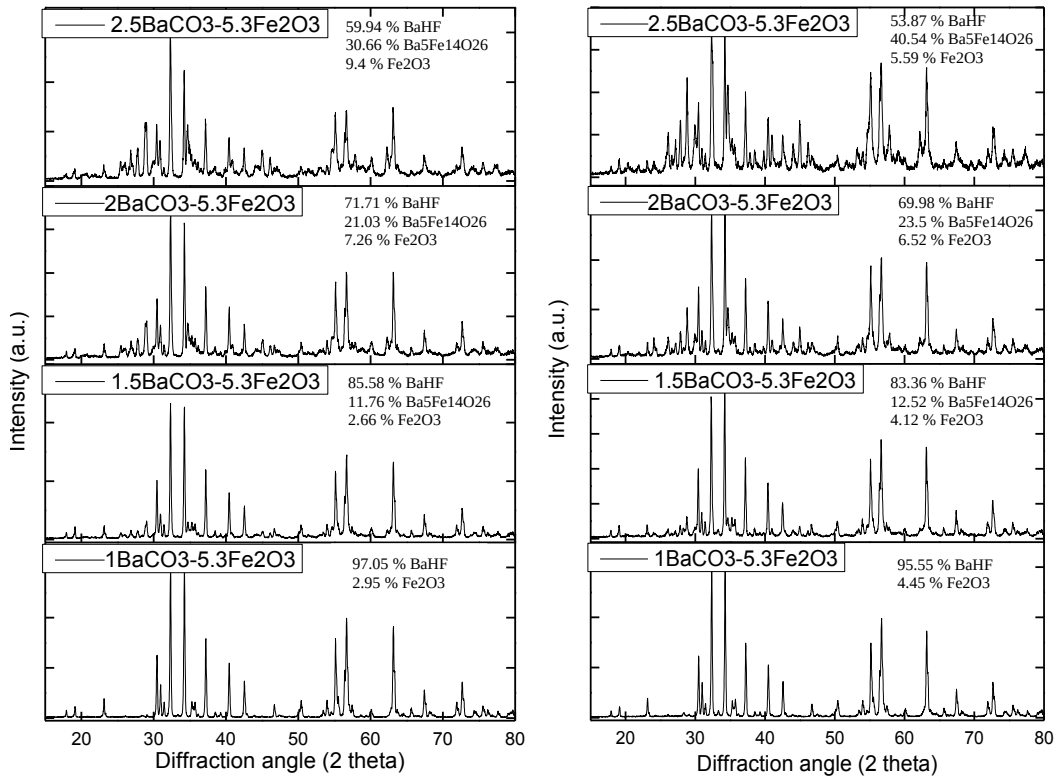

Figure 4.3 XRD results of samples sintered at 900 ˚C for 1 hour (a) in NaCl and NaCl (b) in KCl fluxes. (JCPDS-ICDD card no. 43-0002, 33-0664, 28-0144 for BaHF, Fe_2O_3 and $Ba_5Fe_{14}O_{26}$, respectively).

Morphology of these phase mixtures as a result of varying $BaCO_3$ to Fe_2O_3 ratios can be seen as in Figure 4.4. With the increase in the $BaCO_3$ to Fe_2O_3 ratio, shapes of the phases show a variation. For $BaCO_3$ to Fe_2O_3 ratio of 1.5:5.3, microstructure is composed of small particles together with large rectangular prismatic platelets having high aspect ratio. However, with the further increase in this ratio, these powders and platelets start to show agglomeration.

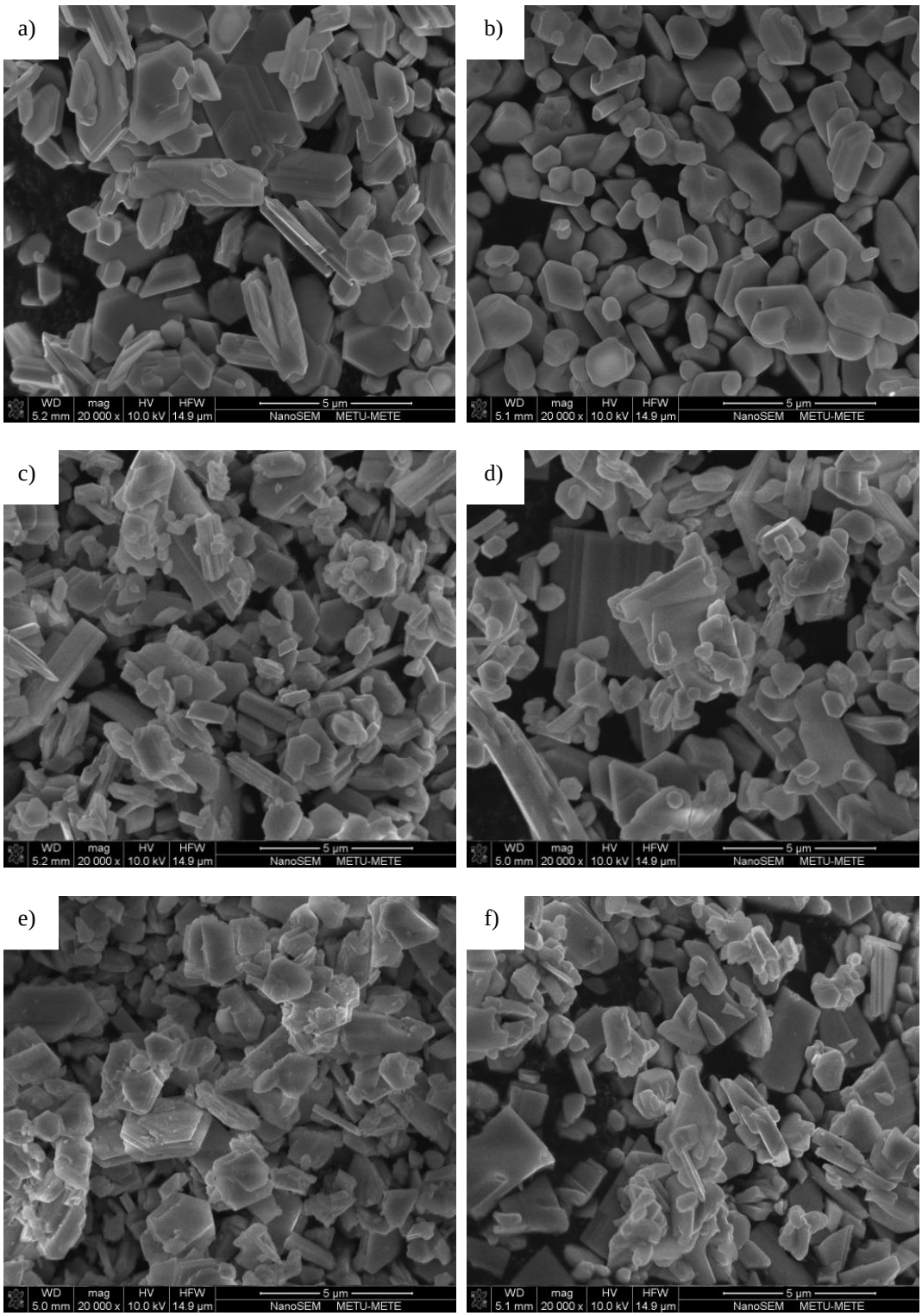

Figure 4.4 SEM image of barium hexaferrite synthesized with $BaCO_3$ to Fe_2O_3 ratio of 1:5.3 (a) in KCl flux, (b) in NaCl flux; $BaCO_3$ to Fe_2O_3 ratio of 1.5:5.3 (c) in KCl flux, (d) in NaCl flux; $BaCO_3$ to Fe_2O_3 ratio of 2:5.3 (e) in KCl flux, (f) in NaCl flux.

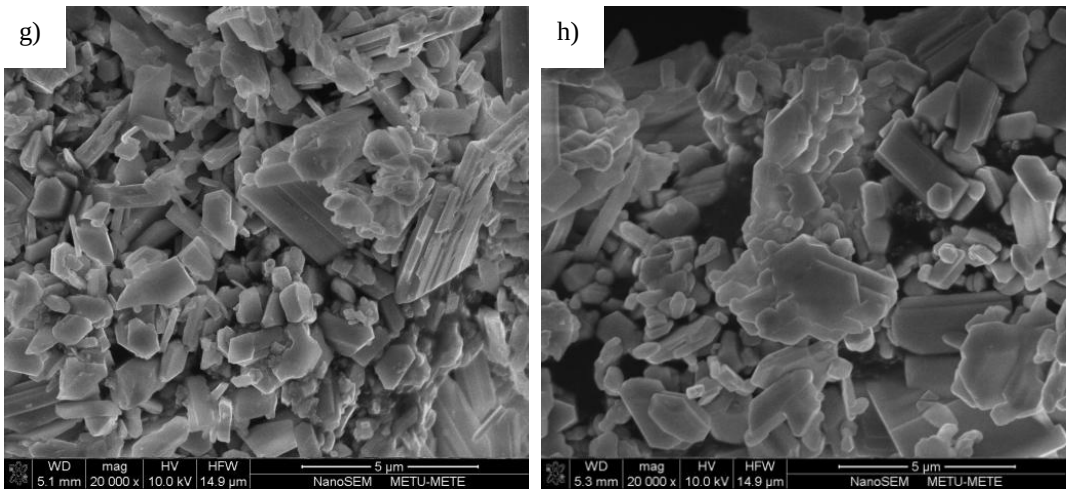

Figure 4.4 SEM image of barium hexaferrite synthesized with $BaCO_3$ to Fe_2O_3 ratio of 2.5:5.3 (g) in KCl flux, (h) in NaCl flux. (cont'd)

As the platelets were synthesized in order to be used in the fabrication of textured bulk BaHF ceramics by TGG, the largest ones with the highest aspect ratio are preferable. Figure 4.5, 4.6, 4.7 & 4.8 show the platelet size distribution as a function of flux composition for varying calcination durations and temperatures. For all the conditions, platelet size in KCl flux is the smallest. With the increase in the NaCl content platelet size increases; however, it starts to decrease again towards the equimolar flux composition. Above that NaCl concentration, platelet size first increases followed by a steep decrease towards pure NaCl flux. Here it should be noted that platelet size in NaCl flux is larger than that of in KCl for all the calcination temperatures and durations applied. When compared to other temperatures, platelet size at 900 ˚C is the largest for most of the compositions and durations, which is especially valid for 2 h.

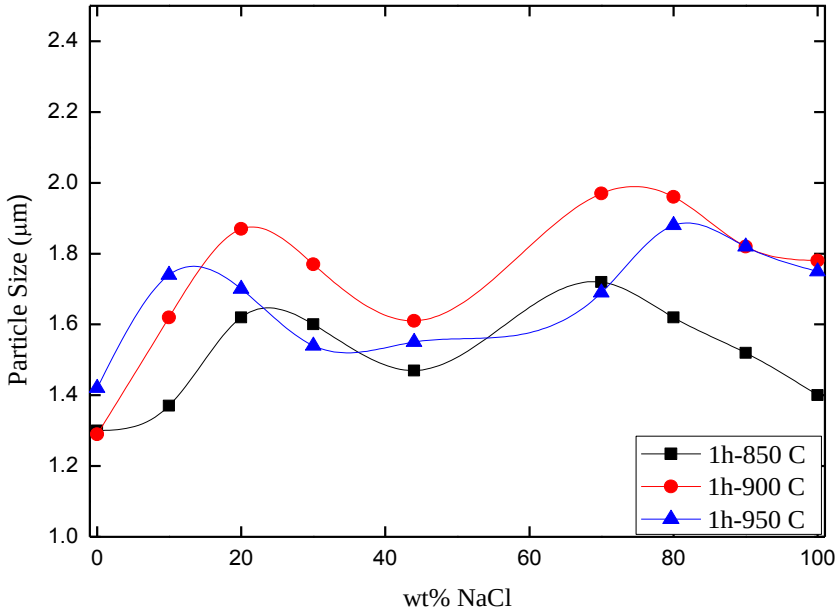

Figure 4.5 Particle size vs. composition graph at 850, 900 and 950 ˚C for 1 h.

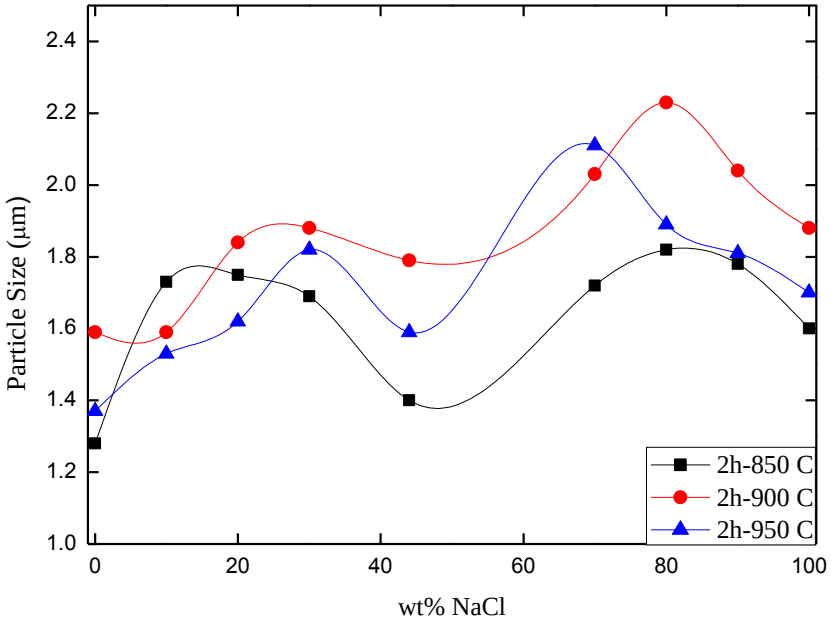

Figure 4.6 Particle size vs. composition graph at 850, 900 and 950 ˚C for 2 h.

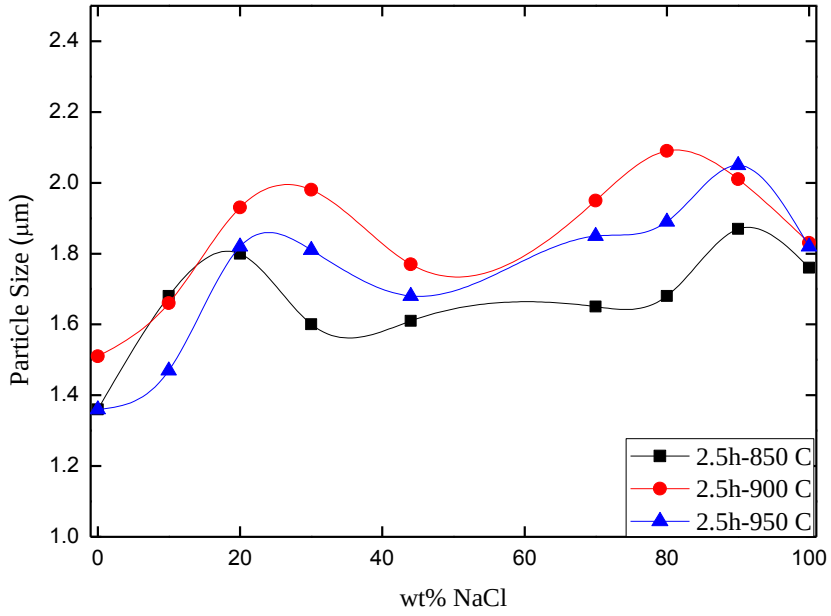

Figure 4.7 Particle size vs. composition graph at 850, 900 and 950 ˚C for 2.5 h.

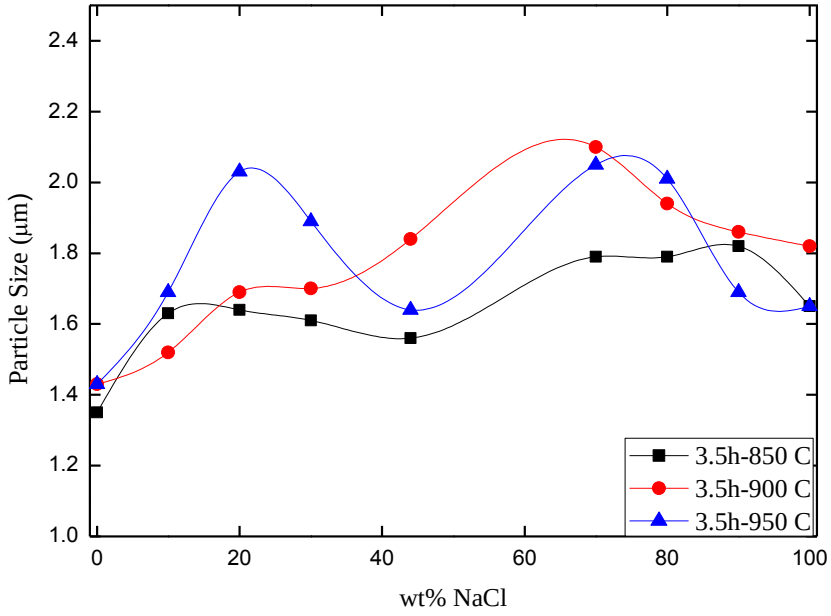

Figure 4.8 Particle size vs. composition graph at 850, 900 and 950 ˚C for 3.5 h.

From the SEM images in Figure 4.9 (a), (b), (c), (d), (e), (f), (g), (h), (i), Figure 4.10 (a), (b), (c), (d), (e), (f), (g), (h), (i), Figure 4.11 (a), (b), (c), (d), (e), (f), (g), (h), (i) and Figure 4.12 (a), (b), (c), (d), (e), (f), (g), (h), (i) both morphologies and sizes can be seen at 850 ˚C for calcination times of 1h, 2h, 2.5h and 3.5h, respectively. Figure 4.13 (a), (b), (c), (d), (e), (f), (g), (h), (i), Figure 4.14 (a), (b), (c), (d), (e), (f), (g), (h), (i), Figure 4.15 (a), (b), (c), (d), (e), (f), (g), (h), (i) and Figure 4.16 (a), (b), (c), (d), (e), (f), (g), (h), (i) show the microstructures of powders calcined at 900 ˚C for calcination times of 1h, 2h, 2.5h and 3.5h, respectively. Also, Figure 4.17 (a), (b), (c), (d), (e), (f), (g), (h), (i), Figure 4.18 (a), (b), (c), (d), (e), (f), (g), (h), (i), Figure 4.19 (a), (b), (c), (d), (e), (f), (g), (h), (i) and Figure 4.20 (a), (b), (c), (d), (e), (f), (g), (h), (i) show the microstructures of powders calcined at 950 ˚C for calcination times of 1h, 2h, 2.5h and 3.5h, respectively. From the SEM images, parameters of the largest particle size with highest aspect ratio can be determined.

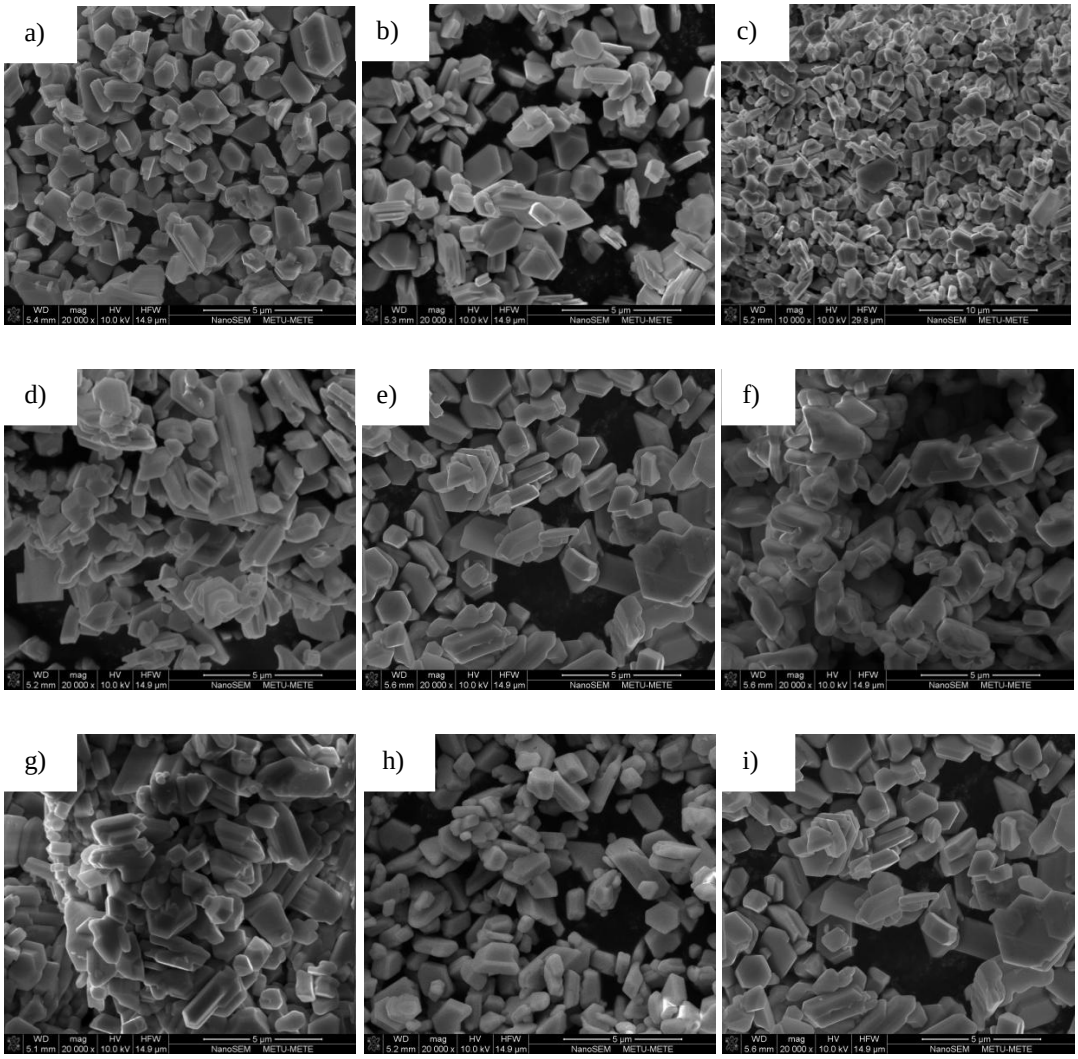

Figure 4.9 SEM images of BaHF platelets sintered in (a) pure KCl, (b) 90 wt% KCl – 10 wt% NaCl, (c) 80 wt% KCl – 20 wt% NaCl, (d) 70 wt% KCl – 30 wt% NaCl, (e) 44 wt% NaCl – 56 wt% KCl (1:1 mol), (f) 70 wt% NaCl – 30 wt% KCl, (g) 80 wt% NaCl – 20 wt% KCl, (h) 90 wt% NaCl - 10 wt% KCl, (i) pure NaCl at 850 ˚C for 1 h.

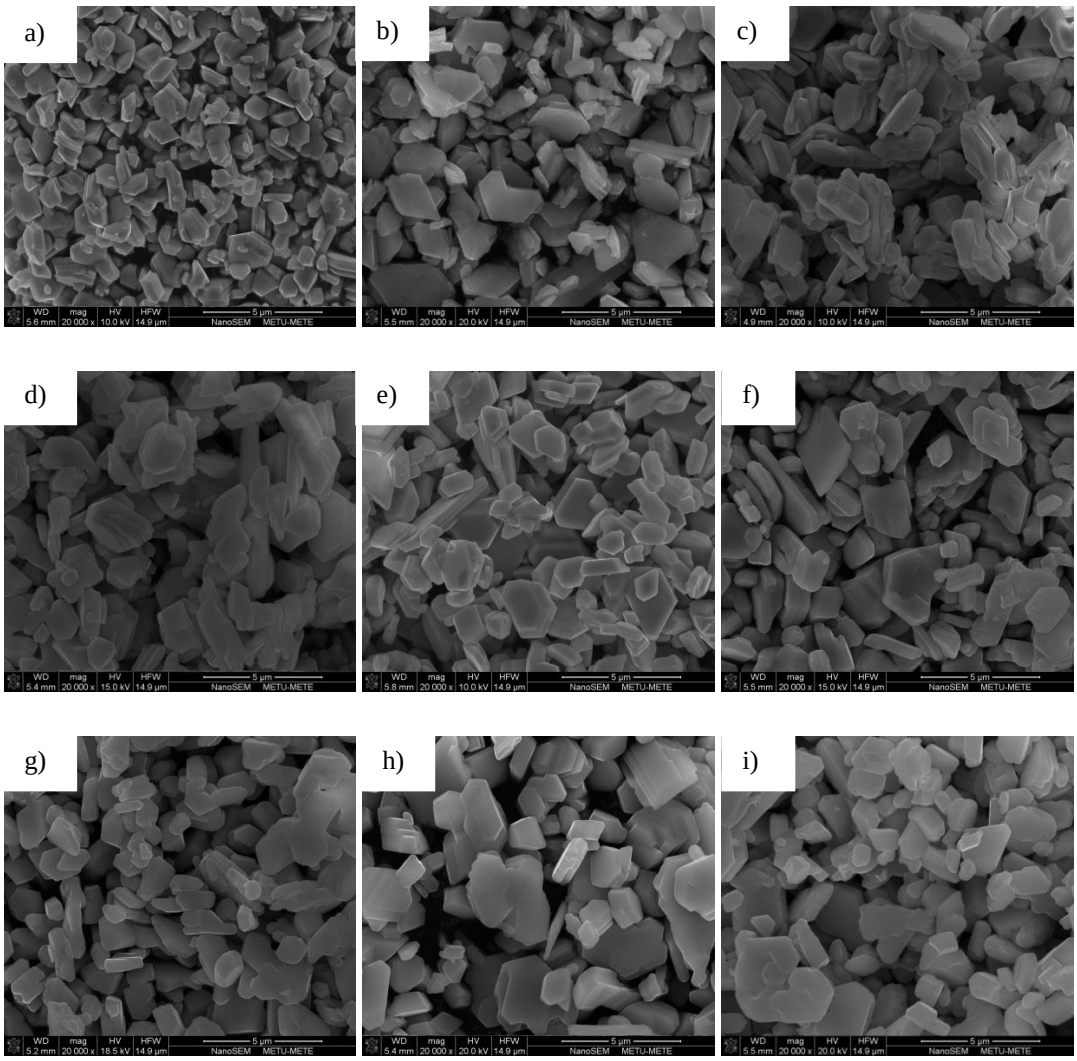

Figure 4.10 SEM images of BaHF platelets sintered in (a) pure KCl, (b) 90 wt% KCl – 10 wt% NaCl, (c) 80 wt% KCl – 20 wt% NaCl, (d) 70 wt% KCl – 30 wt% NaCl, (e) 44 wt% NaCl – 56 wt% KCl (1:1 mol), (f) 70 wt% NaCl – 30 wt% KCl, (g) 80 wt% NaCl – 20 wt% KCl, (h) 90 wt% NaCl - 10 wt% KCl, (i) pure NaCl at 850 ˚C for 2 h.

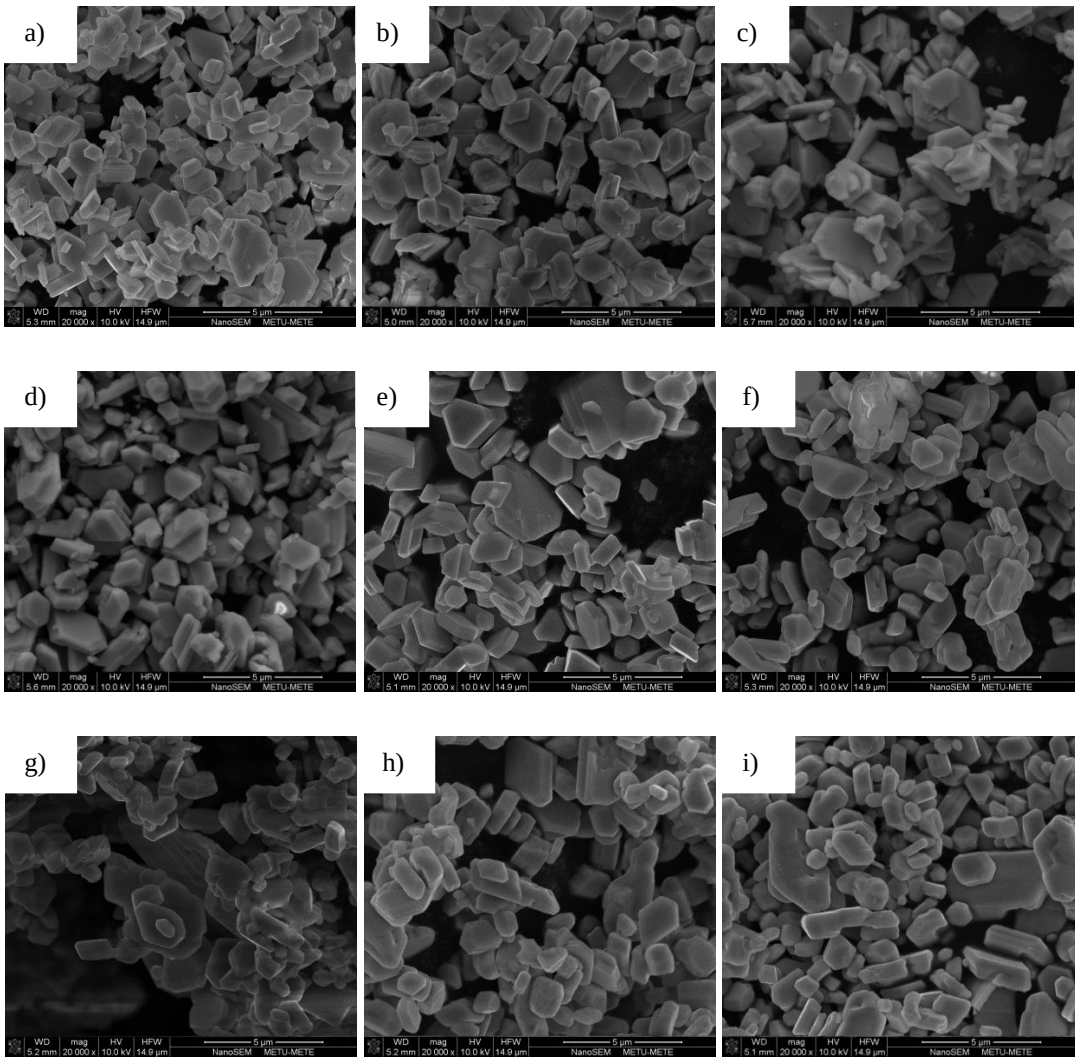

Figure 4.11 SEM images of BaHF platelets sintered in (a) pure KCl, (b) 90 wt% KCl – 10 wt% NaCl, (c) 80 wt% KCl – 20 wt% NaCl, (d) 70 wt% KCl – 30 wt% NaCl, (e) 44 wt% NaCl – 56 wt% KCl (1:1 mol), (f) 70 wt% NaCl – 30 wt% KCl, (g) 80 wt% NaCl – 20 wt% KCl, (h) 90 wt% NaCl - 10 wt% KCl,(i) pure NaCl at 850 ˚C for 2.5 h.

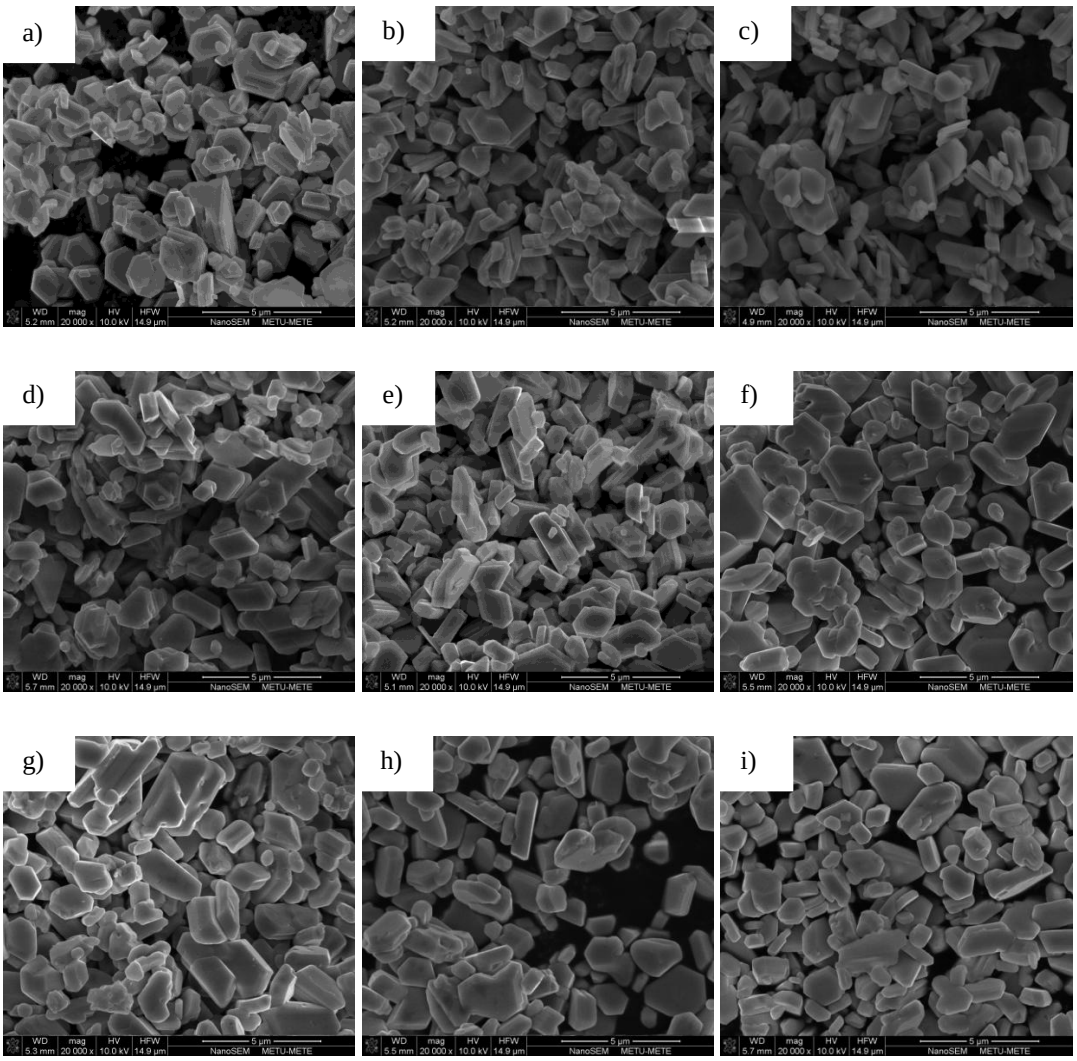

Figure 4.12 SEM images of BaHF platelets sintered in (a) pure KCl, (b) 90 wt% KCl – 10 wt% NaCl, (c) 80 wt% KCl – 20 wt% NaCl, (d) 70 wt% KCl – 30 wt% NaCl, (e) 44 wt% NaCl – 56 wt% KCl (1:1 mol), (f) 70 wt% NaCl – 30 wt% KCl, (g) 80 wt% NaCl – 20 wt% KCl, (h) 90 wt% NaCl - 10 wt% KCl, (i) pure NaCl at 850 ˚C for 3.5 h.

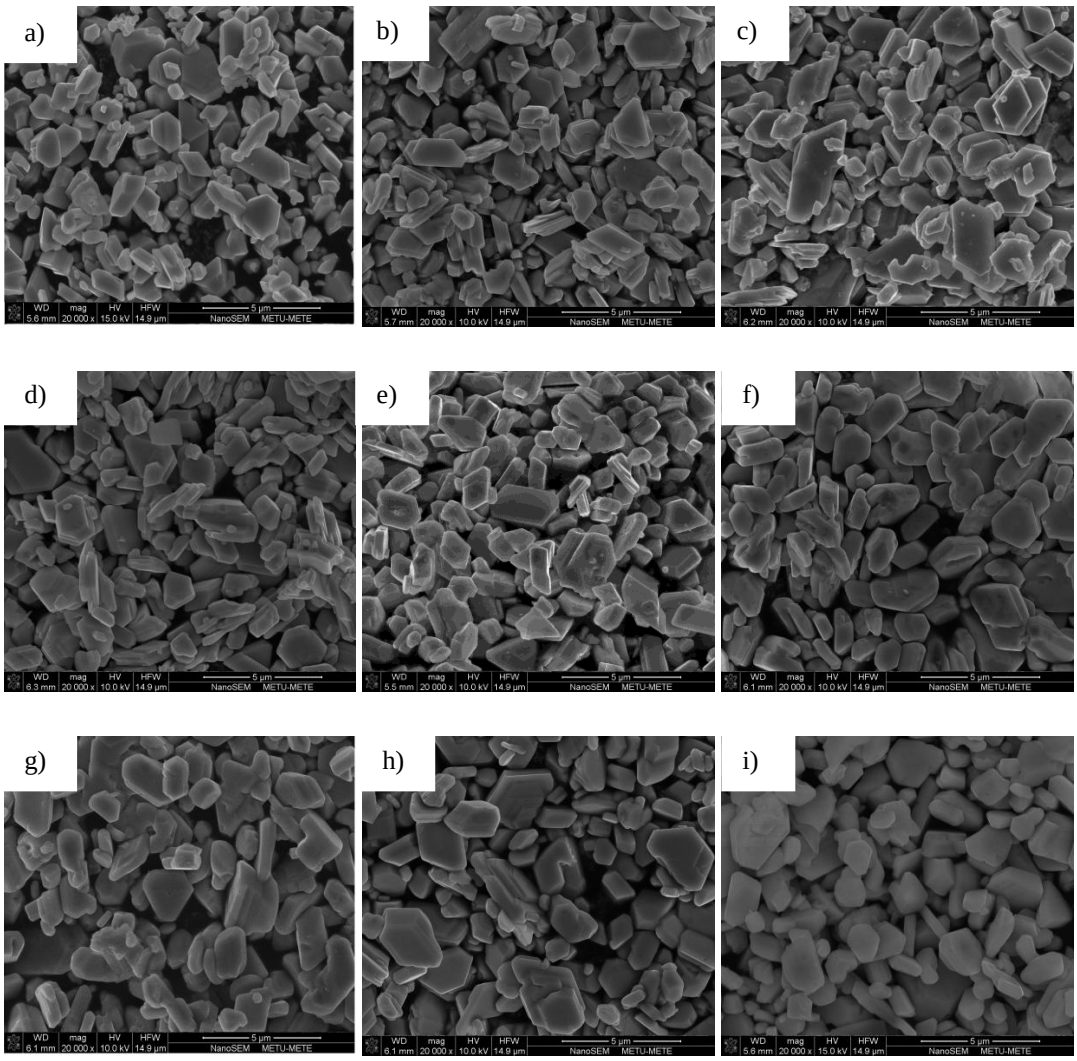

Figure 4.13 SEM images of BaHF platelets sintered in (a) pure KCl, (b) 90 wt% KCl – 10 wt% NaCl, (c) 80 wt% KCl – 20 wt% NaCl, (d) 70 wt% KCl – 30 wt% NaCl, (e) 44 wt% NaCl – 56 wt% KCl (1:1 mol), (f) 70 wt% NaCl – 30 wt% KCl, (g) 80 wt% NaCl – 20 wt% KCl, (h) 90 wt% NaCl - 10 wt% KCl, (i) pure NaCl at 900 ˚C for 1 h.

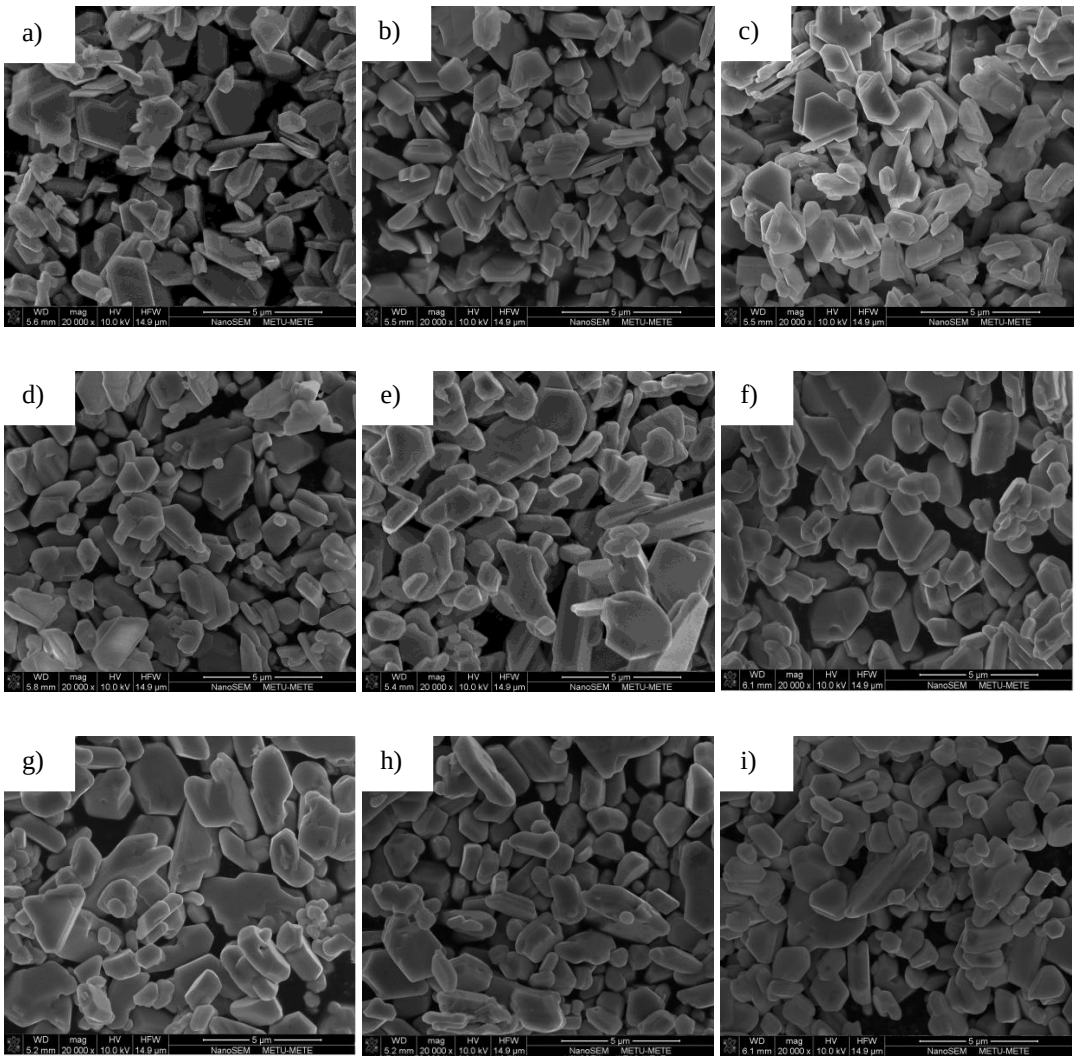

Figure 4.14 SEM images of BaHF platelets sintered in (a) pure KCl, (b) 90 wt% KCl – 10 wt% NaCl, (c) 80 wt% KCl – 20 wt% NaCl, (d) 70 wt% KCl – 30 wt% NaCl, (e) 44 wt% NaCl – 56 wt% KCl (1:1 mol), (f) 70 wt% NaCl – 30 wt% KCl, (g) 80 wt% NaCl – 20 wt% KCl, (h) 90 wt% NaCl - 10 wt% KCl,(i) pure NaCl at 900 ˚C for 2 h.

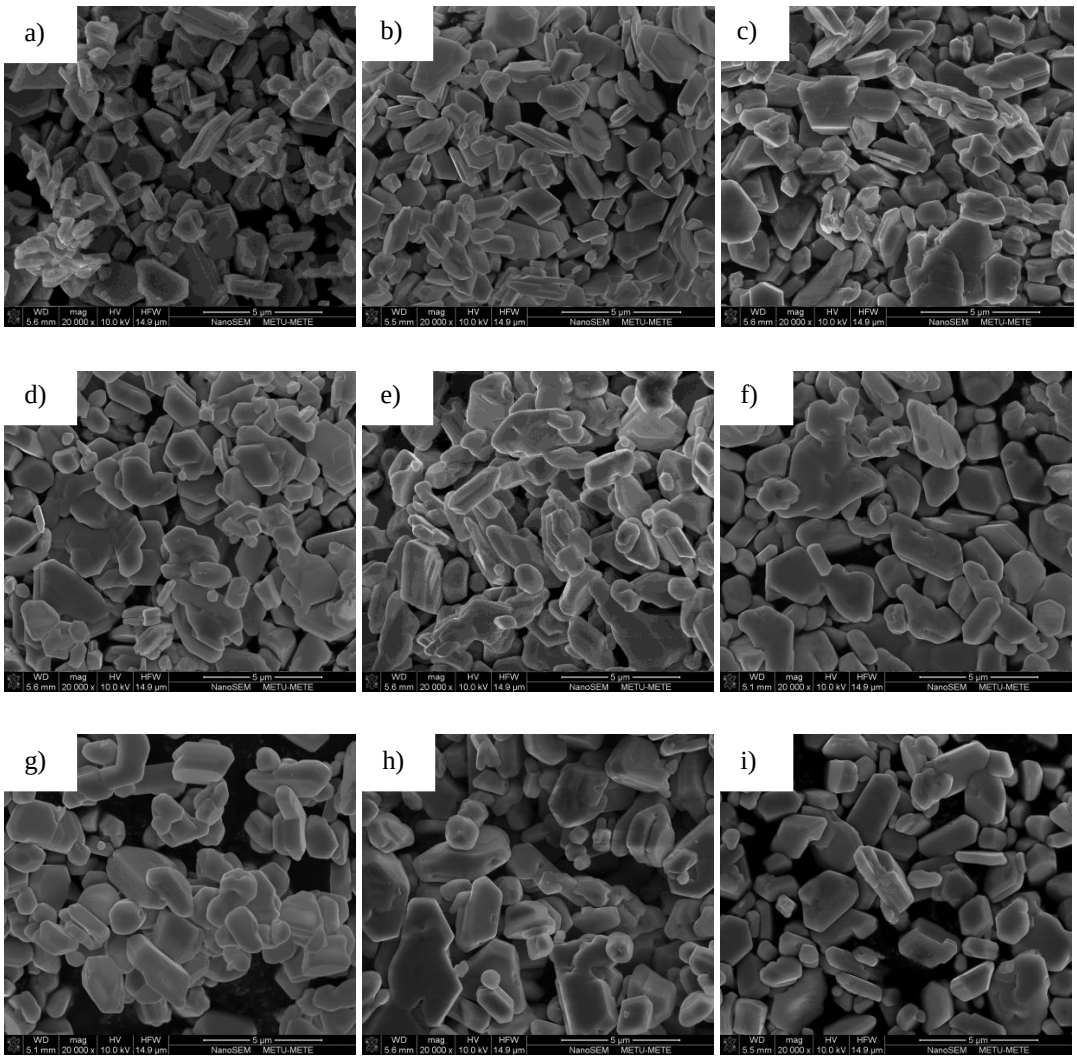

Figure 4.15 SEM images of BaHF platelets sintered in (a) pure KCl, (b) 90 wt% KCl – 10 wt% NaCl, (c) 80 wt% KCl – 20 wt% NaCl, (d) 70 wt% KCl – 30 wt% NaCl, (e) 44 wt% NaCl – 56 wt% KCl (1:1 mol), (f) 70 wt% NaCl – 30 wt% KCl, (g) 80 wt% NaCl – 20 wt% KCl, (h) 90 wt% NaCl - 10 wt% KCl, (i) pure NaCl at 900 ˚C for 2.5 h.

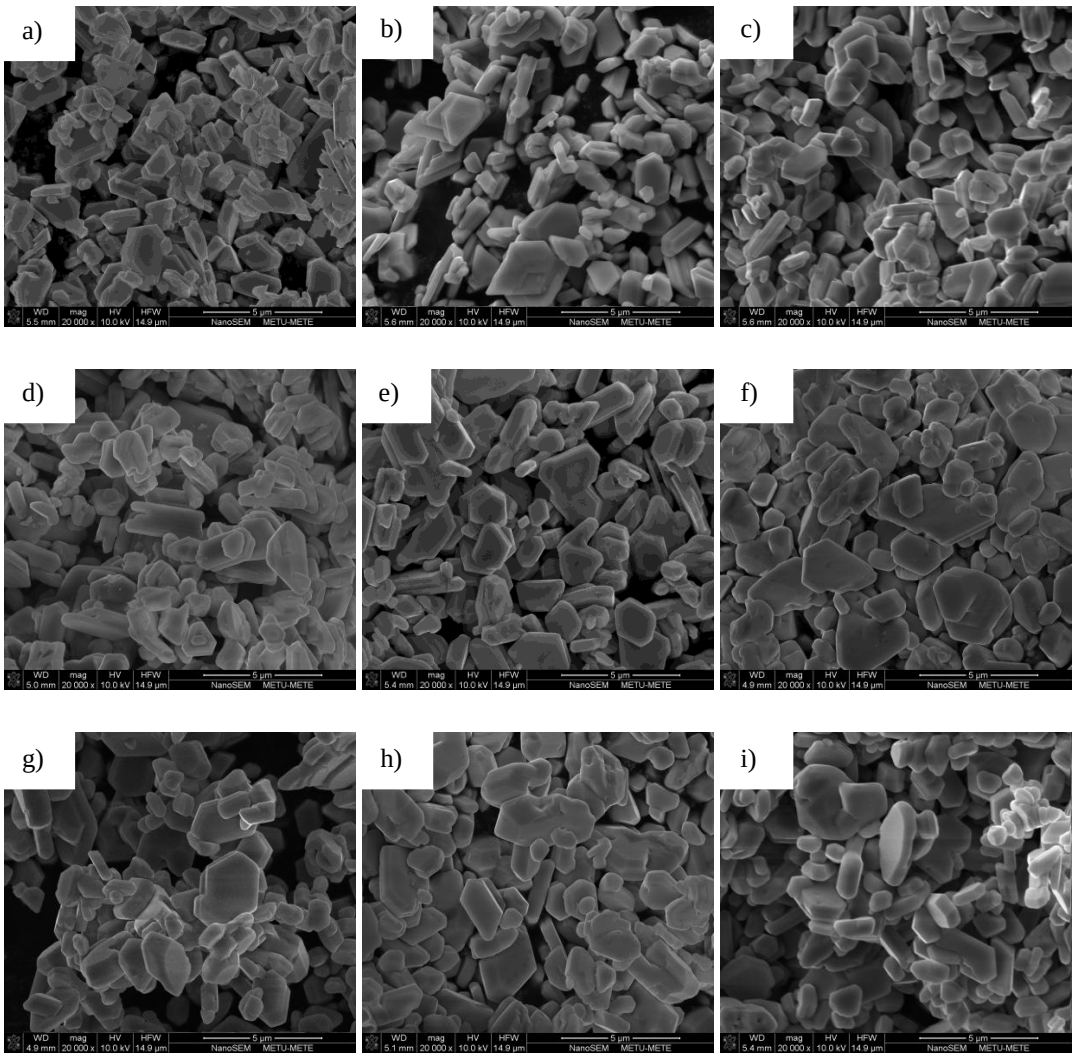

Figure 4.16 SEM images of BaHF platelets sintered in (a) pure KCl, (b) 90 wt% KCl – 10 wt% NaCl, (c) 80 wt% KCl – 20 wt% NaCl, (d) 70 wt% KCl – 30 wt% NaCl, (e) 44 wt% NaCl – 56 wt% KCl (1:1 mol), (f) 70 wt% NaCl – 30 wt% KCl, (g) 80 wt% NaCl – 20 wt% KCl, (h) 90 wt% NaCl - 10 wt% KCl, (i) pure NaCl at 900 ˚C for 3.5 h.

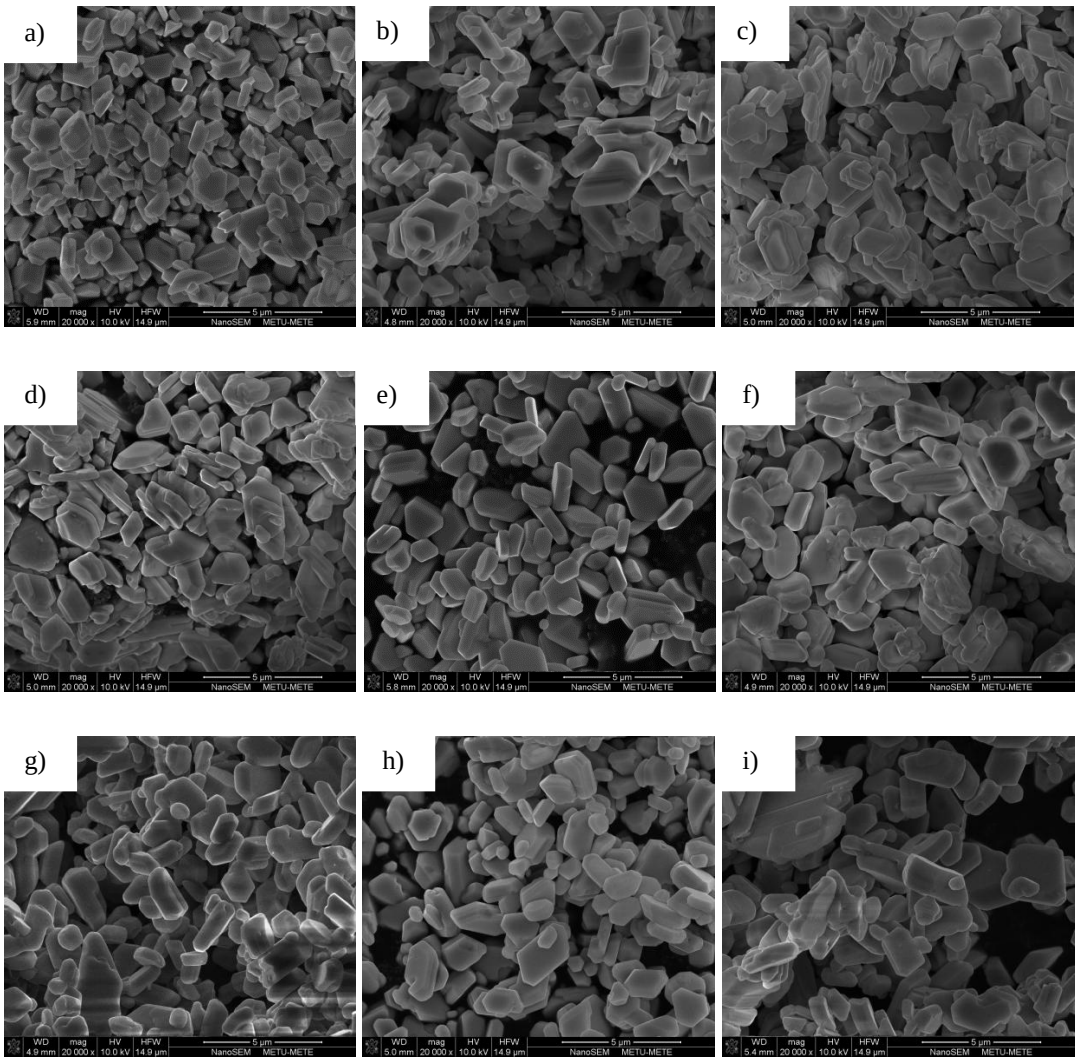

Figure 4.17 SEM images of BaHF platelets sintered in (a) pure KCl, (b) 90 wt% KCl – 10 wt% NaCl, (c) 80 wt% KCl – 20 wt% NaCl, (d) 70 wt% KCl – 30 wt% NaCl, (e) 44 wt% NaCl – 56 wt% KCl (1:1 mol), (f) 70 wt% NaCl – 30 wt% KCl, (g) 80 wt% NaCl – 20 wt% KCl, (h) 90 wt% NaCl - 10 wt% KCl, (i) pure NaCl at 950 ˚C for 1 h.

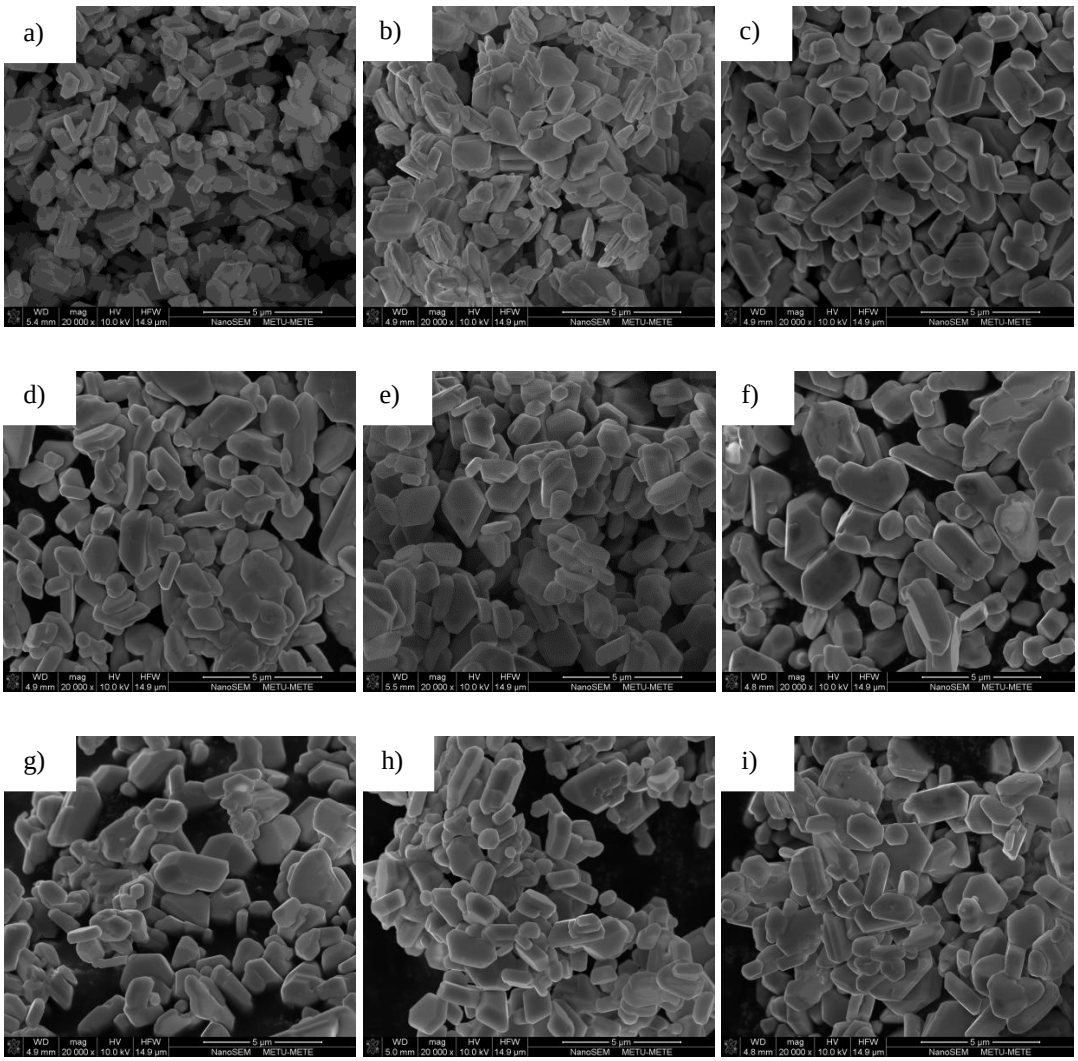

Figure 4.18 SEM images of BaHF platelets sintered in (a) pure KCl, (b) 90 wt% KCl – 10 wt% NaCl, (c) 80 wt% KCl – 20 wt% NaCl, (d) 70 wt% KCl – 30 wt% NaCl, (e) 44 wt% NaCl – 56 wt% KCl (1:1 mol), (f) 70 wt% NaCl – 30 wt% KCl, (g) 80 wt% NaCl – 20 wt% KCl, (h) 90 wt% NaCl - 10 wt% KCl, i) pure NaCl at 950 ˚C for 2 h.

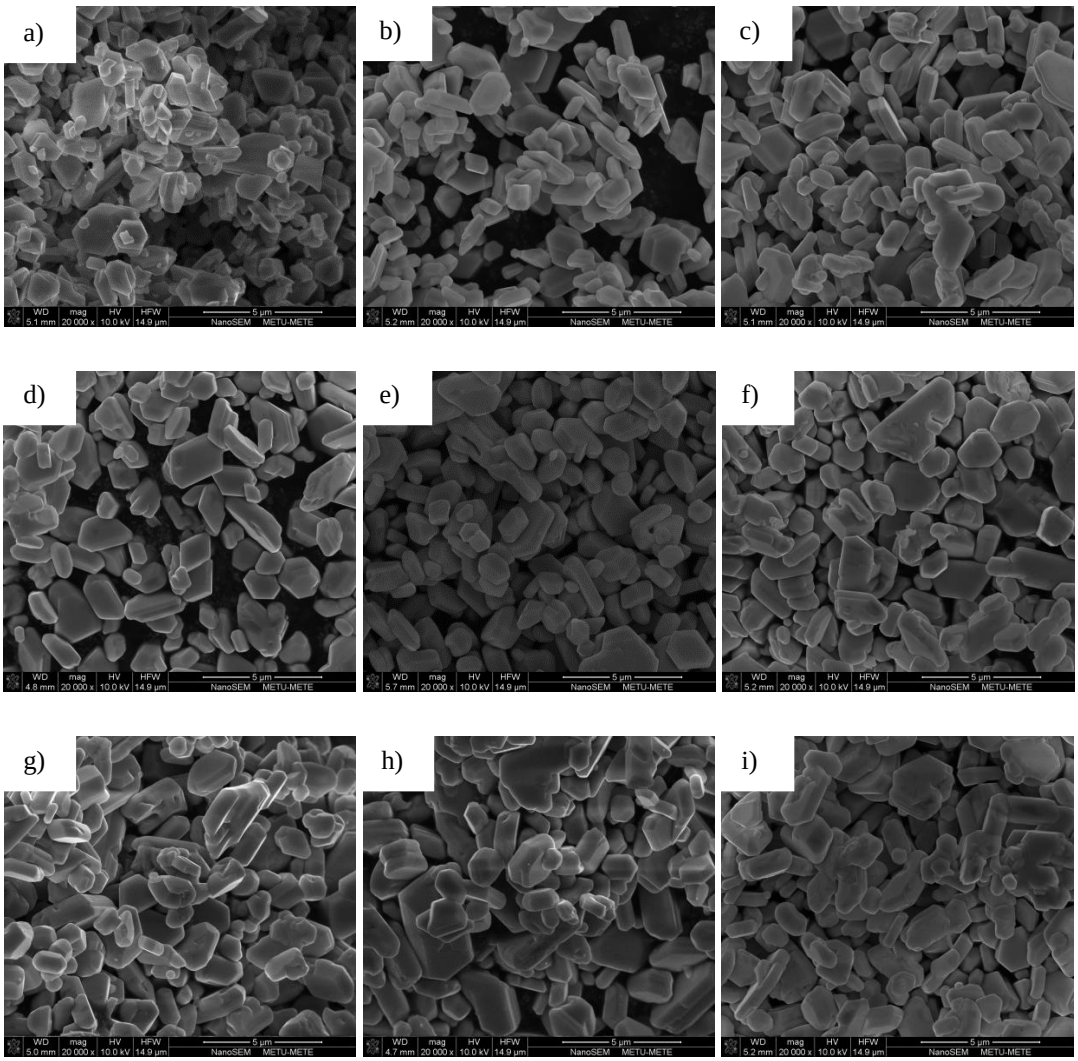

Figure 4.19 SEM images of BaHF platelets sintered in (a) pure KCl, (b) 90 wt% KCl – 10 wt% NaCl, (c) 80 wt% KCl – 20 wt% NaCl, (d) 70 wt% KCl – 30 wt% NaCl, (e) 44 wt% NaCl – 56 wt% KCl (1:1 mol), (f) 70 wt% NaCl – 30 wt% KCl, (g) 80 wt% NaCl – 20 wt% KCl, (h) 90 wt% NaCl - 10 wt% KCl, (i) pure NaCl at 950 ˚C for 2.5 h.

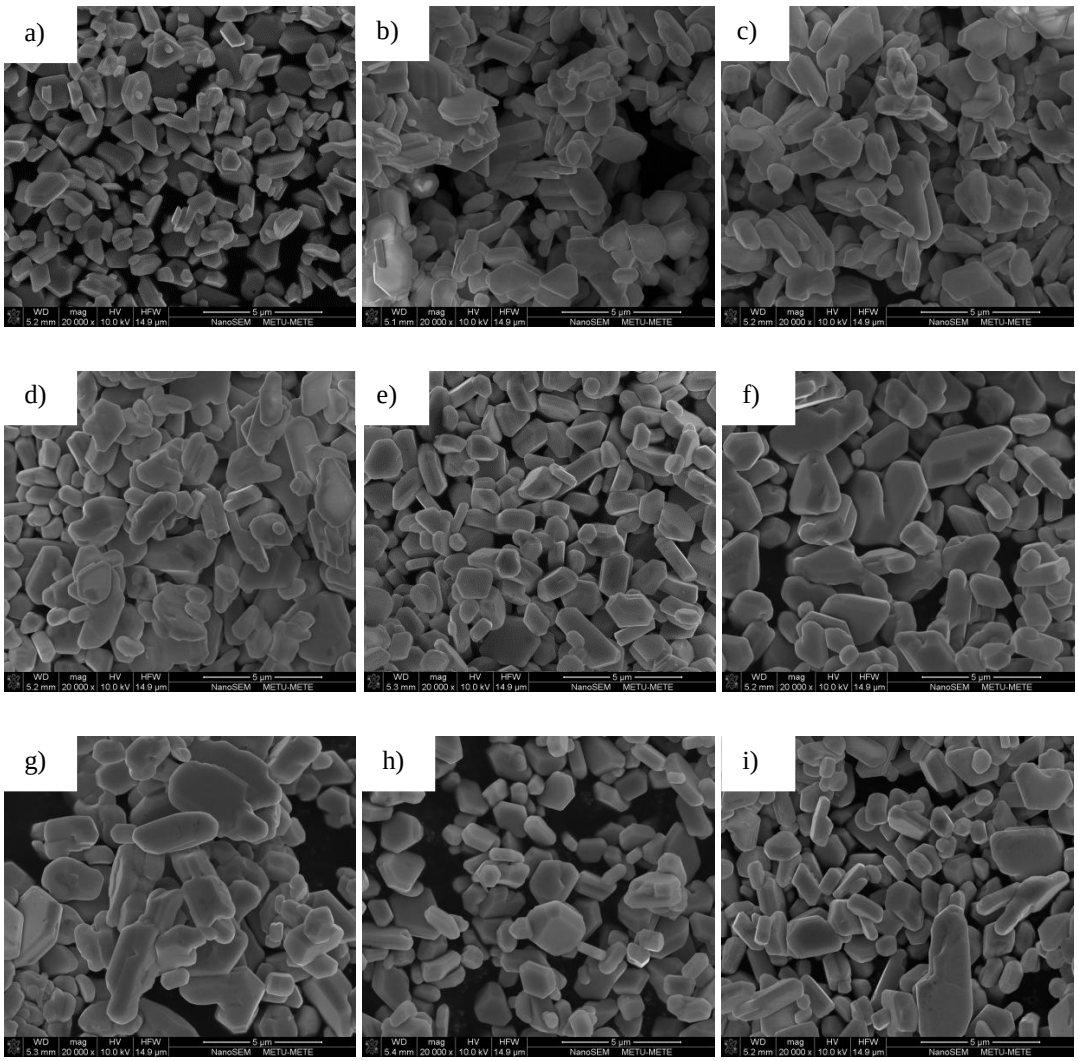

Figure 4.20 SEM images of BaHF platelets sintered in (a) pure KCl, (b) 90 wt% KCl – 10 wt% NaCl, (c) 80 wt% KCl – 20 wt% NaCl, (d) 70 wt% KCl – 30 wt% NaCl, (e) 44 wt% NaCl – 56 wt% KCl (1:1 mol), (f) 70 wt% NaCl – 30 wt% KCl, (g) 80 wt% NaCl – 20 wt% KCl, (h) 90 wt% NaCl - 10 wt% KCl, (i) pure NaCl at 950 ˚C for 3.5 h.

Platelets synthesized in KCl flux, revealed sharper edges compared to those in NaCl. This morphology difference became more obvious at higher calcination temperature and durations. Moreover, as the time and temperature increases, aspect ratio of the platelets became smaller. However, even at lowest temperatures and shortest durations aspect ratios could not exceed ~3-4 (Figure 4.9 - 4.20).

In order to investigate the morphology variation it is necessary to understand the diffusion mechanisms and relative activation energies of the operating mechanisms in both fluxes. This is because different morphologies may have resulted from different particle growth mechanism at different calcination temperatures [13]. Activation energy for particle growth can be calculated from the plot of lnD versus 1/T, which is derived from an Arrhenius type of relationship (Equation 4.1) [55, 56];

$$2\ln D = \ln k + \ln t - E_{act}/RT \qquad (4.1)$$

where D is the average particle size at time t, k is the rate constant, $E_{act.}$ is the activation energy for particle growth, R is the gas constant and T is the calcination temperature. In order to investigate the growth mechanisms of platelets in NaCl and KCl fluxes, their activation energies for 1, 2, 2.5 and 3.5 h were calculated from the plot of lnD versus 1/T graph given in Figure 4.21, Figure 4.22, Figure 4.23 and Figure 4.24.

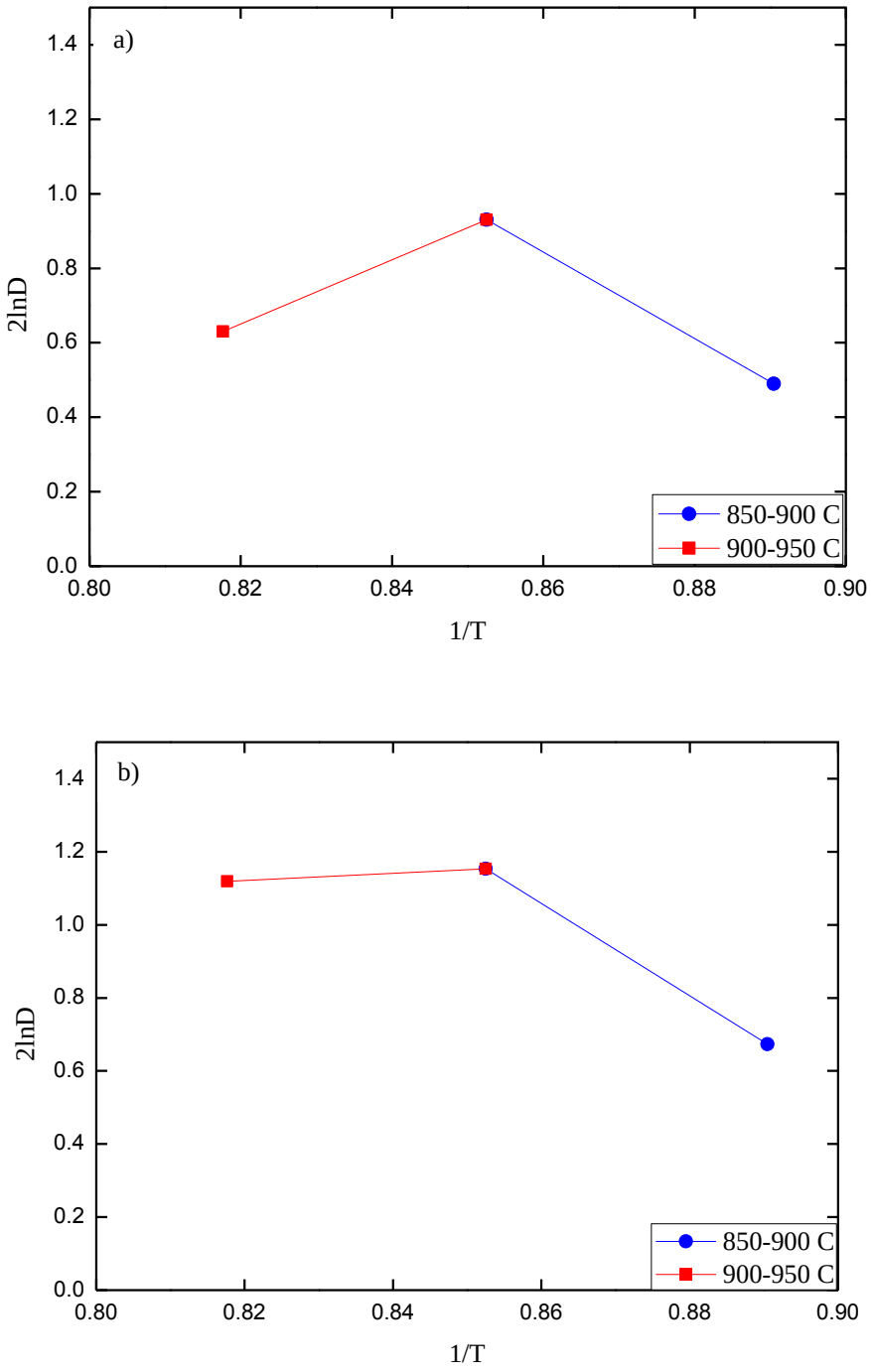

Figure 4.21 Plot of 2 lnD (average particle size) vs. 1/T for 1 h in (a) KCl flux, (b) NaCl flux. (The lines are for visual help).

In Figure 4.21 (a), apparent activation energy for the formation of BaHF in molten KCl is negative between 850 and 900 °C, whereas it is seen to be 45.32 kJ/mol between 900 and 950 °C for the calcination duration of 1 h. Negative activation energy indicates the dominance of another mechanism for the mass transport instead of diffusion. In the case of NaCl flux, apparent activation energy is seen to be 105.2 kJ/mol between 850 and 900 °C, which turns to be negative between 900 and 950 °C (Figure 4.21 (b)). Particle size decrease in both of the cases has been attributed to the desorption from the corners.

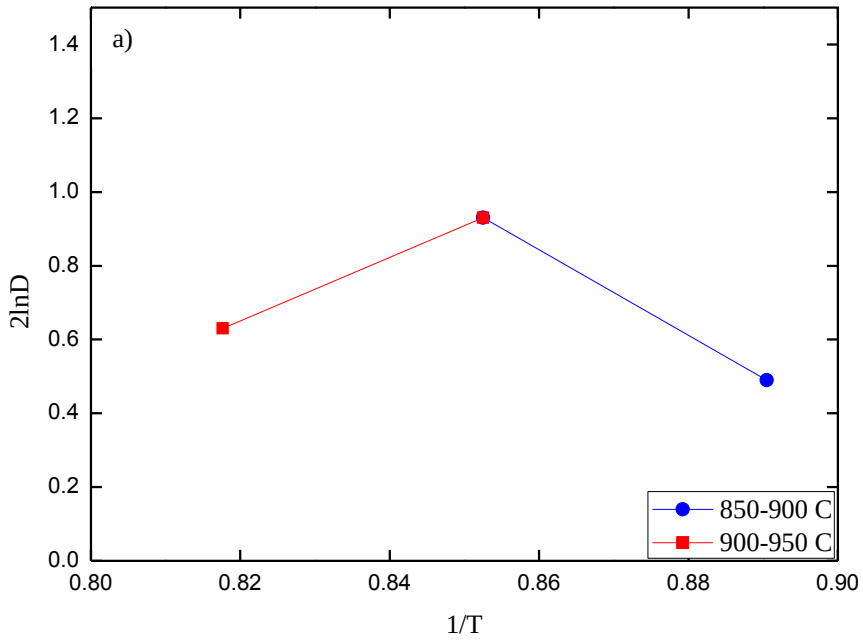

Figure 4.22 Plot of 2 lnD (average particle size) vs. 1/T for 2 h in (a) KCl flux. (The lines are for visual help).

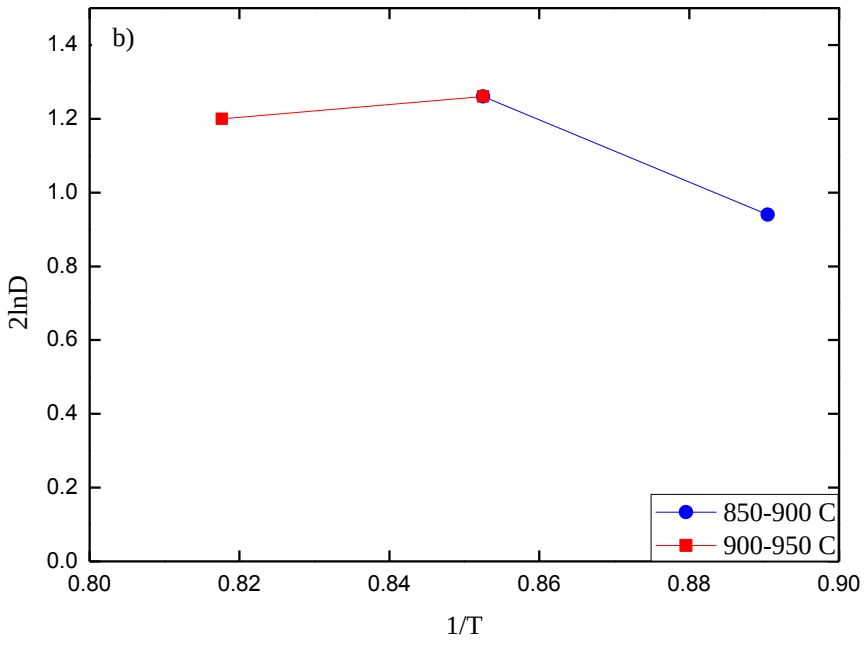

Figure 4.22 Plot of 2 lnD (average particle size) vs. 1/T for 2 h in (b) NaCl flux. (The lines are for visual help). (cont'd)

In Figure 4.22 (a), apparent activation energy for the formation of BaHF in molten KCl is seen to be 96.38 kJ/mol between 850 and 900 °C, whereas the apparent activation energy becomes negative between 900 and 950 °C for the calcination duration of 2 h showing the dominance of another mass transport mechanism rather than diffusion. In the case of NaCl flux, apparent activation energy is seen to be 70.09 kJ/mol between 850 and 900 °C, which turns to be negative between 900 and 950 °C as in the case of KCl flux (Figure 4.22 (b)).

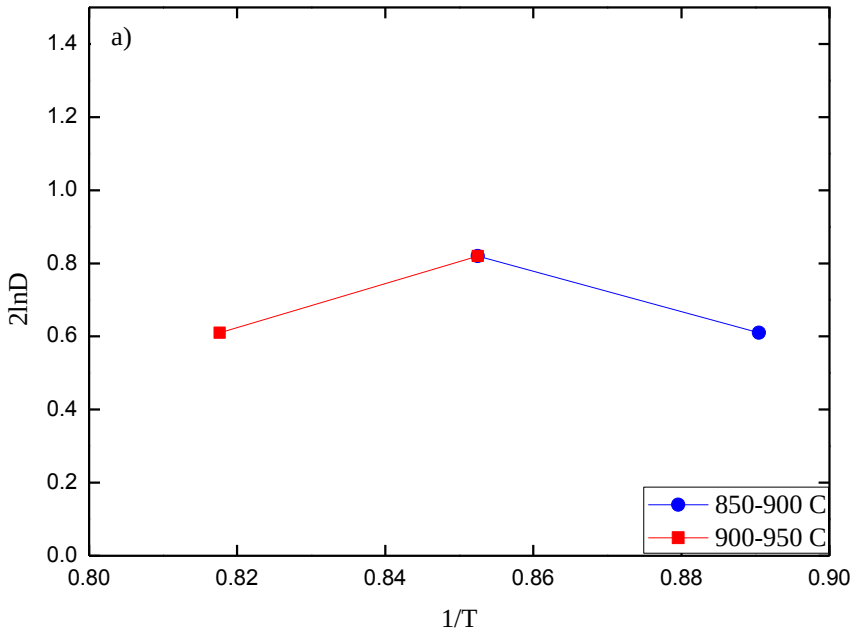

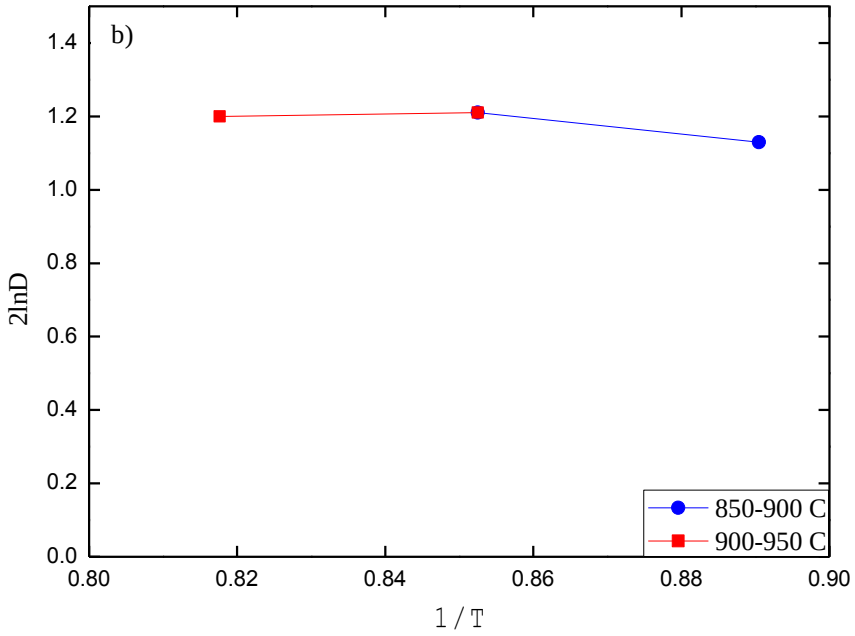

Figure 4.23 Plot of 2 lnD (average particle size) vs. 1/T for 2.5 h in (a) KCl flux (b) NaCl flux. (The lines are for visual help).

In Figure 4.23 (a), apparent activation energy for the formation of BaHF in molten KCl is seen to be 45.99 kJ/mol between 850 and 900 °C, whereas the apparent activation energy becomes negative between 900 and 950 °C for the calcination duration of 2.5 h showing the dominance of another mass transport mechanism rather than diffusion. In the case of NaCl flux, apparent activation energy is seen to be 17.52 kJ/mol between 850 and 900 °C, which turns to be negative between 900 and 950 °C as in the case of KCl flux (Figure 4.23 (b)).

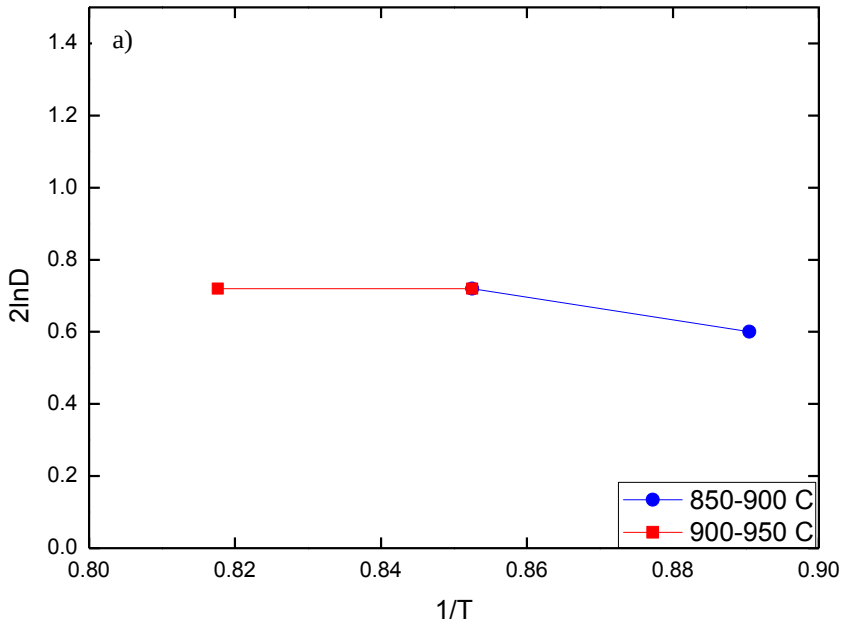

Figure 4.24 Plot of 2 lnD (average particle size) vs. 1/T for 3.5 h in (a) KCl flux. (The lines are for visual help).

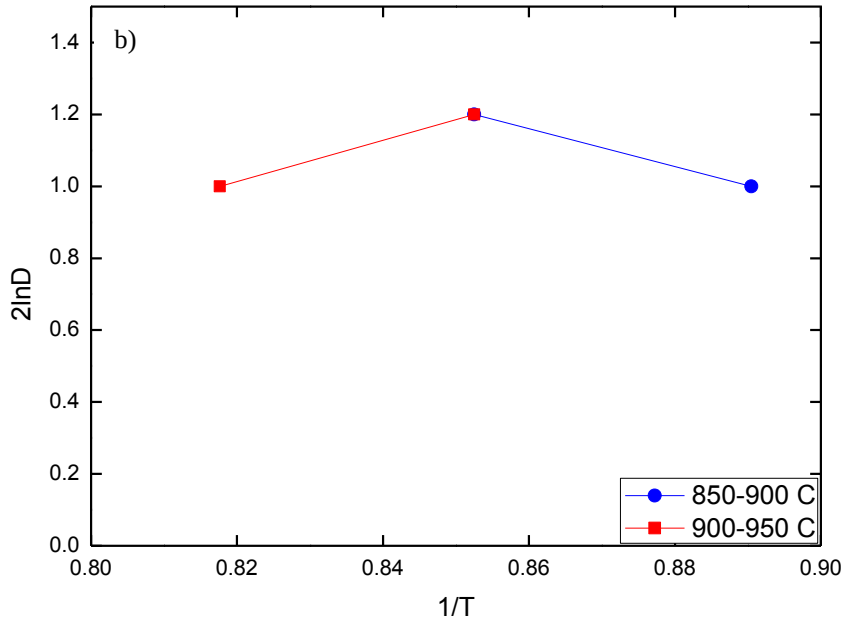

Figure 4.24 Plot of 2 lnD (average particle size) vs. 1/T for 3.5 h in (b) NaCl flux. (The lines are for visual help). (cont'd)

In Figure 4.24 (a), apparent activation energy for the formation of BaHF in molten KCl is seen to be 26.28 kJ/mol between 850 and 900 °C, whereas the apparent activation energy becomes negative between 900 and 950 °C for the calcination duration of 3.5 h showing the dominance of another mass transport mechanism rather than diffusion. In the case of NaCl flux, apparent activation energy is seen to be 43.81 kJ/mol between 850 and 900 °C, which turns to be negative between 900 and 950 °C as in the case of KCl flux (Figure 4.24 (b)).

As well as platelet size and morphology, amount of BaHF formation in the structure is critical. Figure 4.25, 4.26, 4.27 and 4.28 show the BaHF amount formed during calcination at 900 °C for 1h, 2h, 2.5h and 3.5h, respectively as a function of flux composition determined using quantitative XRD analysis. It is obvious that formation of BaHF phase within the structure is lower in the case of synthesis in pure KCl flux for almost all the calcination periods. With the increase in the NaCl content, BaHF phase amount increases. Quantitative analysis shows an

obvious increase in the BaHF formation amount with the increasing calcination times; however, aspect ratio of the platelets decreases. Optimized platelet size and BaHF amount is obtained for 2 h calcination durations. At this calcination period, NaCl-rich flux increase will increase BaHF phase till 90 wt% NaCl-10 wt% KCl flux composition, where it reaches to its maximum value of ~97.5%.

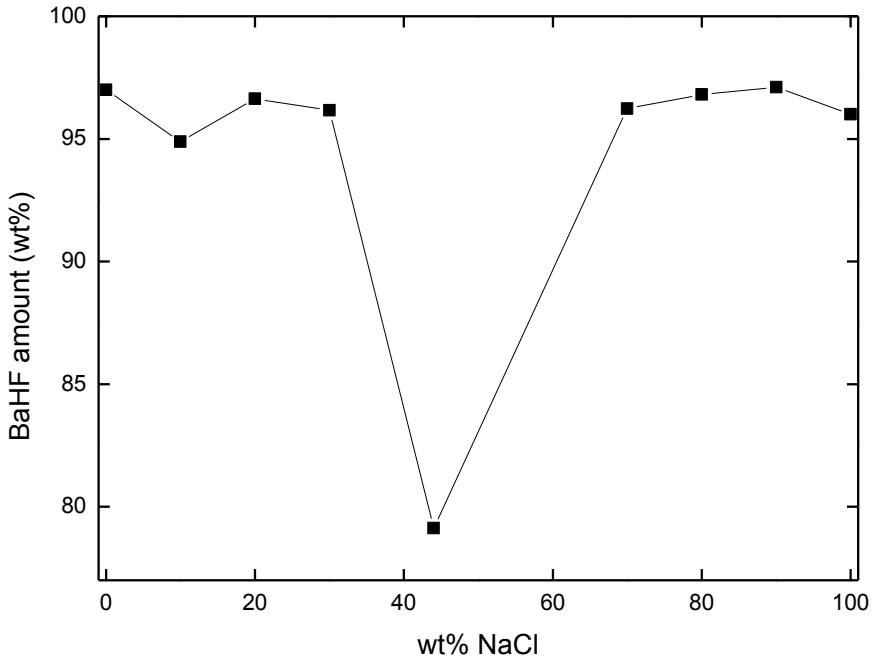

Figure 4.25 Quantitative X-ray analysis of platelets having different compositions and sintered at 900 ˚C for 1 h.

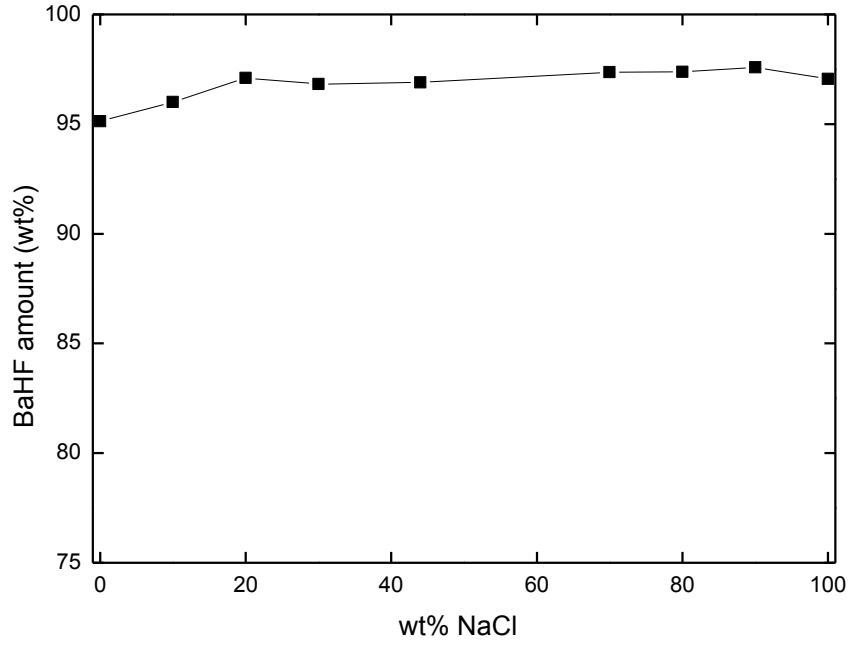

Figure 4.26 Quantitative X-ray analysis of platelets having different compositions and sintered at 900 ˚C for 2 h.

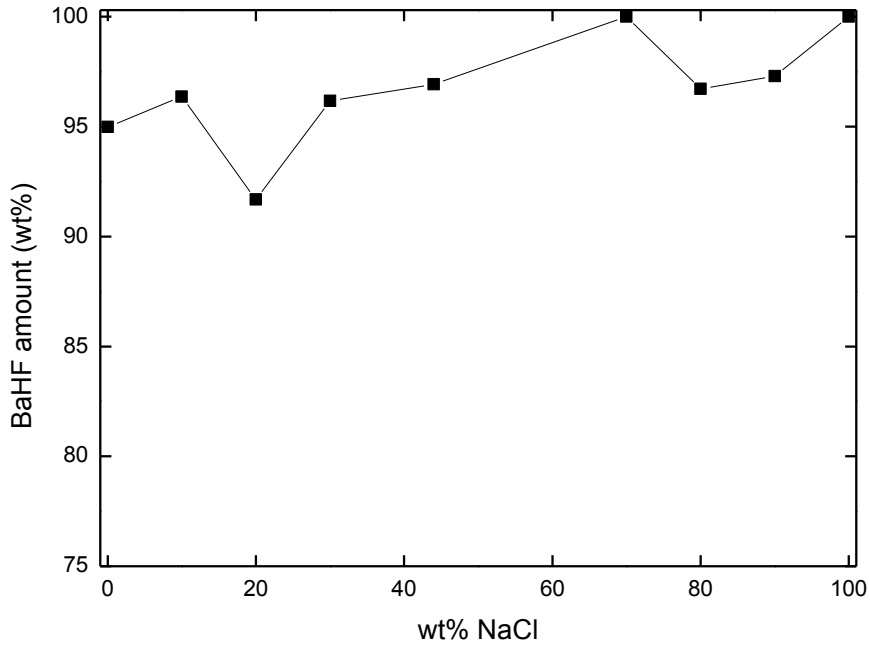

Figure 4.27 Quantitative X-ray analysis of platelets having different compositions and sintered at 900 ˚C for 2.5 h.

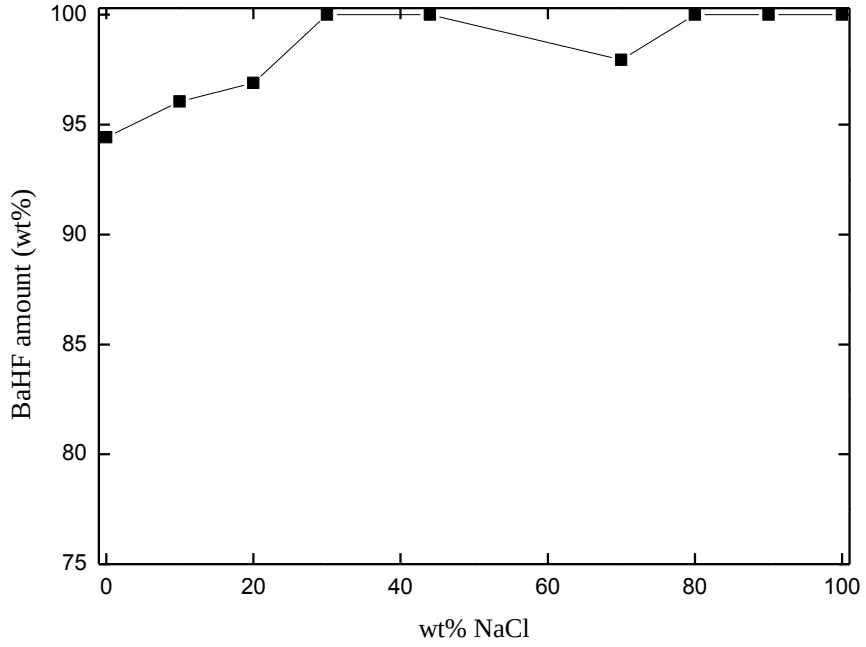

Figure 4.28 Quantitative X-ray analysis of platelets having different compositions and sintered at 900 ˚C for 3.5 h.

4.2. Microstructure and Texture Analysis of Multilayered BaHF Ceramics

4.2.1. Microstructure of Multilayered BaHF Ceramics Produced by Platelets Synthesized via MSS

SEM analyses were conducted on both the planer surface and cross-section of the multilayered structure. Figure 4.29 shows the microstructure of planar surface and cross-section of the five-layer structure heated to 1000 ˚C with 4 ˚C/min rate and sintered for 4 hours. Although the ideal sintering temperature of BaHF is about 1250 ˚C, present samples were sintered at lower temperatures because they sticked to the alumina plates at that temperature. As the figures show, there is no texture within the structure since the size of the initial platelets obtained by molten salt synthesis is too small for TGG to efficiently occur.

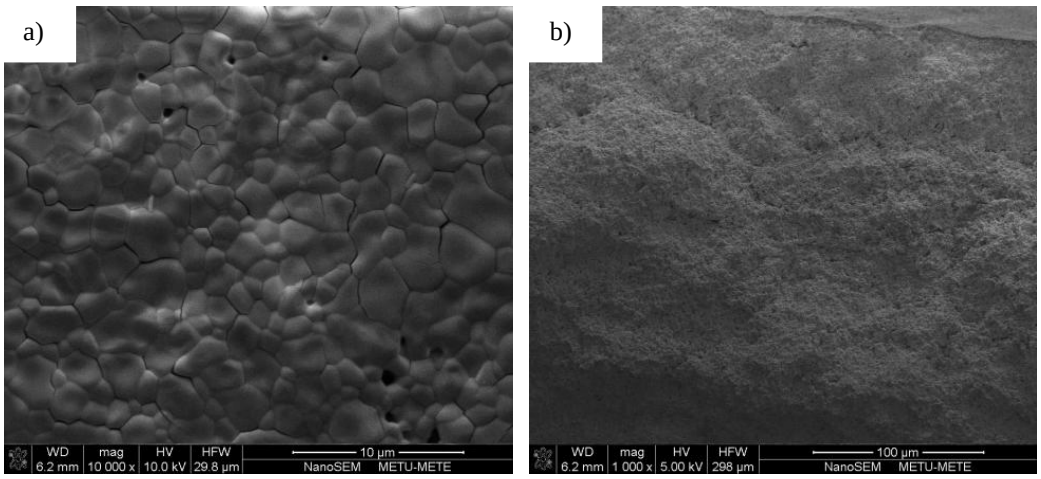

Figure 4.29 (a) Planar surface (b) Cross-section of the five-layer BaHF ceramics sintered at 1000 ˚C for 4 hours.

Figure 4.30 shows the planar surface and cross-section of the five-layer BaHF structure heated to 1100 ˚C with 4 ˚C/min rate and sintered for 4 hours. Since the size of the initial platelets is too small, there is still no texture formation within the structure even at a higher sintering temperature.

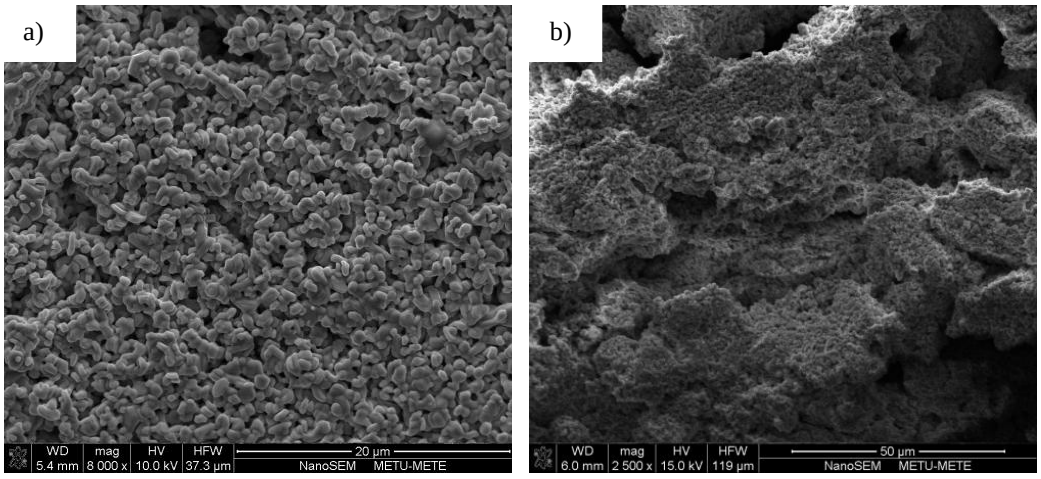

Figure 4.30 (a) Planar surface (b) Cross-section of the five-layer BaHF ceramics sintered at 1100 ˚C for 4 hours.

4.2.2. Microstructure of Multilayered BaHF Ceramics Produced by Platelets Synthesized via RTGG from BiF Seed Crystals

Figure 4.31 shows the SEM images of the multilayered ceramic. It is composed of 5 layers and layers are completely adhered. From the micrographs the grain size can be determined as ~ 35 μm. Cross-sectional view of the microstructure (Figure 4.31 (b)) shows a week degree of texture formation which is evidently much higher compared to those observed in other two cases presented in Figure 4.29 (b) and Figure 4.30 (b), however.

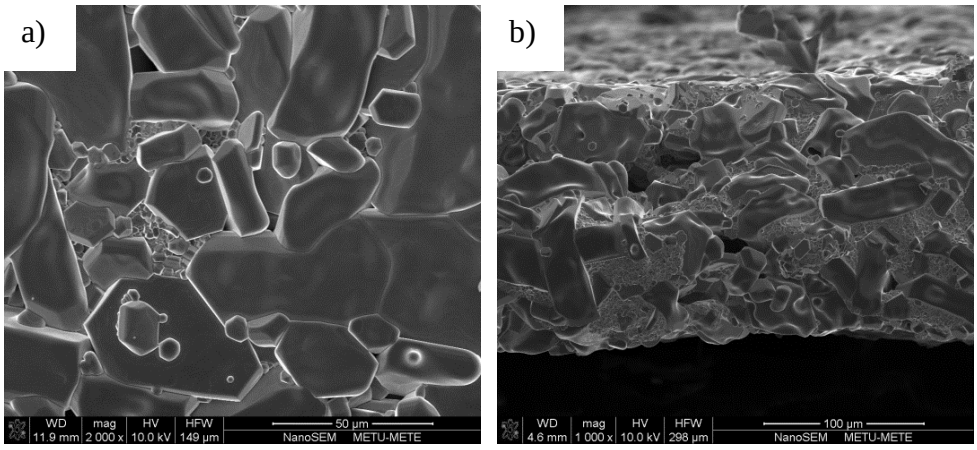

Figure 4.31 (a) Planar surface (b) Cross-section of the five-layer ceramic that was heated to 1000 ˚C with 4 ˚C/min rate and sintered for 2 h followed by heating to 1250 ˚C with 4 ˚C/min rate, held for 5 hours and cooled in the furnace.

4.2.3. Texture Analysis of Multilayered BaHF Ceramics

4.2.3.1. Texture Analysis by Rietveld Refinement Method

For the texture analysis, it is critical to make Rietveld analysis of BaHF ceramics both in powder form and in textured bulk form. XRD diffractograms of the powder and the textured sample taken perpendicular to its planar surface are shown in Figure 4.32 for Cu K_α radiation.

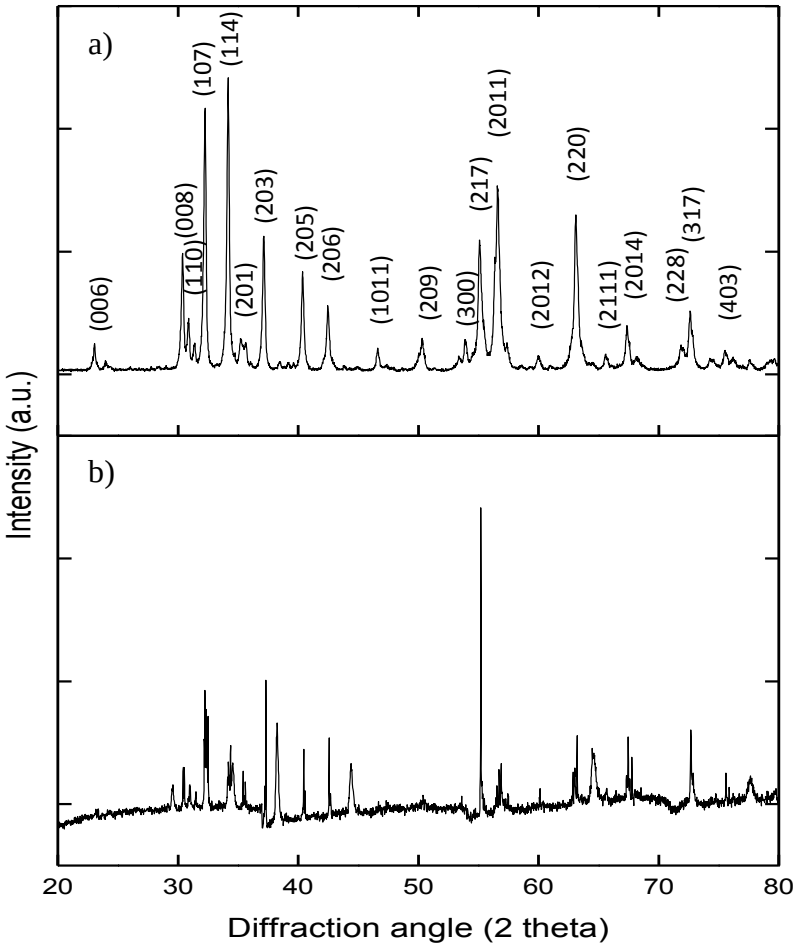

Figure 4.32 X-ray diffraction spectrum of (a) powder BaHF, (b) textured bulk BaHF for Cu K_α radiation. (JCPDS-ICDD card no. for BaHF is 43-0002).

Figure 4.33 (a) shows the calculated and observed peaks as well as their difference without introducing any texture function. Figure 4.33 (b) and (c) show XRD patterns calculated by Spherical Harmonics (SH) and March-Dollase (MD) functions and observed XRD data together with the difference in the calculated and observed diffraction patterns. For the case of Rietveld analysis of powder BaHF ceramic, calculated and observed patterns fit perfectly. However, the difference between the observed and calculated peaks (shown by blue in Figure 4.33 (b) and (c)) reveals that even with the introduction of preferred orientation functions, Rietveld refinement does not reveal ideal results due to the presence of some phases in the produced bulk ceramics other than BaHF.

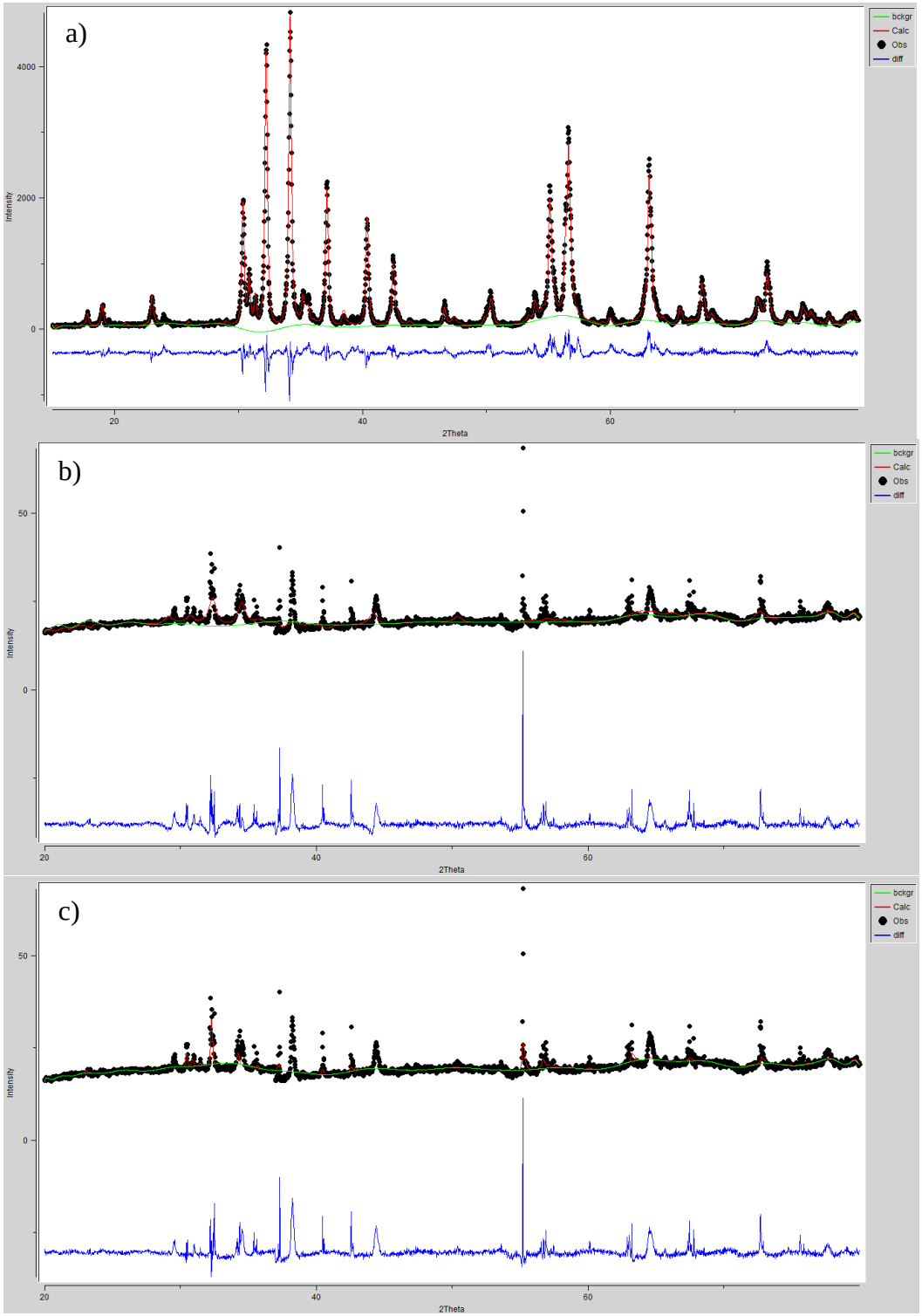

Figure 4.33 The calculated (red) and observed (black) XRD patterns for (a) powder BaHF (b) textured BaHF by Spherical Harmonics function (c) textured BaHF by March-Dollase function. The difference between the calculated and observed XRD patterns is also shown (blue).

Table 4.2 shows Rietveld analysis results for powder and textured bulk BaHF. As a result of Rietveld refinements, lattice parameters and densities of both powder and textured bulk BaHF ceramics refined by MD and SH functions are seen to be close to the theoretical values. Cagliotti terms which are instrument response functions for Bragg-Brantano diffraction (GU, GV and GW) and isotropic thermal factors (U_{iso}) are found as expected (GV should be negative and others should be at least zero in order to minimize least-square error of structure factors). Moreover, Lorentzian coefficients LX and LY showing the particle size and microstrain, respectively are reasonable for powder BaHF and textured ceramic refined by SH function; however, LY is zero in the case of textured ceramic refined by MD function which is an unexpected result since strain cannot be zero for the materials processed by shear deformation (tape casting). Also, atomic positions as a result of Rietveld refinements show similarity with the theoretically resulting ones.

Table 4.2 Results for Rietveld refinement of BaHF using Bragg-Brentano diffraction data.

Parameter	***Powder BaHF***				***Textured BaHF (M-D)***				***Textured BaHF (S-H)***				***Theoretical BaHF***			
Lattice Parameter (Å) a,b	5.892401				5.886598				5.865731				5.892402			
c	23.20358				23.210197				23.350460				23.203585 [111]			
Density (g/cm3)	5.729				5.300				5.316				5.26 [113]			
Mass (g/unit cell)	2406.987				2222.950				2227.398							
GU	0				101.686				0							
GV	-31.7367				-2				-20.4							
GW	18.3901				21.5721				9.73876							
LX	17.3670				0.282284				45.4832							
LY	0				0				27.9942							
Absorption Coefficient (A_{B1})	0				0				0.00786617							
Scale Factor	13.785				0.011889				0.087523							
	U_{iso}	x	y	z	U_{iso}	x	y	z	U_{iso}	x	y	z	x	y	z [111]	
Ba	0	0.33	0.67	0.25	0.00	0.33	0.67	0.25	0.08	0.33	0.67	0.5	0.33	0.67	0.25	
Fe1	0.01	0	0	0	0.00	0	0	0	0.17	0	0	0	0	0	0	
Fe2	0	0	0	0.55	0.00	0	0	0.26	0.00	0	0	0.23	0	0	0.26	
Fe3	0.00	0.67	0.33	0.02	0.00	0.67	0.33	0.03	0.00	0.67	0.33	0.03	0.67	0.33	0.03	
Fe4	0	0.67	0.33	0.19	0.00	0.67	0.33	0.18	0.00	0.67	0.33	0.20	0.67	0.33	0.19	
Fe5	0	0.17	0.34	0.11	0.00	0.17	0.33	0.11	0.04	0.16	0.33	0.10	0.17	0.34	0.11	
O1	0.05	0	0	0.20	0.00	0	0	0.16	0.00	0	0	0.10	0	0	0.15	
O2	0	0.33	0.67	0.08	0.01	0.33	0.67	0.09	0.01	0.33	0.67	0.02	0.33	0.67	0.05	
O3	0.01	0.83	0.65	0.25	0.01	0.77	0.54	0.25	0.05	0.94	0.89	0.25	0.82	0.63	0.25	
O4	0	0.85	0.70	0.05	0.00	0.83	0.66	0.05	0.00	0.87	0.73	0.06	0.84	0.68	0.05	
O5	0	0.51	1.00	0.14	0.01	0.51	1.00	0.15	0.01	0.46	0.91	0.20	0.50	0.99	0.15	
R_{wp}(%)	13.86				30.63				30.48							
R_p(%)	11.02				12.15				11.47							
χ^2	6.754				0.09764				0.1076							

Texture analysis that is done using March-Dollase function gives the parameters that can be used for the calculation of the measured texture distribution (Equation 2.6). Figure 4.34 shows both the fraction distribution of crystallites that are associated with a particular orientation axis along with the texture factors. When *f* (fraction in Figure 4.34) and *r* (ratio in Figure 4.34) parameters are inserted to the formula together with the ω angle which is the angle between the normal of the

specified plane and (00l), the highest texture degree can be seen on (006) plane. Figure 4.34 shows only the fraction and texture factor; however, Equation 2.6 also contains ω angle which can be obtained by basic geometrical calculations. For that reason, fraction and ratio values do not give information about the degree of texture without ω angle, directly. Nevertheless, texture index value (*r*) approaching to 0 and fraction value (*f*) approaching to 1 show the strong existence of preferred orientation in bulk BaHF ceramics produced by tape casting utilizing TGG.

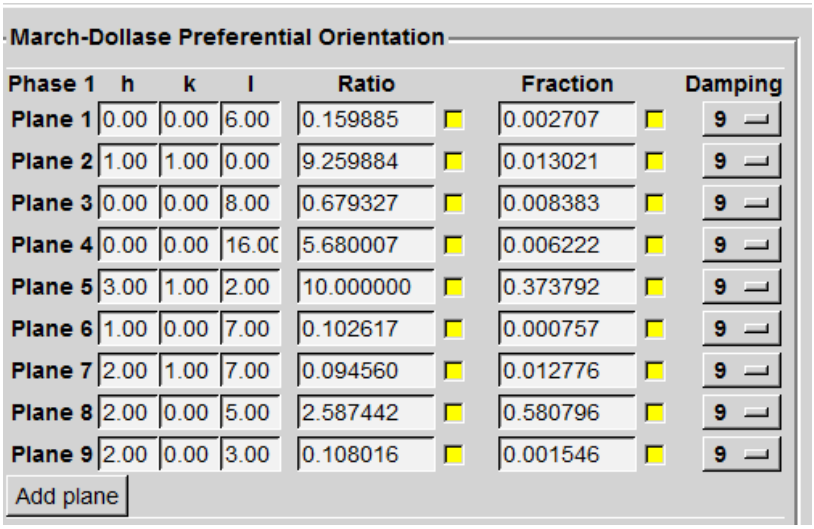

Figure 4.34 Results of March-Dollase function showing fraction distribution of crystallites that are associated with a particular orientation axis and texture factors.

Equation 4.2 can be applied for this textured sample, since the intensity of (006) plane has risen mostly due to the highest degree of diffraction as a result of texture, and since the lowest amount of diffraction is on (110) plane that is perpendicular to (006) plane due to the alignment of the platelets along (006) plane. From the diffractogram obtained by the GSAS (General Structure Analysis System) refinement, intensity values can be read and degree of texture (G) can be found as in the Table 4.3. G value of 1 shows completely random distribution while 0 shows the existence of 100% preferred orientation. As it is clear from Table 4.3, March coefficient (G) obtained from MD function is 0.67 meaning that the degree of texture within the bulk ceramic is 33%.

$$I_{006} / I_{110} = 0.10953 G^{-4.701} \quad (4.2)$$

Table 4.3 Texture analysis results for Rietveld refinement of BaHF using March-Dollase function.

Sample	I(006)/I(110) (observed)	G_{obs} (March coefficient)
Textured BaHF	19/226=0.73	0.67

Texture analysis that is conducted using Spherical Harmonics function gives the texture index as 7.555 in Figure 4.35. This is the indication of the existence of texture because it is well above 1 which shows the random distribution. Since the sample has fiber texture (where all of its basal plane normals [001] are assumed to perpendicular to the tape casting direction), it has cylindrical symmetry, and hence, the most suitable order for this sample is 12th order. The order is determined experimentally according to the suitability of the fit and decrease in the goodness of fit (χ^2).

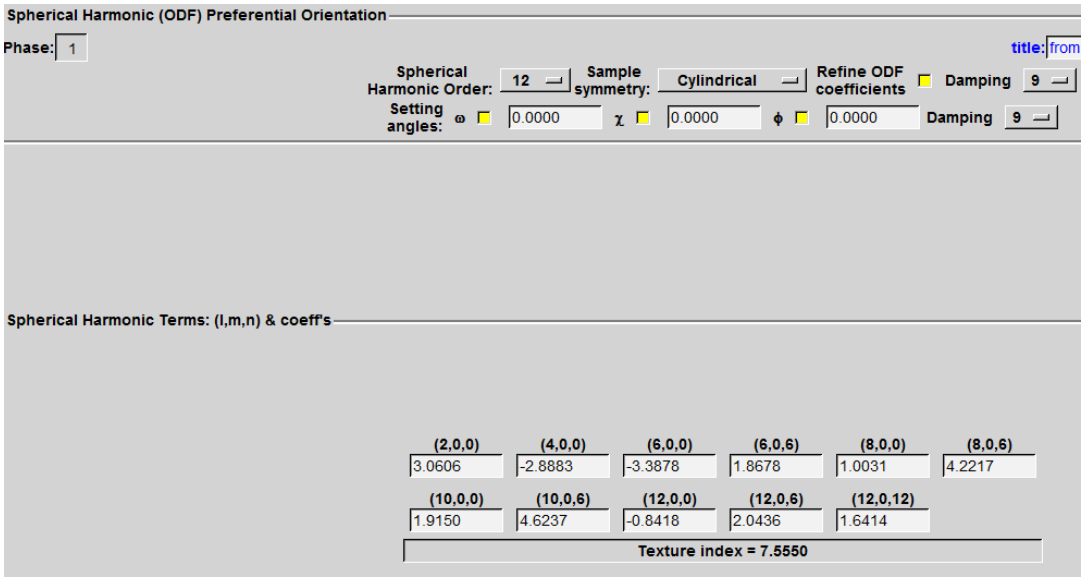

Figure 4.35 Analysis results of spherical harmonics function showing related coefficients, symmetry and texture index.

After the refinement with spherical harmonics function, pole figures of (006) and (110) are drawn as in Figure 4.36. GSAS draws the pole figures using the spherical harmonics terms (l,m,n) and coefficients as can be seen in Figure 4.35. Nonhomogeneous distribution of the contours in the pole figure on (006) plane shows the presence of texture. Similarly, distribution of contours on (110) pole figure is nonhomogeneous confirming the existence of texture on the (006) plane. This result is acceptable, since when the faces of platelets are parallel to (006) plane, the planes along their thickness are parallel to (110) plane.

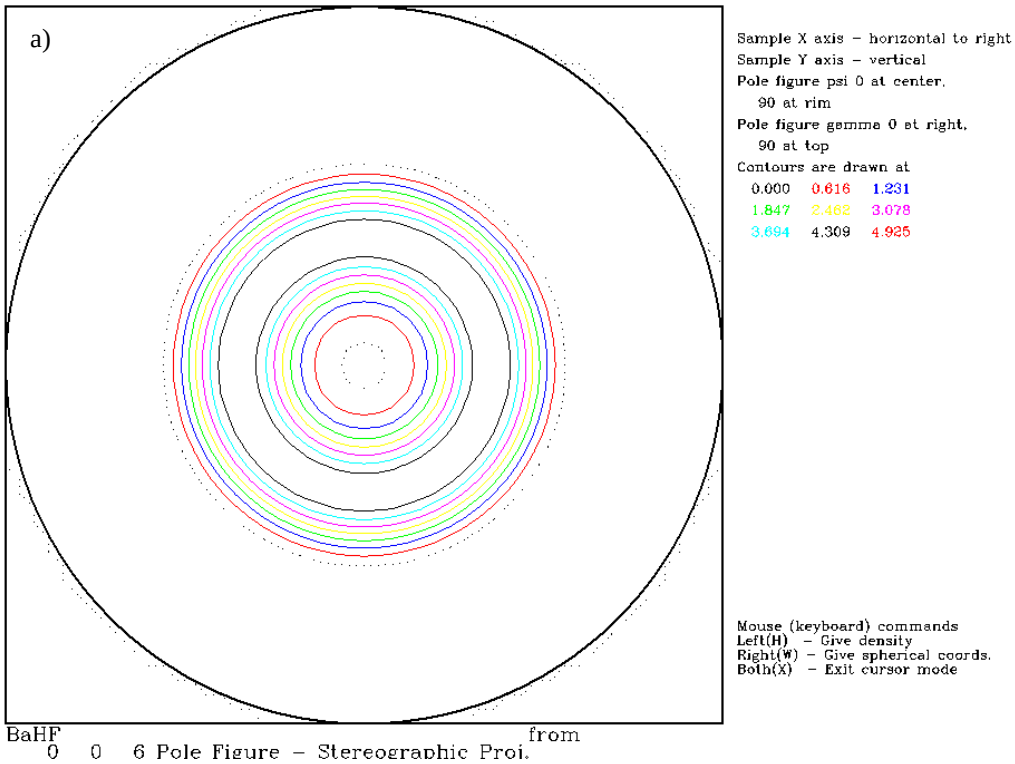

Figure 4.36 Pole figure of (a) (006) plane as a result of refinement by Spherical Harmonics function.

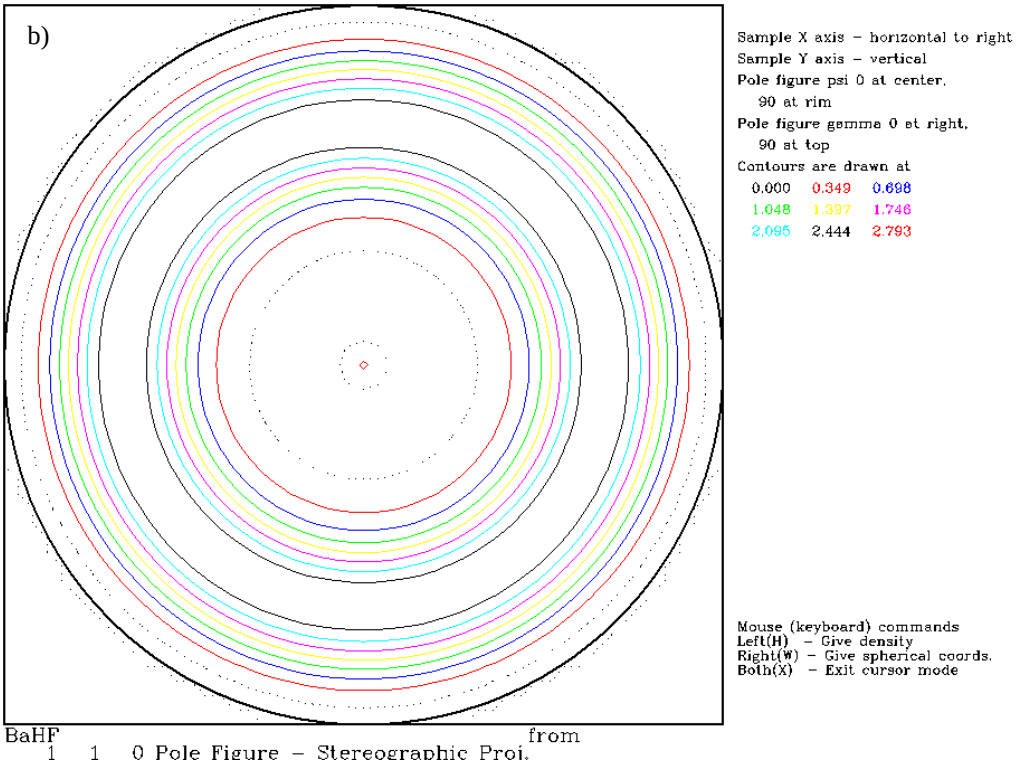

Figure 4.36 Pole figure of (b) (110) plane as a result of refinement by Spherical Harmonics function. (cont'd)

Since the grain size of the textured BaHF is much larger than 1μm and instrumental broadening is calibrated with the strain free-annealed standard Si powder, peak broadening has resulted only from the strain that is introduced during the tape casting step. Consequently, there was no need to calculate Williamson-Hall plot for the textured ceramic, as it shows the dominance of only the strain effect on the peak broadening. On the other hand, it was necessary to calculate the Williamson-Hall plot for the powders having~500 nm size. Figure 4.37 shows the Williamson-Hall plot for the powder ceramics. Equation 4.3 is the general formula of the peak broadening according to Lorentzian peak shape. B stands for total broadening while B_{strain}, $B_{inst.}$and B_{size} represent broadening caused by strain, instrument and crystallite size, respectively.

$$B = B_{strain} + B_{inst.} + B_{size} \tag{4.3}$$

Since the instrumental broadening was calibrated, broadening has resulted from size and strain.

$$B = B_{strain} + B_{size} \tag{4.3'}$$

Resulting L_y (Lorentzian coefficient of microstrain) after the refinement gives the amount of the strain which is zero for the case of powder BaHF. This means that all of the broadening introduced should have resulted from the size effect only.
In order to find size broadening, Scherrer constant for randomly distributed powder samples was required and it was found as 1.123 [114] where Cu K_α is 1.54056 Å. Equation 4.4 is the total broadening term containing only the size broadening.

$$B = \frac{K \cdot \lambda}{t \cdot \cos\theta} \tag{4.4}$$

Here, K is the Scherrer constant, λ is the wavelength of Cu K_α, t is the average size of the powders and θ is the diffraction angle.
After the calculation of the broadening term with respect to the diffraction angle, Williamson-Hall plot according to Lorentzian peak shape can be drawn as in Figure 4.37. $\frac{B\cos\theta}{\lambda}$ value of 0.000225 being constant for all $\frac{\sin\theta}{\lambda}$ values shows that size broadening is significant rather than the strain broadening.

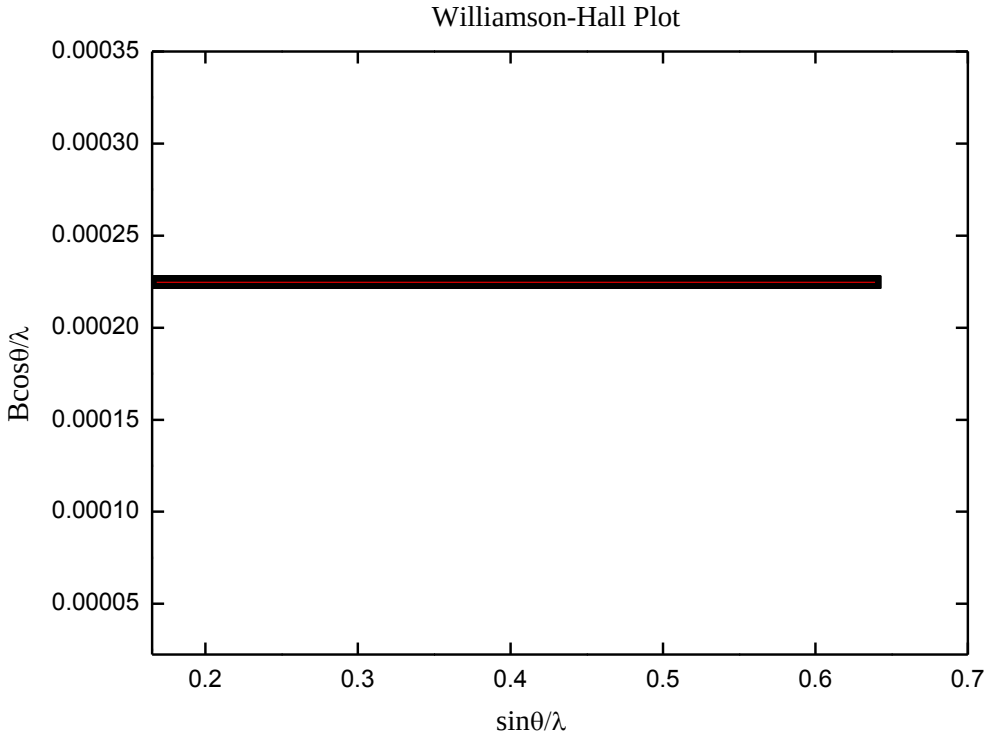

Figure 4.37 Williamson-Hall plot of powder BaHF having particle size of~500 nm.

In Figure 4.37, intersection point of the line with the y axis gives 1/*t* value that is 0.000225 resulting in the powder size of 445.24 nm which is close to the actual average particle size of powders (~500 nm).

$$\frac{1}{t} = 0.0002246 \Rightarrow t = 445.24nm$$

Consistency of the particle size values observed on the Williamson-Hall plot and the actual size of the particles confirms the reliability of Rietveld refinements, since total broadening also includes instrumental broadening that was obtained by Si calibration sample.

4.2.3.2. Texture Analysis by Pole Figure Measurements

Another method for the texture analysis is the pole figure measurement. According to 2-D and 3-D pole figures of (006) plane (Figure 4.38), it can be said that there exist some texture on this plane due to the nonhomogenity of the poles observed. However, degree of texture seems to be not so high where this nonhomogenity is not so sharp.

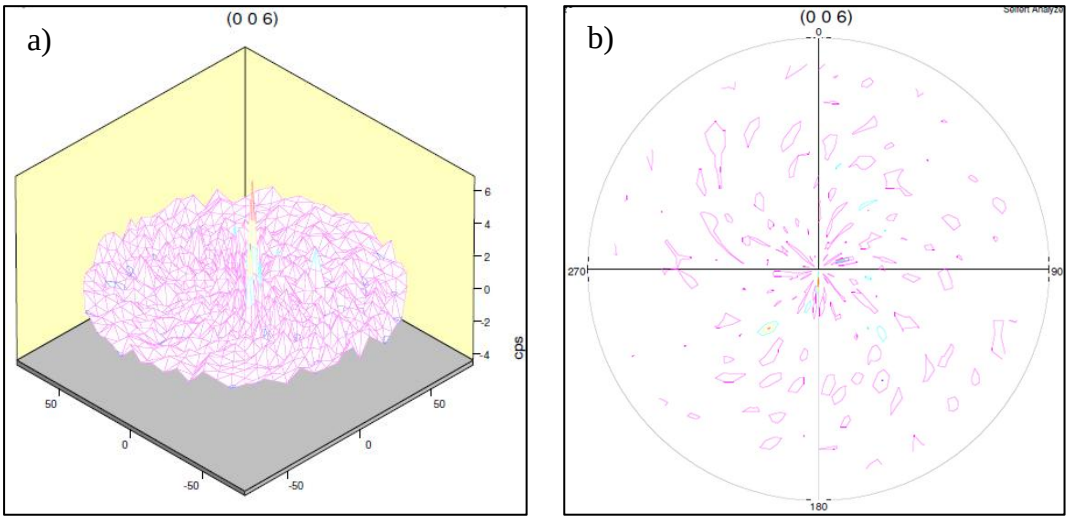

Figure 4.38 (a) 3-D appearance and (b) 2-D appearance of pole figures of (006) plane.

4.2.3.3. Texture Analysis by EBSD Characterization

After the preparation of the bulk textured BaHF sample surface, EBSD analysis was conducted for the texture analysis. EBSD characterization results showed that the ceramic that was produced by tape casting using platelets synthesized by RTGG from BiF seed crystals has some degree of texture. Even in the as-received form (before the metallographic preparation), EBSD analysis showed the presence of texture on (001) plane due to the localized distribution of poles (Figure 4.39 (a) and (b)). EBSD mapping of the unprepared surface is not successful expectedly, since colours should be revealing the existance of grains in their crystallographic

orientation. Also, some additional processing programs should have been used to remove irrelavent points from which diffraction could not be taken.

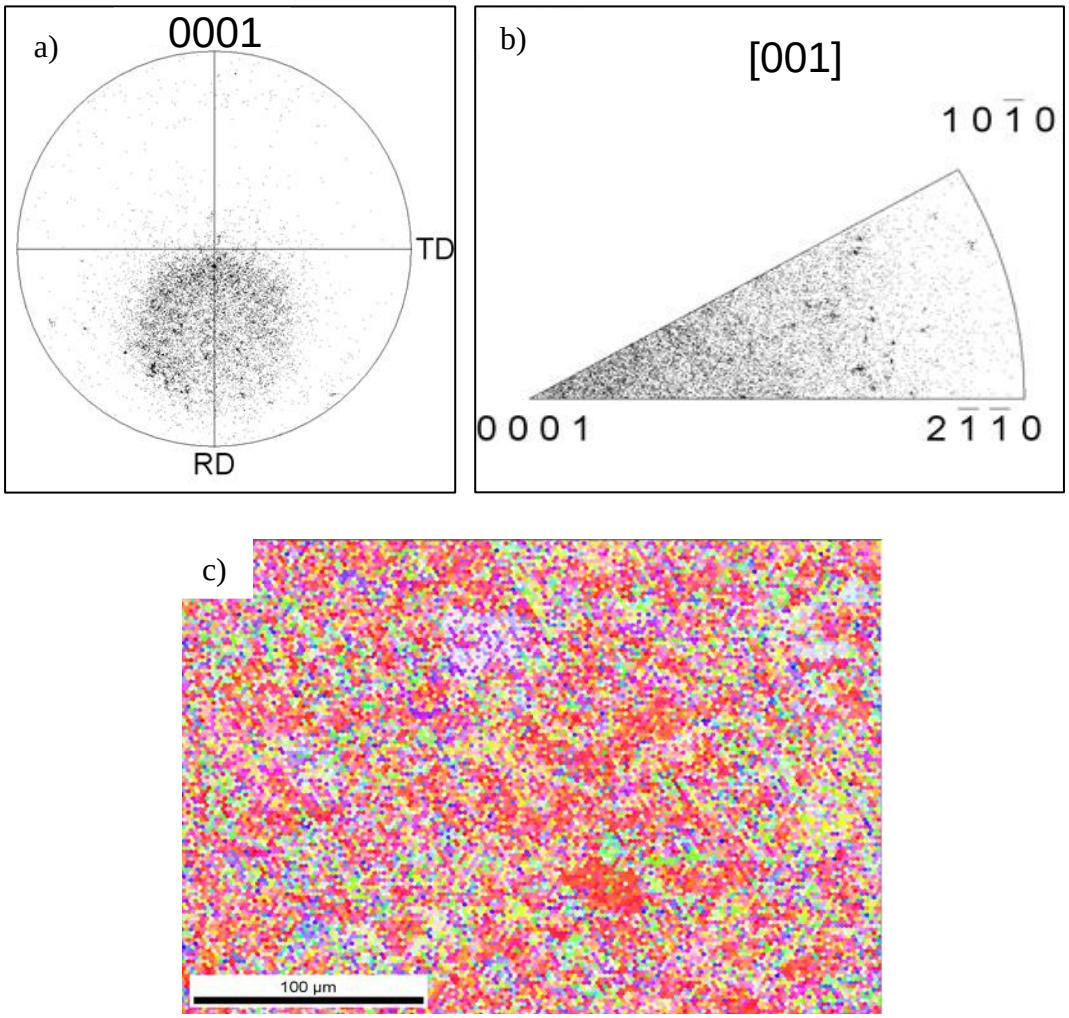

Figure 4.39 EBSD texture analysis showing the presence of texture on (001) plane for the ceramic before surface preparation.

When the ceramic surface was metallographically prepared, the results became more meaningful, and the diffraction patterns were seen more obviously (Figure 4.40 (a)). Hough transform, which is used for converting the diffraction lines to

bright spots, was used to reveal the diffraction patterns which are not obvious in Figure 4.40 (b).

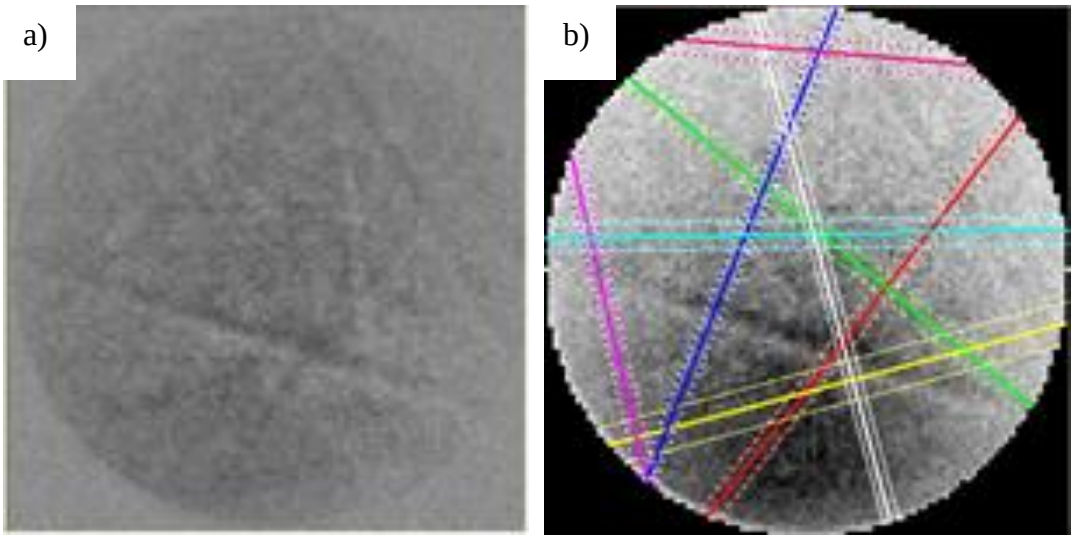

Figure 4.40 EBSD diffraction pattern of BaHF textured ceramic after surface preparation (a) without processing with Hough Transform (b) with processing with Hough Transform.

Figure 4.41 shows the EBSD analysis result indicating the texture on (0001) plane by pole figure and inverse pole figures. In Figure 4.41 (a) pole figure distribution on (0001) plane is not homogenous. Furthermore, inverse pole figures measurement indicates that the degree of distribution of the grains on (0001) plane is higher since the poles are localized on this plane as in Figure 4.41 (b). Mapping seems to be better compared to the mapping of the unprepared surface, yet it still requires to be processed by another processing programs like Channel5 software for further improvement.

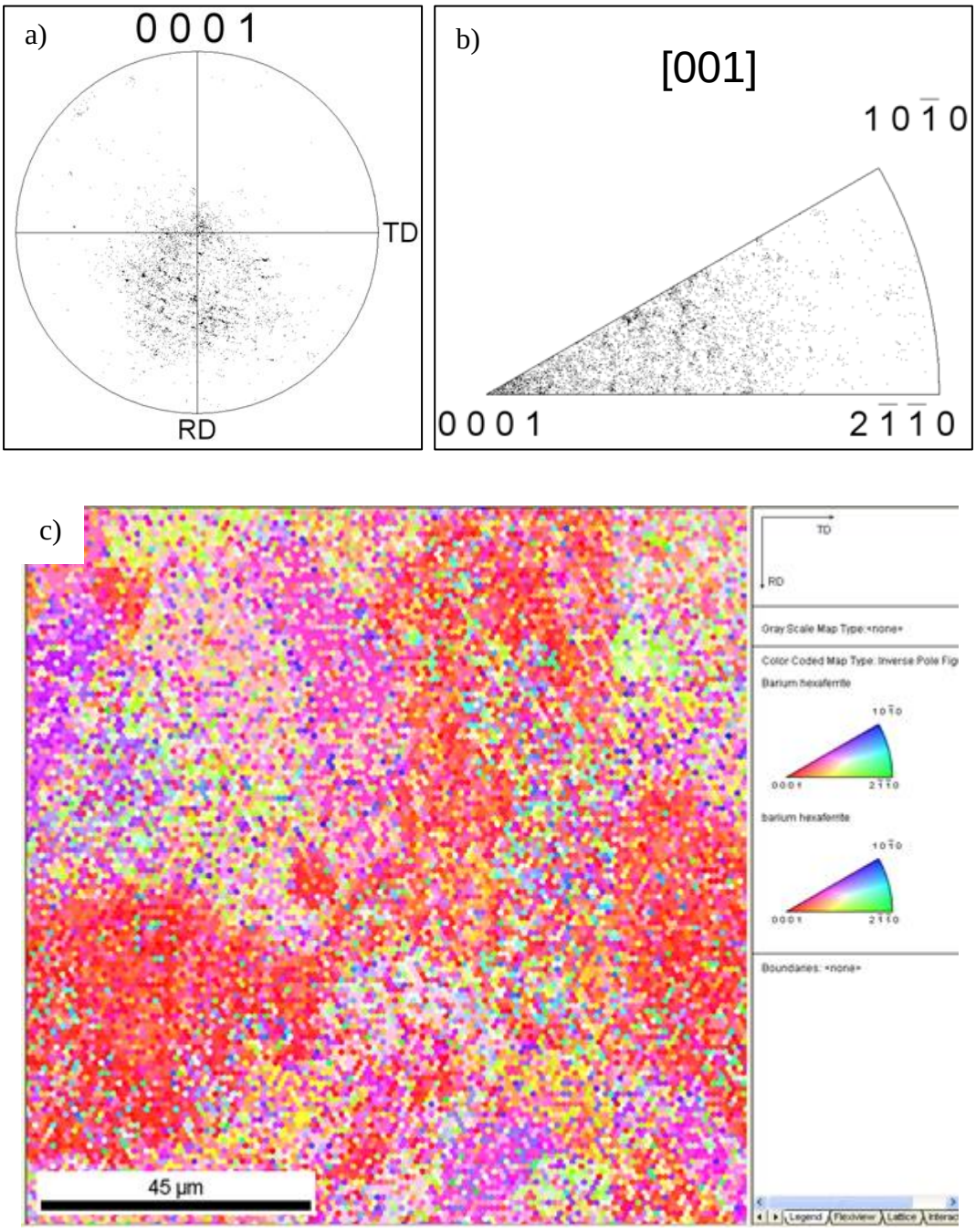

Figure 4.41 EBSD analysis results indicating the texture on (001) plane by (a) pole figure and (b), (c) inverse pole figures.

CHAPTER 5

DISCUSSION

ICP-MS and XRD results, which were used for the investigation of BaHF formation mechanism, showed that solubility of Fe_2O_3 in both KCl and NaCl is almost zero. On the other hand, $BaCO_3$ dissolves in the flux and reacts with Fe_2O_3 particles. From the final size of the BaHF platelets, which was determined by quantitative metallographic measurements on SEM images, it was concluded that a BaHF platelet of size ~1-3 μm could not have formed from a single hematite particle of ~200 nm average size by growth mechanism. There should be Fe_2O_3 clusters forming a single BaHF platelet. Since $BaCO_3$ dissolves in the flux completely, and Fe_2O_3 has no solubility in the molten salts, formation of BaHF should occur via wetting of Fe_2O_3 by the flux containing Ba^{+2} and O^{-2} ions. As a result, its wettability by the flux should be effective on both the amount of BaHF formation and platelet size, and hence, apparent activation energy for the formation of BaHF. Figure 5.1 shows the apparent wettability characteristics of Fe_2O_3 by molten NaCl and KCl. Apparent contact angle between Fe_2O_3 surface and molten NaCl was measured as 46.7˚ while it was 64.1˚ in the case of KCl at 700 ˚C. Lower apparent contact angle shows more effective wettability of Fe_2O_3 by NaCl flux compared to the KCl.

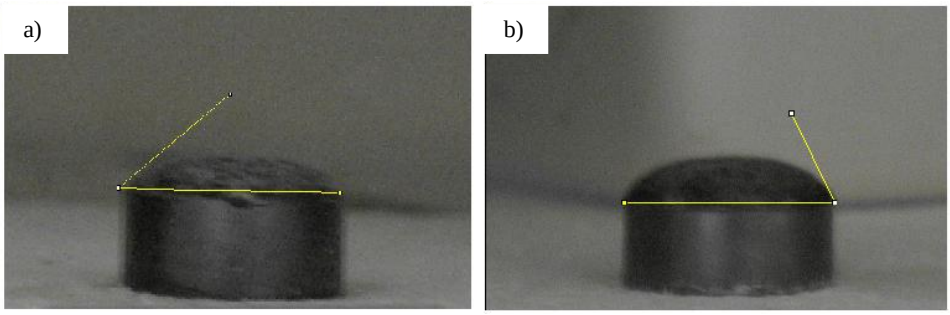

Figure 5.1 Typical images showing (a) the apparent contact angle (46.7˚) for NaCl (b) the apparent contact angle (64.1˚) for KCl at 700 ˚C.

From the experiments which were conducted in short calcination times even for the calcination time of 10 minutes, it can be seen that the first precipitating phase is $Ba_5Fe_{14}O_{26}$ as in Figure 5.2. With the increase in the $BaCO_3/Fe_2O_3$ ratio, the amount of this phase increases since the amount of $BaCO_3$ dissolving in the flux increases leading to the formation of Ba-rich compound (Figure 4.3). However, for the longer calcination times and low $BaCO_3/Fe_2O_3$ ratio, this phase disappears leaving the place to $BaFe_{12}O_{19}$ due to the homogenization of Ba^{2+} and O^{2-} ions throughout the system.

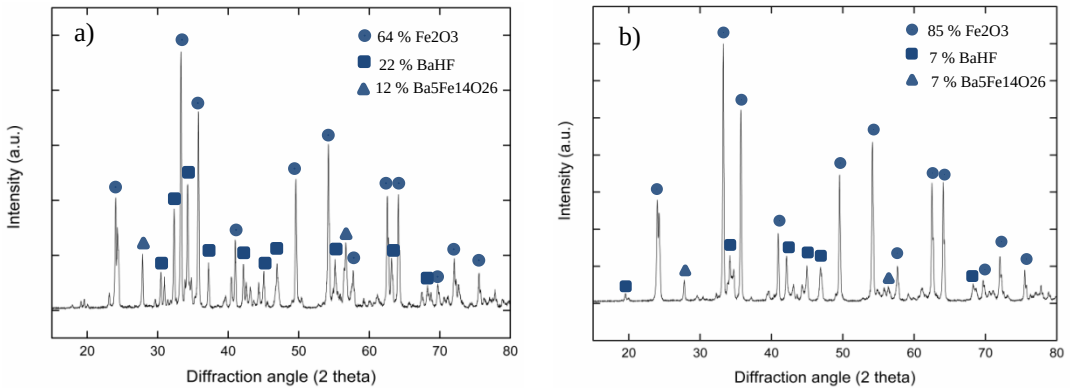

Figure 5.2 X-ray diffractogram of platelets calcined at 900 ˚C for 10 minutes in (a) NaCl flux and (b) KCl flux.

Until the homogenization of the ions within the system, proportions of the stable phases ($BaFe_{12}O_{19}$ and $Ba_5Fe_{14}O_{26}$) fluctuate. These phases form in Fe_2O_3 particles as concentric rings as Ba^{2+} and O^{2-} diffuses to the solid particle from the flux. In this case, if all the platelets were composed of the rings of Fe_2O_3, BaHF and $Ba_5Fe_{14}O_{26}$ from inner to the outer part, there would not be any fluctuations in the fraction of these phases; the fraction of Fe_2O_3 would continuously decrease. For that reason, together with the platelets that are composed of the rings of Fe_2O_3, BaHF and $Ba_5Fe_{14}O_{26}$ from inner to the outer part, there should be some small and large particles which are fully composed of $Ba_5Fe_{14}O_{26}$ and Fe_2O_3 within an agglomerate. Under these circumstances, $Ba_5Fe_{14}O_{26}$ phase decomposes when the Ba^{2+} ion supply is insufficient for the formation of BaHF. This argument is also supported by the observed increase in Fe_2O_3 amount in short calcination time experiments as in Figure 5.3, since 5 moles of Ba^{2+} decompose while 1 mole of Ba^{2+} forms another compound upon the decomposition of $Ba_5Fe_{14}O_{26}$ and formation of $BaFe_{12}O_{19}$ instead. In time, Fe_2O_3 amount decreases back with the homogenization of the ions. Figure 5.4 shows a hypothetical growth model proposed for BaHF platelet formation.

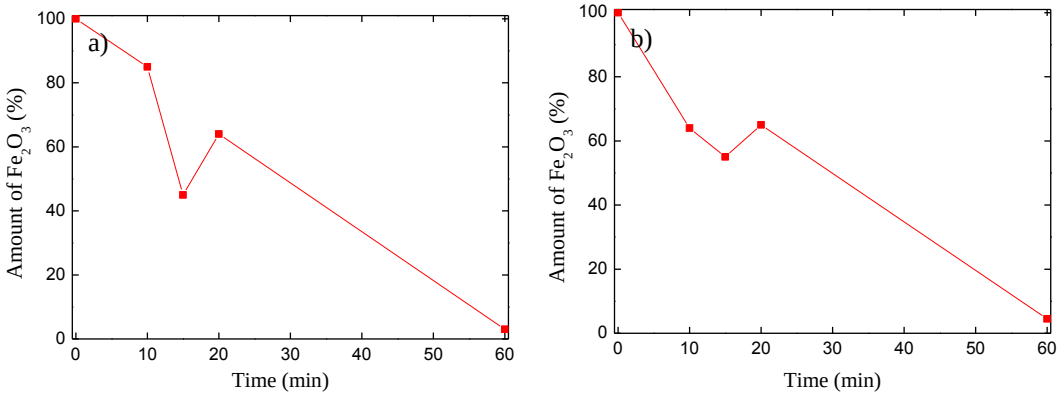

Figure 5.3 Effect of calcination time on the amount of Fe_2O_3 transformed in (a) NaCl flux (b) KCl flux.

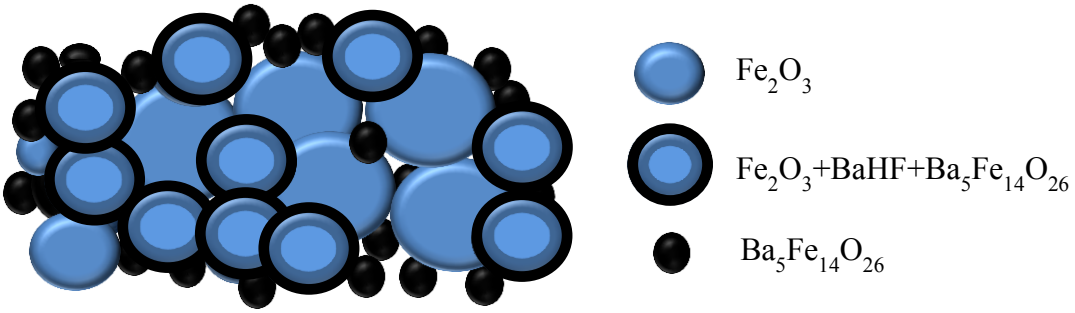

Figure 5.4 Proposed BaHF growth model showing the distribution of powders within single agglomerate during BaHF platelet formation.

After revealing the solubility of initial raw materials in the molten salts and the apparent activation energy for BaHF formation in both fluxes together with the wettability characteristic of Fe_2O_3 by the molten salts, growth mechanisms resulting in different morphologies in varying flux environments could be suggested. In NaCl flux, for all the calcination durations (1, 2, 2.5 and 3.5 h) Ba^{+2} and O^{-2} ions diffuse into the Fe_2O_3 clusters between 850 and 900 °C resulting in the formation and coarsening of BaHF platelets. Between 900 and 950 °C concentration of ions within the clusters becomes locally higher than that in the flux resulting in the decomposition of BaHF preferentially from the corners of the platelets evident from the rounded platelet morphologies with decreased average size. Even though the average platelet size does not change considerably with increasing time (Figure 5.5), platelets become more rounded with increase in time as can be seen from SEM images (i in Figures 4.9-4.20) which is probably due to a desorption process.

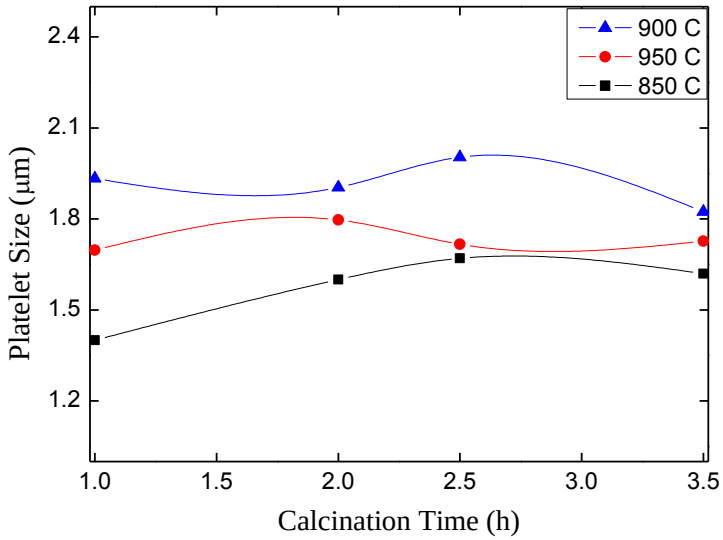

Figure 5.5 Platelet size vs. calcination time graph showing the change in the platelet size with increasing calcination durations at calcination temperatures of 850, 900 and 950 ˚C.

In KCl flux, for all calcination durations average platelet size increases with increasing temperature between 850 and 900 °C, while it decreases in the higher calcination temperature region as it is seen from 2lnD vs. 1/T graphs (Figure 4.21-4.24). The decrease between 900 and 950 °C also results from the decomposition of BaHF due to transient Ba^{+2} and O^{-2} deficiency in the flux. However, unlike in the case of NaCl, dissolution of BaHF in KCl flux should be occurring homogeneously on all surfaces of the platelets resulting in the preservation of the sharp cornered initial platelet shape at all calcination durations which are seen from SEM images (a in Figures 4.9-4.20).

In the literature, there are studies reporting the change in the growth mechanism by temperature during molten salt synthesis evidenced by the changes in the measured "activation energy for particle growth" [51, 56]. In the present study, apparent activation energy for BaHF platelet formation also shows a variation with temperature. Nevertheless, currently observed change in the negative direction has been attributed to the existance of non-diffusional growth mechanism(s).

During synthesis studies it has been observed that the amount of BaHF phase within the structure increases together with the average platelet size when using a combination of two fluxes. This is attributed to the better wettability of the Fe_2O_3 particles by the flux mixture. As a summary, when the molten salt synthesis of BaHF platelets in NaCl and KCl based fluxes is evaluated in terms of the formation efficiency and suitability of the morphology for textured bulk BaHF ceramic processing by TGG, 70 to 90 wt% NaCl containing flux compositions seem to generate the highest amount of conversion to BaHF along with largest platelet size and aspect ratio at 900 °C by 2 h calcination.

In the case of the texture analyses of multilayered ceramics, the unit cell parameters determined by the Rietveld refinements of powder BaHF and textured bulk BaHF which were refined with both March-Dollase (MD) and Spherical Harmonics (SH) functions are consistent with the theoretical values for BaHF. Since the textured ceramics contain phases other than BaHF, their fitting with the whole diffraction pattern is poor. Although the curves calculated by GSAS do not fit appropriately with the real data in the case of textured ceramics, estimated densities are quite close to the theoretical values. However, density in refinement with SH function differs from the actual value more than that in the case of MD function. This is one of the reasons why MD function is more suitable than SH function for the texture refinement of Bragg-Brentano diffraction pattern. Another reason for the poor fitting of the curves is that due to the defocusing effect and low structure factor of (006) peak, its intensity is not adequate, and hence the refinement values are not perfect [115]. Consequently, almost all Rietveld analyses are done by using neutron diffraction data. When the goodness of fit (χ^2) is considered, in the case of powder BaHF, it is not as low as in the case for textured ceramics which is caused by the intensity difference with the calculated plot. Intensity difference shows that the powders have some preferred orientation due to the placement of powders to the goniometer. Still textured ones have lower degree of fit as a result of the incorporation of texture parameters to GSAS. It is lower for the case of March-Dollase function resulting in the better density value. Since the calculated curves do not fit better, their R_p and R_{wp} values are not low enough.

Isotropic thermal factors are normal (positive) in all three cases. Also, Cagliotti terms are as expected because GU and GW values are either positive or zero, and GV values are negative. However, Rietveld refinement obtained by using MD function gives the microstrain value (LY) of zero which is an unreasonable result that might have been caused by poor fitting of the diffractograms. All these findings except LY value for Rietveld refinement by MD function are seen to be logical, and resultant refinement values have high degree of reliability.

In the case of the pole figure measurements, stereographic projection of (006) plane shows nonhomogeneous distribution of the planes. However, this situation is not so distinct because of the low intensity of (006) plane.

In addition to the Rietveld analysis and pole figure measurements, EBSD results also show the nonhomogeneous distribution of poles on (001) planes indicating the availability of some texture on that plane. The red regions show the grains oriented on (001) plane (Figure 5.6) while the pink regions show the grains that are tilted with a small angle from (001) plane. From the figure, it can be seen that the red regions are less than the half of the whole area in the image (~33 %); however, the rest is composed of the grains that have the orientation close to the red ones.

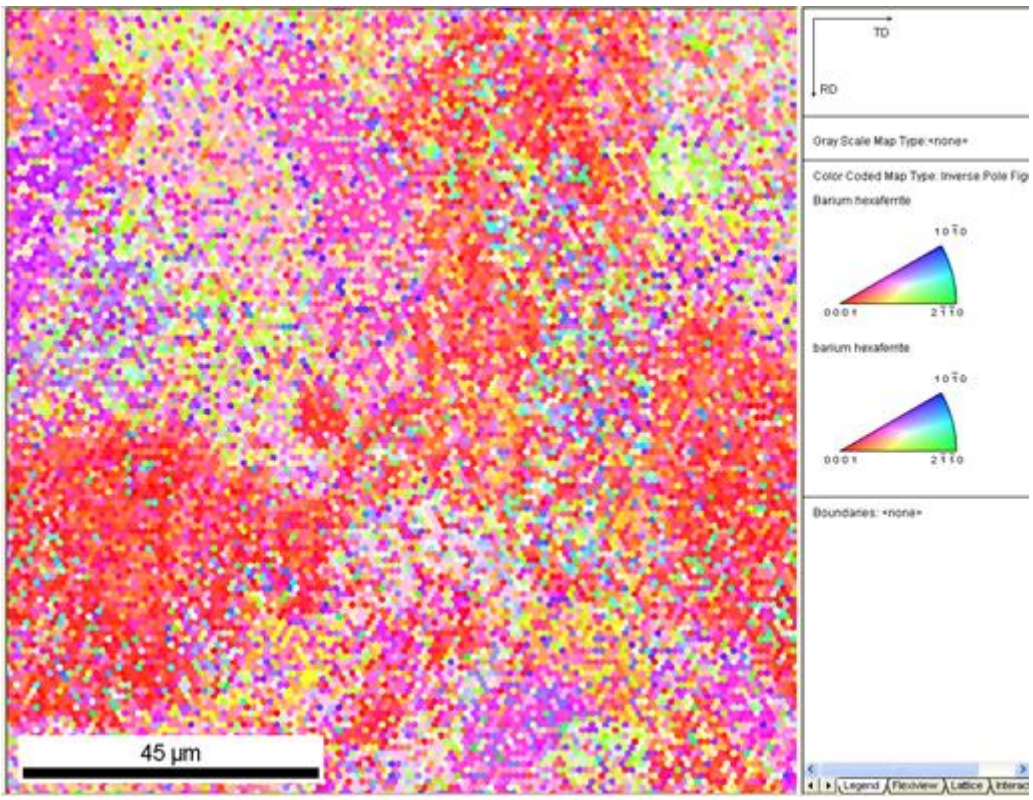

Figure 5.6 Inverse pole figure of bulk BaHF showing the orientation distribution of the grains on its planar surface.

Even though texture on (006) plane is not as obvious as in the case of other methods, when combined with the results of the Rietveld refinements and EBSD analyses, pole figure measurements also point out to the presence of some texture formation in BaHF ceramics produced by using the platelets synthesized by RTGG from BiF seed crystals and processed by tape casting. In fact, the preferred orientation value of 33% is consistent with the Rietveld results since March coefficient, G, is found as 0.67 giving the texture amount of 33%.

CHAPTER 6

CONCLUSION

For the production of textured BaHF ceramics, fine initial powders along with platelets having large radial size and high aspect ratio are required. For this purpose, BaHF platelets were synthesized by both molten salt synthesis (MSS) and reactive templated grain growth (RTGG) methods while the powders were synthesized by mixed oxide technique.

During synthesis of the platelets by MSS, the formation mechanism of BaHF platelets has been discussed by conducting short calcination time experiments. Moreover, effect of calcination time and temperature together with flux type and amount on the morphology and amount of formation has been studied in detail. In the case of the platelets synthesized by RTGG method, rod-like bismuth ferrite particles were synthesized in order to be used as seed crystals of subsequent BaHF platelets.

Laminated bulk ceramics were produced by tape casting method. Using the platelets synthesized by both MSS and RTGG methods, two different multilayered ceramics were obtained. In order to determine the degree of texture achieved in the bulk ceramic bodies Rietveld analysis, pole figure measurement and EBSD characterization have been conducted.

Conclusions presented below show the highlights of this study:

- This study reveals that in the case of the platelet synthesis by molten salt synthesis, the solubility of Fe_2O_3 in molten NaCl-KCl salts is negligible,

and BaHF forms by dissolution of BaO in the flux followed by diffusion of Ba^{+2} and O^{-2} ions to the Fe_2O_3 particles.

- In pure NaCl flux, BaHF formation starts rapidly and desorption from the surface occurs subsequently due to the higher wettability of Fe_2O_3 by NaCl. In case of pure KCl flux, saturation of Fe_2O_3 clusters by Ba^{+2} and O^{-2} ions and BaHF formation proceeds a longer period of time.
- Platelets synthesized in NaCl flux are rounded at any time and temperature which can be attributed to selective desorption of BaHF. However, decomposition occurs homogenously in the case of KCl leading to the preservation of sharp cornered platelet shape.
- Large platelets having high aspect ratio that are required for the fabrication of textured bulk BaHF ceramics can be synthesized in the flux mixtures containing the combination of NaCl and KCl molten salts. Molten salt containing 70 to 90 wt% NaCl seem to produce the highest amount of conversion to BaHF along with largest final platelet size and aspect ratio by calcination at 900 ˚C for 2 h.
- Platelets synthesized by MSS cannot exceed ~2-4 μm average radius, and they have relatively low aspect ratio in order to be used effectively for the production of textured ceramics by tape casting based on TGG.
- Platelets synthesized by RTGG method have larger size (~30-40 μm) with high aspect ratio making them preferable seed crystals for the production of textured ceramics by tape casting utilizing TGG phenomenon.
- Laminated textured bulk ceramics obtained by using the platelets of RTGG method contains some phases other than BaHF.
- In Rietveld refinements, texture analyses with both March-Dollase and Spherical Harmonics functions have resulted in poor matching of calculated curves and actual data points due to the existence of other phases within the structure.
- In Rietveld analysis, both the texture fraction and ratio results obtained by March-Dollase function and texture index larger than 1 along with the pole figures resulted from Spherical Harmonics function show the existence of

texture on (006) plane of bulk BaHF ceramics processed by tape casting utilizing TGG phenomenon.

- Pole figure measurements along (006) plane on which the distribution of planes is nonhomogeneous have indicated the existence of some texture that is not so strong. However, these results may contain some error due to the low intensity of (006) plane.
- Pole figures and inverse pole figures obtained by EBSD analysis have also supported the presence of texture on (006) plane. Furthermore, the March Coefficient (G) that has been calculated as 0.67 is the same with the one based on the pole figure measurements of EBSD analysis showing the existence of a preferred orientation in the bulk BaHF ceramics with a degree of 33 %.

REFERENCES

[1] P. S. Neelekanta, Handbook of Electromagnetic Materials: Monolithic and Composite Versions and Their Applications. (CRC Press, Washington D.C., 1995).

[2] H.I. Hsiang, C.S. Hsi, T.C. Lee, C.H. Chang, Journal of Magnetism and Magnetic Materials 268 (2004) 186.

[3] H.I. Hsiang, Japanese Journal of Applied Physics 41 (2002) 5137.

[4] J. Smith, H.P.J. Wijn, Ferrites (Philips Technical Library, Eindhoven, Netherlands, 1959).

[5] H. Hibst, Angewandte Chemie International Edition 21 (1982) 270-282.

[6] Y. Du, H. Gao, X. Liu et al., Journal of Materials Science (2010) 45:2442–2448.

[7] J. Ding, W.F. Miao, P.G. McCormick, R. Street, Journal of Alloys and Compounds 281 (1998) 32-36.

[8] A. Mali, A. Ataie, Scripta Materialia 53 (2005) 1065-1075.

[9] N. Shams, X. Liu, M. Matsumoto, A. Morisako, Journal of Magnetism and Magnetic Materials 290-291 (2005) 138-140.

[10] O. Carp, R. Barjega, E. Segal, M. Brezeanu, Thermochimica Acta 318 (1998) 57-62.

[11] D. K. Cheng, Fundamentals of Engineering Electromagnetics (Addison-Wesley Publishing Company, Inc., 1993).

[12] P.A. Marino-Castellanos, et al., Journal of Magnetism and Magnetic Materials, 280 (2-3) (2004) 214-220.

[13] E. Suvaci, M. M. Seabaugh, G. L. Messing, Journal of the European Ceramic Society 19 (1999) 2465±2474.

[14] E. K. Akdogan, R. E. Brennan et al., Journal of Electroceramics (2006) 16: 159–165.

[15] R.H. Arendt, J.H. Rosolowski, J.W. Szymaszek, Materials Research Bulletin 14 (1979) 703–709.

[16] T. Kimura, M. Machida, T. Yamaguchi, Journal of American Ceramic Society 66 (1983) C195–C197.

[17] L. H. Hemming, Electromagnetic Anechoic Chambers: A Fundamental Design and Specification Guide (John Wiley & Sons, Inc., 2002).

[18] J. Qiu, M. Gu, and H. Shen, Journal of Magnetism and Magnetic Materials, 295 (3) (2005) 263-268.

[19] H. Nornikman, P.J. Soh, A.A.H. Azremi, H.M.R Nurul, International Symposium on Antennas and Propagation, ISAP, Taipei, Taiwan, (2008).

[20] N. V. Katartzis, T. D. Tsiboukis, Modern EMC Analysis Technique II, (Morgan & Claypool, 2008).

[21] C. Brito, A. Lubiano, N. Hui, and D. Arakaki, Proceedings of the 26th Annual Antenna Measurement Techniques Association Meeting & Symposium, Atlanta, (2004) 403-408.

[22] Cuming Microwave Corporation Technical Data Sheet, Technical Bulletin 390-11, N-15-000-01154-A, (Avon, USA, 1997).

[23] Cuming Microwave Corporation Technical Data Sheet, Technical Bulletin 390-2, N-15-000-0126-A, (Avon, USA, 1997).

[24] Retrieved on 13th of June, 2012 from, http://www.aemi-inc.com/content/products/standard-absorbers/wedge-absorbers-aew-series.

[25] Retrieved on 13th of June, 2012 from, http://www.aemi-inc.com/content/products/standard-absorbers/convoluted-absorbers-aec-series.

[26] Technical Data Sheet, AN Absorber, Emerson and Cumings.

[27] Retrieved on 8th of June, 2012 from, http://datasheets.globalspec.com/ps/5236/EmersonCumingMicrowaveProducts/C5D177AF-1CAB-4A04-ABBE-3609761E4AC4.

[28] C. K. Yüzcelik, Radar Absorbing Material Design (Naval Postgraduate School, Monterey, 2003).

[29] E. F. Knott, J. F. Schaeffer, M. T. Tuley, Radar Cross Section, (Artech House, 1993).

[30] RF Absorbers Catalog, Advanced ElectroMagnetics, Inc., Santee, CA, 2011.

[31] Retrieved on 9th of June, 2012 from,
http://www.ramayes.com/RF_Absorber.htm.

[32] R. Louh, T. G. Reynolds III, R. C. Buchanan, Ferrite Ceramics in Ceramic Materials for Electronics (Marcel Dekker Inc., Newyork, 2004).

[33] R. Valenzuela, Magnetic ceramics (Cambridge University Press, 1994.).

[34] J. Smit and H. P. J. Wijn, Les Ferrites. (Bibliotheque Technique Philips, Paris, 1961).

[35] N. Gürkan, Studies on interaction of electromagnetic waves with barium hexaferrite ceramics, in "Department of Metallurgical and Materials Engineering" (Middle East Technical University, Ankara, 2008).

[36] A. J. Moulson, Herbert, J. M., Electroceramics: Materials, Properties, Applications (John Wiley & Sons Ltd. 2003).

[37] G. Winkler, Crystallography, Chemistry and Technology of Ferrites. In Magnetic Properties of Materials (McGraw-Hill, London, 1971).

[38] G. Albanese, M. Carbucicchio, L. Pareti, S. Rinaldi, E. Licchini and G. Slokar, Journal of Magnetism and Magnetic Materials **15-18** (1980) 1453.

[39] X. Obradors, A. Collomb, M. Pernet, D. Samaras and J. C. Joubert, Journal of Solid State Chemistry 56 (1985) 171-81.

[40] F. Kools, Hard Magnetic Ferrites (Encyclopedia of Advanced Ceramic Materials, Pergamon Press, Oxford, 1991).

[41] G. K. Sahoo Synthesis and characterization of $BaTiO_3$ Prepared by Molten Salt Synthesis Method, in 'Department of Ceramic Engineering' (National Institute of Technology, Rourkela).

[42] D. H. Chen, X. R.He, Materials Research Bulletin 36 (2001) 1369–1377.

[43] P. Brahma, D. Chakravorty, K. Singh and D. Bahadur, Journal of Materials Science Letters 9, (1990) 1438-1440.

[44] S. Somiya and R. Roy, Bulletin of Materials Science 23 (6) (2000) 453–460.

[45] W. L. Suchanek and R. E. Riman, Advances in Science and Technology 45 (2006) 184-193.

[46] T. Yamauchi, Y. Tsukahara, T. Sakata, H. Mori, T. Chikata, S. Katoh Y. Wada, Journal of Magnetism and Magnetic Materials 321 (2009) 8–11.

[47] S.P. Gaikwad, S.B. Dhesphande, Y.B. Khollam, V. Samuel, V. Ravi, Materials Letters 58 (2004) 3474– 3476.

[48] A. Iyiel, Synthesis and Characterization of Barium Ferrite Powders as Radar Absorbing Material, in "Department of Metallurgical and Materials Engineering" (Middle East Technical University, Ankara, 1997).

[49] S.H. Cho, J.V. Biggers, Journal of American Ceramic Society 66 (1983) 743–746.

[50] Y. Hayashi, T. Kimura, T. Yamaguchi, Journal of American Ceramic Society 69 (1983) 322–325.

[51] C.C. Li, C.C. Chiu, S.B. Desu, Journal of American Ceramic Society 74 (1991) 38–47.

[52] K. Katayama, M. Abe, T. Akiba, Journal of European Ceramic Society 5 (1989) 183–191.

[53] K. Katayama, M. Abe, T. Akiba, Ceramics International 15 (1989) 289–295.

[54] Z. Cai, X. Xing, R. Yu, Journal of Alloys and Compounds 420 (2006) 273–277.

[55] K. Yoon, Y. S. Cho, D. H. Kang Journal of Materials Science 33 (1998) 2977-2984.

[56] Z. Cai, X. Xing et al., Journal of Alloys and Compounds, 454 (2008) 466–470.

[57] O. A. Esin, S. E. Lyumkis, Russion Journal of Inorganic Chemistry 2 (1957).

[58] M. Thirumal, P. Jain, and A.K. Ganguli, Materials Chemistry and Physics 70 (2001) 7.

[59] I. K. Naik and A. R. Das Transactions- Indian Ceramics Society, 40 (1981) 199.

[60] Beretka and T. Brown, Australian Journal of Chemistry, 24 (1971) 237.

[61] R. H. Arendt, Journal of Solid State Chemistry 8 (1973) 339.

[62] K. Haneda and H. Kojima, Journal of Applied Physics 44 (1973) 3760.

[63] H. Sakai, K. Hanawa and K. Aoyagi, IEEE Transactions on Magnetics, 28(6) (1992).

[64] H. I. Hsiang and C. H. Chang, Journal of Magnetism and Magnetic Materials 278 (2004) 218–222.

[65] T. Tani, T. Kimura, Advances in Applied Ceramics, 105 (1) (2006) 55-63.

[66] T. Tani, Journal of the Ceramic Society of Japan, 114 [5] (2006) 363-370.

[67] T. Tani, Journal of Korean Physical Society 32 (1998) S1217-S1220.

[68] K. Okazaki, H. Igarashi, K. Nagata, T. Yamamoto, and S. Tashiro, IEEE Transactions- Ultrasonics Ferroelectrics and Frequency Control 33 (1986) 328–337.

[69] T. S. Suzuki, T. Uchikoshi and Y. Sakka, Science and Technology of Advanced Materials 7 (2006) 356–364.

[70] Y. Sakka, T. S. Suzuki and T. Uchikoshi, Journal of European Ceramic Society 28 (2008) 935–942.

[71] K. H. Brosnan, G. L. Messing, R. J. Meyer and M. D. Vaudin, Journal of American Ceramic Society 89 (2006) 1965–1971.

[72] M. M. Seabaugh, I. H. Kerscht and G. L. Messing, , Journal of American Ceramic Society 80 (1997) 1181–1188.

[73] M.D. Snel, J. Van Hoolst et al., Journal of the European Ceramic Society 29 (2009) 2757–2763.

[74] M. M. Seabaugh, G. L. Cheney et al., Journal of Intelligent Material Systems and Structures, 15 (2004).

[75] E. M. Sabolsky, L. Maldonado, Journal of Electroceramics 25 (2010) 77–84.

[76] E. Suvacı, K. -S. Oh and G. L., Messing Acta materialia 49 (2001) 2075–2081.

[77] J. A. Horn, S. C. Zhang, U. Selvaraj, G. Messing and S. T. Mckinstry, Journal of the European Ceramic Society 29 (2009) 2757-2763.

[78] E. Suvaci, M. M. Seabaugh and G. L. Messing, Journal of the European Ceramic Society 19 (1999) 13.

[79] E. Suvaci, and G. L. Messing, Journal of American Ceramic Society, 83 **(**2000) 8.

[80] M. M. Seabaugh, G. L. Messing and M. D. Vaudin, Journal of American Ceramic Society 83 (2000) 12.

[81] Y. Yan, K. H. Cho and S. Priya, Journal of American Ceramic Society 94 [6] (2011) 1784–1793.

[82] H. Sitepu, Characterization of Preferred Orientation in Crystalline Materials by X-Ray Powder Diffraction, in Department of Physics (Curtin University of Technology, Perth, 1991).

[83] Y.N. Wang, J.C. Huang, Materials Chemistry and Physics 81 (2003) 11–26.

[84] P. Echlin, C.E. Fiori, J.I. Goldstein, D.C. Joy, C.E. Lyman, E. Lifshin, D.E. Newbury, A.D. Romig, Scanning Electron Microscopy and X-ray Microanalysis, (Plenum Press, London, 1992).

[85] C. Escher, G. Gottstein, Acta Materialia 46 (1998) 525.

[86] I.C. Hsiao, S.W. Su, J.C. Huang, Metallurgical and Materials Transactions 31A (2000) 2169.

[87] T.R. McNelley, D.L. Swisher, M.T. Perez-Prado, Metallurgical and Materials Transactions 33 (2002) 279.

[88] L.G. Schulz, Journal of Applied Physics 20 (1949) 1030.

[89] D. Chateigner, P. Germi and M. Pernet, Journal of Applied Crystallography 25 (1992) 766-769.

[90] R.J. Roe, Journal of Applied Physics 36 (1965) 2024.

[91] H.J. Bunge, Z. Metallkd. 56 (1965) 872.

[92] U.F. Kock, C.N. Tome, H.R.Wenk, Texture and Anisotropy: Preferred Orientation in Polycrystals and Their Effect on Materials Properties, (Cambridge University Press, Cambridge, 1998).

[93] M. M. Seabaugh, M. D. Vaudin, J. P. Cline and G. L. Messing Journal of American Ceramic Society, 83 [8] (2000) 2049–54.

[94] L. B. McCusker, R. B. Von Dreele, D. E. Cox, D. Louër and P. Scardi Journal of Applied Crystallography 32 (1999) 36-50.

[95] A. Le Bail, H. Duroy and J. L. Fourquet Materials Research Bulletin 23 (1988) 447-452.

[96] H. R. Wenk, L. Cont, Y. Xie, L. Lutterotti, L. Ratschbacher and J. Richardson Journal of Applied Crystallography 34 (2001) 442–453.

[97] A. March, Z. Kristallogr., 81 (1932) 285–97.

[98] W. A. Dollase, Journal of Applied Crystallography 19 (1986) 267–72.

[99] T. Leventouri, Physica C 277 (1997) 82-86.

[100] H. J. Bunge. Texture Analysis in Materials Science, (London:Butterworth, 1982).

[101] N. C. Popa, I Appl. 25 (1992) 611--616.

[102] R. B. Von Dreele, Journal of Applied Crystallography 30 (1997) 517-525.

[103] R. H. Arendt, Journal of Applied Physics 44(7) (1973).

[104] Y. T. Chien, H. C. Pan et al., Journal of American Ceramic Society 72 [8] (1989) 1328-32.

[105] A. Ghasemi, et al., Journal of Magnetism and Magnetic Materials, **302**(2) (2006) 429-435.

[106] A. Ghasemi, A. Saatchi, M. Salehi, A. Hossienpour, A. Morisako, X. Liu, Physica Status Solidi (A), **203**(2) (2006) 358-365.

[107] R. D. C. Lima, M. S. Pinho, M. L. Gregori, R. C. R. Nunes, T. Ogasawara, Materials Science, **22**(3) (2004) 245-252.

[108] S. Sugimoto, et al., Magnetics, IEEE Transactions on, **35**(5) (1999) 3154-3156.

[109] Retrieved on 3rd of May, 2012 from, http://www.crct.polymtl.ca/fact/phase_diagram.php?file=KCl-NaCl.jpg&dir=FTsalt.

[110] J. Lu et al., Journal of Crystal Growth 318 (2011) 936-941.

[111] W.D.Townes, J.H.Fang, A.J.Perrotta, Zeitschrift für Kristallographie: 125(125) 437-449.

[112] W. Martienssen, H. Warlimont, Springer Handbook of Condensed Matter and Materials Data, (Springer, 2005).

[113] S. S. Vidyawathi, R. Amaresh and L. N. Satapathy, Bulletin of Material Science, 25(6) (2002) 569–572.

[114] J. A. Horn, S. C. Zhang, U. Selvaraj, G. L. Messing and S. T. McKinstry, Journal of American Ceramic Society, 82 [4] 921–26 (1999).

[115] E. Guilmeau, D. Chateigner, T. S. Suzuki, Y. Sakka et al., Chemistry of Materials, 17 (2005), 102-106.